SLAC-279
UC-34D
(E)

MEASUREMENT OF THE LIFETIMES OF THE NEUTRAL AND CHARGED D MESONS*

Larry Donnie Gladney†

Stanford Linear Accelerator Center
Stanford University
Stanford, California 94305

March 1985

Prepared for the Department of Energy

under contract number DE-AC03-76SF00515

Printed in the United States of America. Available from the National Technical Information Service, U.S. Department of Commerce, 5285 Port Royal Road, Springfield, Virginia 22161. Price: Printed Copy A07, Microfiche A01.

* Ph.D. dissertation.

† This work was supported in part by the Department of Energy, contracts DE-AC03-76SF00515 and DE-AC03-76SF00098.

ABSTRACT

Results are presented on the use of a high-resolution drift chamber in the Mark II Detector at PEP to measure the lifetimes of D^0 and $D^{\pm}$ mesons produced in e^+e^- annihilations at 29 GeV. Based on a sample of 74 events for the D^0 mesons and 23 events for the $D^{\pm}$ mesons, the lifetimes are found to be

$$\tau_{D^0} = 4.7^{+0.9}_{-0.8} \pm 0.5 \times 10^{-13} \text{ s}$$
$$\tau_{D^{\pm}} = 8.9^{+3.8}_{-2.7} \pm 1.3 \times 10^{-13} \text{ s}.$$

The ratio of these lifetimes, $\tau_{D^0}/\tau_{D^{\pm}} = 1.9^{+0.9}_{-0.7} \pm 0.3$, indicates that the decays of these mesons cannot be explained by the simple spectator model of charmed particle decay.

ACKNOWLEDGEMENTS

At times such as these, I always find it impossible to acknowledge all of those who have aided me with their kindness, their wisdom, and their support through the long years of graduate school. There are a few, however, who have made special contributions and to them I give my heartfelt thanks. First among these, are my advisors, John Jaros and Bob Hollebeek, who gave me the freedom I needed to pursue my interests and the patience and guidance necessary to direct me towards a successful end to my studies here. Special mention must also go to John Yelton for his insight and leadership throughout the course of this analysis; to Theo Schaad for the unfailing enthusiasm in physics that provided me with much inspiration; to Heidi Schellman for her innumerable contributions to the experiment. Many thanks must also go to Rene Ong, Nigel Lockyer, and Dan Amidei who not only made a great deal of this thesis possible through their work, but provided me with warm friendship throughout the years. Finally, I wish to thank Bruce LeClaire for his willingness to listen and his willingness to teach, both of which made my time at SLAC not only profitable but enjoyable.

CONTENTS

LIST OF TABLES

LIST OF FIGURES

1. Introduction

The discovery of a family of extremely narrow vector mesons in 1974[1-2] opened a new era in high-energy physics. After intensive theoretical and experimental study, particle physicists have come to the conclusion that these narrow resonances are bound states of charmed quarks and anti-quarks. Since charm is an entirely new property of matter whose very existence was unknown until ten years ago, its interactions via the strong, weak, and electromagnetic (EM) forces have been the subject of extensive experimental research. Such studies on the J/Ψ family, especially those on the weak interactions of charm quarks, were hampered by the fact that the charm-anti-charm content of these mesons leaves a state with no net charm. It was only with the discovery of mesons with naked charm (i.e. mesons consisting of a charm quark and non-charm anti-quark) that any progress on this front was made. This thesis reports on a measurement of the lifetime of two of these charmed mesons; one aspect of the weak interactions of charm quarks. Table 1 gives the current list of the mesons along with some of their expected characteristics.

Table 1.

CHARMED MESONS

Name	Quark Content	J^p	Mass GeV/c^2
D^0	$(c\bar{u})$	0^-	1.865
$D^\pm$	$(c\bar{d})$	0^-	1.869
$F^\pm$	$(c\bar{s})$	0^-	1.975
D^{*0}	$(c\bar{u})$	1^-	2.010
$D^{*\pm}$	$(c\bar{d})$	1^-	2.010
$F^{*\pm}$	$(c\bar{s})$	1^-	2.125

1.1 Theoretical Considerations

We begin our study of the weak interactions of charmed mesons by reviewing current theoretical expectations and experimental findings. The detailed list of theoretical predictions based on a SU(4) theory of the spectroscopy of a world composed of four quarks has been presented in ref.[3]. It is expected, for example, that the EM and strong interactions conserve quark flavor. One consequence of this is the observed associated production of charmed particles in e^+e^- annihilations. The process $e^+e^- \rightarrow c\bar{c}$ (see fig. 1) leads to charm hadrons in both jets of a typical hadronic event. In other words, the net charm of a final state from e^+e^- annihilations must be zero and the observance of one charmed particle in an hadronic event necessitates the existence of at least one other charmed particle. The most important consequence of flavor conservation, however, is that the decay of charmed hadrons can only occur through the weak interaction. Furthermore, the GIM mechanism[4] necessitates that the decay proceed only through the charged current as shown in fig. 1. Since the charm quark mass is sufficient to allow it to decay to either strange or down quarks, the relative amplitudes of these decays is governed by the Cabibbo mechanism and must, therefore, be proportional to $\cos\theta_c/\sin\theta_c$, where θ_c is the Cabibbo angle. Since experiment has determined that θ_c is small, charmed hadrons decay primarily to strange particles, giving rise to easily identifiable decay modes such as $D^+ \rightarrow K^-\pi^+\pi^+$. (We note here that it will be assumed throughout this thesis that statements relevant to any state are also relevant to its charge-conjugate state, e.g. $D^+ \rightarrow K^-\pi^+\pi^+$ implies that $D^- \rightarrow K^+\pi^-\pi^-$).

In order to derive rough quantitative predictions about the charmed hadron decay, it has generally been assumed that the spectator diagrams play a principal role. The primary assumption here is that the charm quark decays freely without

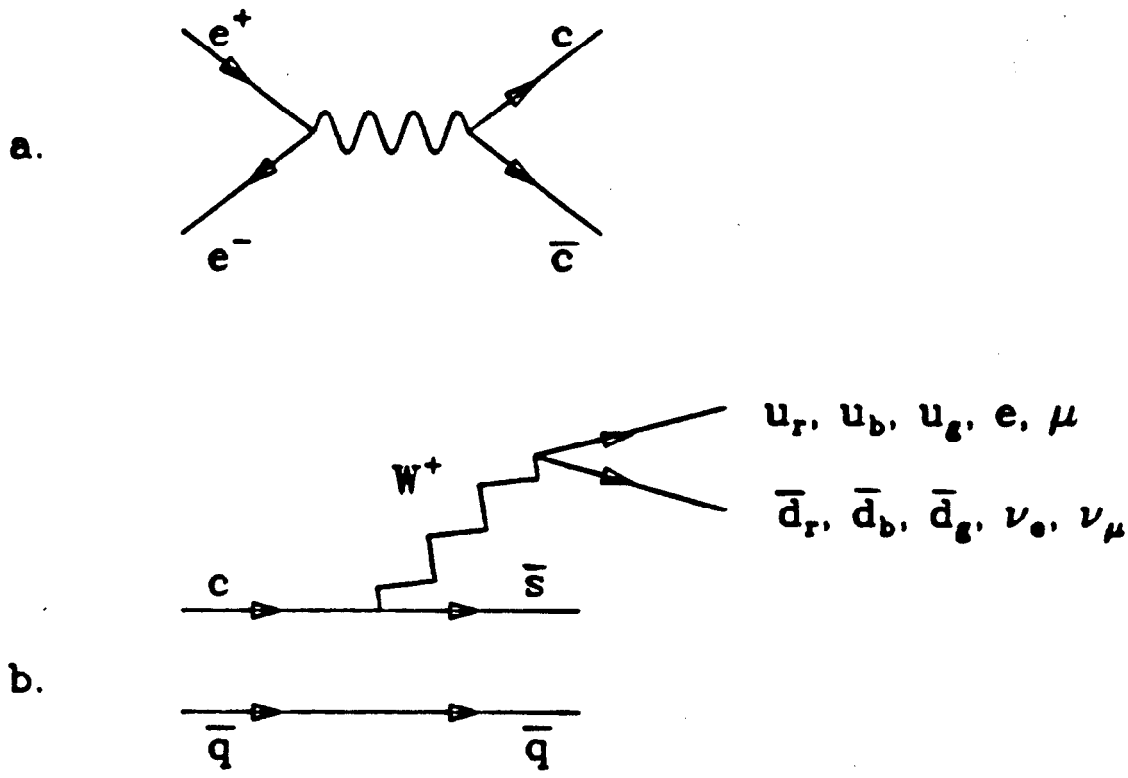

Fig. 1: a. Diagram for $e^+e^- \rightarrow c\bar{c}$.

b. Subsequent standard model decay of a charmed meson.

any interference from its "spectator" quark partner (see fig. 1). Under this assumption, it is trivial to calculate the charm lifetime in terms of the muon lifetime since the charm and muon decays differ only in the effective phase space and the number of channels available. Thus, in the context of the standard model,

$$\tau_c \simeq \frac{1}{5} \cdot \left(\frac{m_\mu}{m_c}\right)^5 \tau_\mu \simeq 2 \times 10^{-13}\text{s}$$

if effects from the finite mass of the strange quark are ignored. The factor of $\frac{1}{5}$ is due to the fact that there are 5 channels open for c decay (see fig. 1b) as opposed to the one decay channel for μ decay. (Since the W does not carry color, the $u, \bar{d}$ channel actually represents 3 decay channels instead of one.) Thus, in the spectator model, one expects that $\tau_{D^0} = \tau_{D^+} = \tau_{F^+}$. Since it is already known from experiments done at the SPEAR storage ring[5-6] that the relative semi-leptonic branching ratios for charmed mesons are such that

$$B_e(D^+)/B_e(D^0) > 1,$$

it is possible to conclude that $\tau_{D^+} > \tau_{D^0}$, and thus that the simple spectator model is <u>not</u> sufficient for a full understanding of charmed meson decay.

Various ideas have been suggested as possible explanations of the discrepancy between the theoretical and experimental values for the ratio τ_{D^+}/τ_{D^0}. Sextet dominance, non-spectator diagrams, and identical particle interference are three of the most popular examples. Each of these will be considered in detail.

The notion of sextet dominance comes about from detailed considerations of the proposed SU(3) structure[7-8] of the hadronic current in the GIM model. Specifically, the charm-changing four-quark portion of the SU(3) Lagrangian has

the form

$$\mathcal{L} \simeq \cos^2\theta_c[\bar{c}\gamma^\mu(1-\gamma_5)s][\bar{d}\gamma_\mu(1-\gamma_5)u] + \sin\theta_c\cos\theta_c\Big([\bar{c}\gamma^\mu(1-\gamma_5)s][\bar{s}\gamma_\mu(1-\gamma_5)u]$$
$$-[\bar{c}\gamma^\mu(1-\gamma_5)d][\bar{d}\gamma_\mu(1-\gamma_5)u]\Big) + \sin^2\theta_c\Big([\bar{c}\gamma^\mu(1-\gamma_5)d][\bar{s}\gamma^\mu(1-\gamma_5)u]\Big)$$

where u,d,s, and c are the Dirac spinors for the up, down, strange, and charm quarks and the color factors have been omitted. This Lagrangian has the SU(3) transformation property of a $\bar{6} + 15$ for charm-changing reactions. The 15 and $\bar{6}$ can be shown to be subgroups of the SU(4) 84 and 20-dimensional representations, i.e. the 84-dimensional representation of SU(4) breaks down to

$$84_{SU(4)} \rightarrow [(1+8+27)(\Delta C=0),\quad (15)(\Delta C=-1),\quad (\overline{15})(\Delta C=+1)]_{SU(3)}$$

and

$$20_{SU(4)} \rightarrow [\qquad\quad (8)(\Delta C=0),\quad (\bar{6})(\Delta C=-1),\quad (6)(\Delta C=+1)]_{SU(3)}$$

where $\Delta C = 0, \pm 1$ represents reactions in which charm changes by $0, \pm 1$. It is an experimentally observed fact that strange particle decays (for which $\Delta C = 0$) are governed by the Δ I $= \frac{1}{2}$ rule (i.e. isospin can change only by $\pm\frac{1}{2}$ in such decays). This leads to the theoretical assumption of 20-dominance in SU(4) since only in the 20-dimensional representation of SU(4) is Δ I$= \pm\frac{1}{2}$ assured for $\Delta C = 0$ reactions. This, in turn, leads to the expectation of 6-dominance or sextet dominance in SU(3) for $\Delta C = \pm 1$ reactions.

The consequence of sextet dominance in SU(3) is that certain hadronic decay modes of the D^+ such as $D^+ \rightarrow \overline{\mathrm{K}}^0\pi^+$ and $D^+ \rightarrow \overline{\mathrm{K}}^{*0}\rho^+$, are forbidden[9] . This, in turn, would lead to $\tau_{D^+}/\tau_{D^0} > 1$. Evidence for the first decay has already been observed[5,10] .

A simpler method for generating $\tau_{D^+}/\tau_{D^0} > 1$ is simply to assume that non-spectator diagrams such as those shown in fig. 2 are relevant to D meson decay. A diagram like fig. 2a is Cabibbo suppressed for D^+ mesons, thus, we would

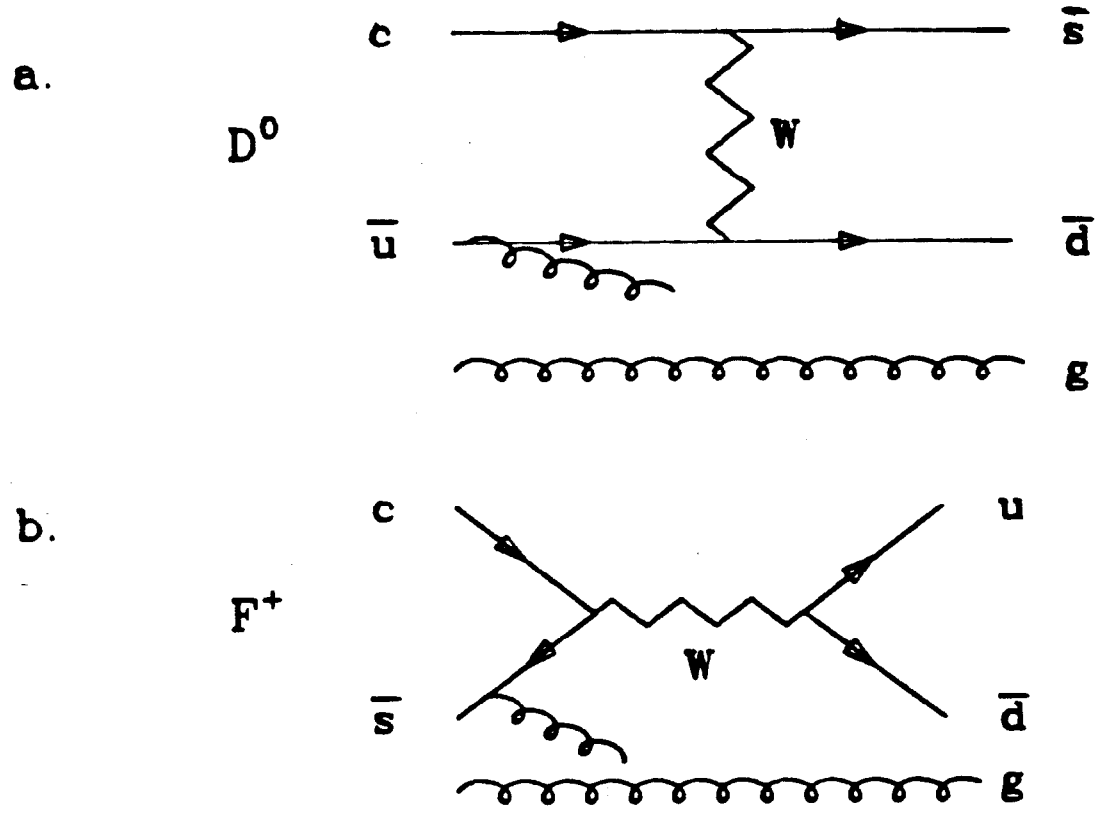

Fig. 2: Non-spectator diagrams for heavy-quark decay

again expect that there are more decay channels open to the D^0 meson so that $\tau_{D^+} > \tau_{D^0}$. The gluons attached to the quark lines are necessary to prevent the helicity suppression of these diagrams. It would otherwise be expected that the amplitude of the non-spectator diagrams would be multiplied by a factor of $(\frac{m_u}{m_c})^2$ since these diagrams represent pseudoscalar particles decaying into two light fermions. At least one other gluon must be present in order to make a color singlet in the final state. Several authors have suggested that the non-spectator diagrams can be the principal mode for D decay[11-12] .

Yet another way to make $\tau_{D^+} > \tau_{D^0}$ is to note that there are two diagrams contributing to the amplitude for non-leptonic decay of the D^+ as shown in fig.3. Fermi statistics demands that there be destructive interference between the spectator anti-quark $\bar{d}$ and the identical $\bar{d}$ in the final state coming from the charm quark decay.[13] . Initial estimates of the size of this effect indicated that it might be responsible for a considerable difference in the D^0 and D^+ lifetimes. Subsequent calculations disagree on the importance of this effect[14-17] .

1.2 Motivation for this Analysis

It has taken several years to develop the techniques for making precise measurements of charmed meson lifetimes. As shown above, the expected lifetimes are extremely short because of the relatively large charm quark mass. Only detection devices with extremely high resolution, such as emulsions, bubble chambers, and silicon strip detectors have been used to make measurements thus far. These experiments are not completely without bias, however, since they depend upon a finite lifetime to identify and isolate charmed particle decays from the huge background due to light quarks. In addition, the net yield of fully identified charm decays from these detectors has been small. This has limited the statistical power of the lifetime measurements done to date. However, in order to test

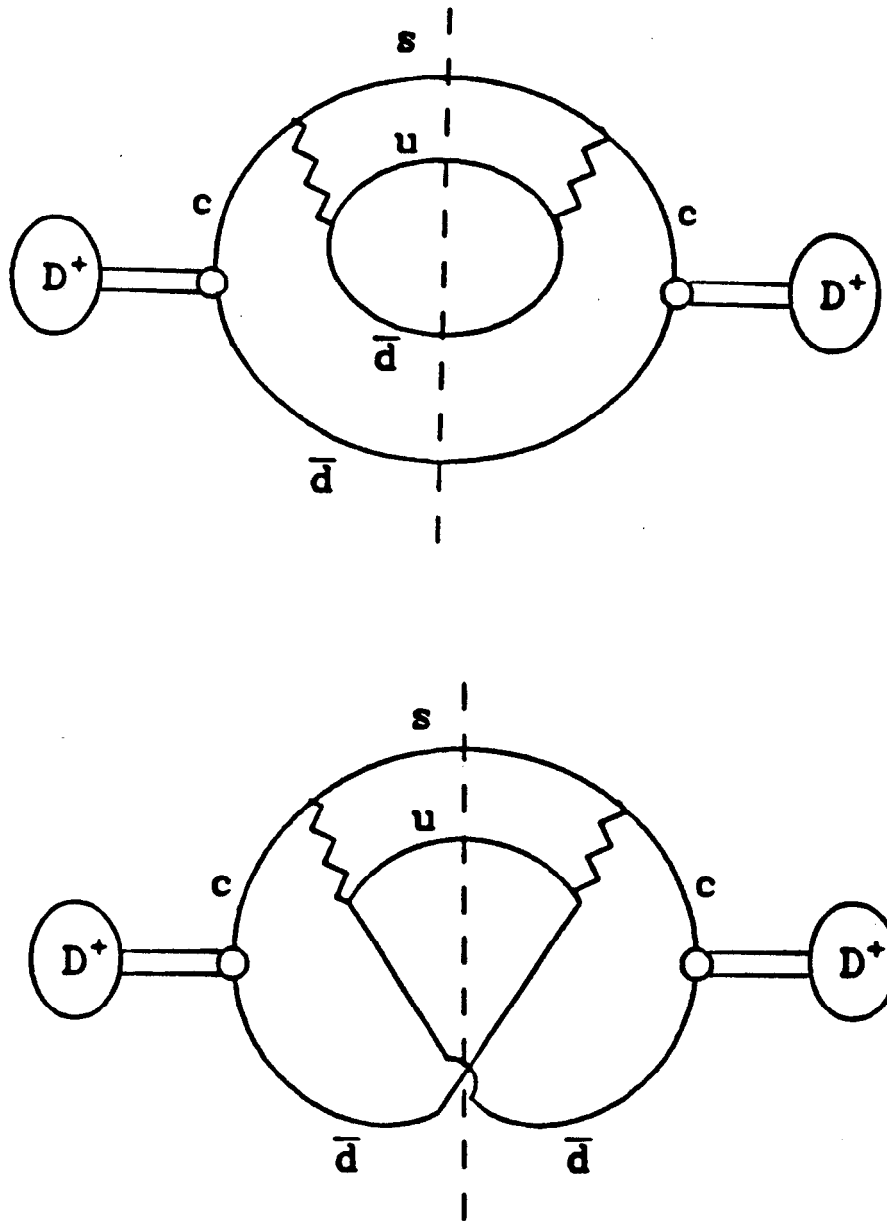

Fig. 3: The direct term diagram and interference term diagram for D^+ non-leptonic decay

calculations made on the basis of the scenarios described above, accurate values of τ_{D^+}, τ_{D^0}, and τ_{F^+} are necessary.

Storage rings are very suitable laboratories for making measurements on weak heavy hadron decays because these particles are copiously produced (for storage rings of appropriate energies) and easily distinguished from the backgrounds due to light quarks and processes other than one-photon annihilation. As will be shown, the identification of D^0 and D^+ mesons can be done nearly independently of the charm lifetime. However, the high repetition rate and highly-evacuated beam pipe of circulating electron-positron beams precludes the use of devices such as bubble chambers, which can continuously track particles from the point of their creation. Instead, drift chambers, with an intrinsic resolution which is a factor of 2 or more worse than bubble chambers, must be employed. Here, we must depend on copious production of the particles of interest in order to reduce the statistical error on the lifetime measurement.

We will justify the correctness of this statistical procedure by showing that many of the measurement errors relevant to the lifetime determination are Gaussian in nature. This means that the systematic errors on the final result can be well-understood and easily calculated. This contrasts sharply with bubble chamber and emulsion experiments which must contend with scanning efficiencies which are functions of the decay length to be observed. One added advantage of the procedure to be described is that a very similar method can be tested on the well-understood τ lepton.

This thesis presents the first measurement of charmed meson lifetimes using a high-resolution drift chamber. The data used here were taken with the Mark II detector at the PEP storage ring at a center-of-mass energy of 29 GeV. The Mark II was a general purpose detector capable of charged and neutral particle

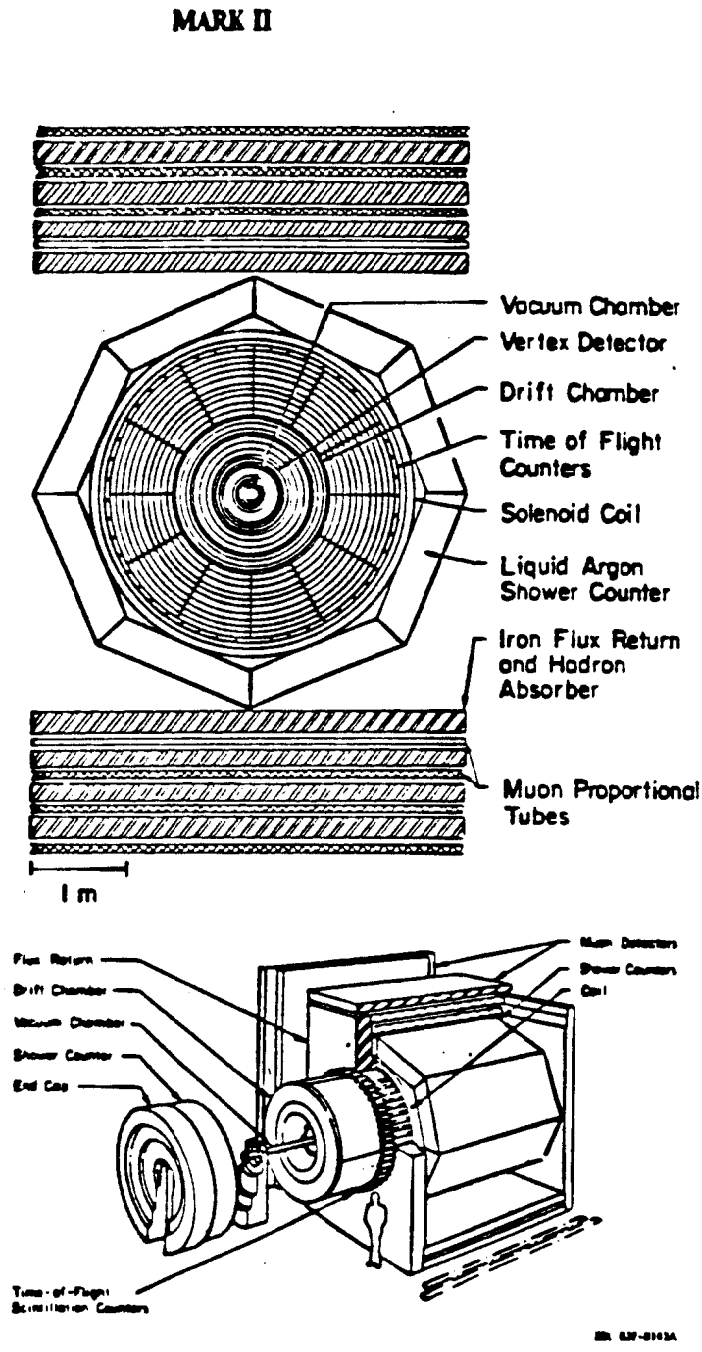

Fig. 4: The Mark II Detector

identification and accurate momentum measurement over a large fraction of the total solid angle. The addition of a very precise drift chamber augmented the physics capabilities of the detector by allowing high resolution charged-particle tracking. The various components of the detector and their performance are described in the next chapter.

2. The Mark II Detector

The Mark II detector was built and first operated at the SPEAR storage ring. After two years of operation there, it was moved to the PEP storage ring and took data at a center-of-mass energy of 29 GeV for four years. In the second year of operation, a high-resolution drift chamber called the vertex detector was installed to facilitate measurements of particle lifetimes on the order of 10^{-13} s. Only the data taken after the installation of the vertex detector were used in this analysis, so the following description of the detector apparatus and the schematic diagram shown in fig. 4 apply only to the configuration of the detector during the last three years of running. Components of the Mark II are described in an order representing increasing distance of the component from the beam interaction point.

2.1 Vertex Detector

The vertex detector[18] or vertex chamber (VC) as it was called, was a high precision cylindrical drift chamber situated inside and concentric with the inner wall of the main drift chamber. The chamber had seven axial layers of drift cells grouped into two concentric bands and contained in a pressure vessel with an outer radius of 0.35 m and a length of 1.2 m. The first band consisted of 4 layers of drift cells starting at a radius of 10.1 cm (relative to the beam line) and extending out to 12.6 cm. The second band of 3 layers extended from 30.4 to 32.0 cm in radius. The chamber had a total of 825 rectangularly shaped drift cells (270 in the first band, 555 in the second band). The vertex detector layout and wiring pattern are shown in fig. 5. In each cell, sense wire layers were separated from adjacent field wire layers by a distance of 4.2 mm. Sense wires were separated from adjacent field wires within a layer by 5.3 mm. The chamber

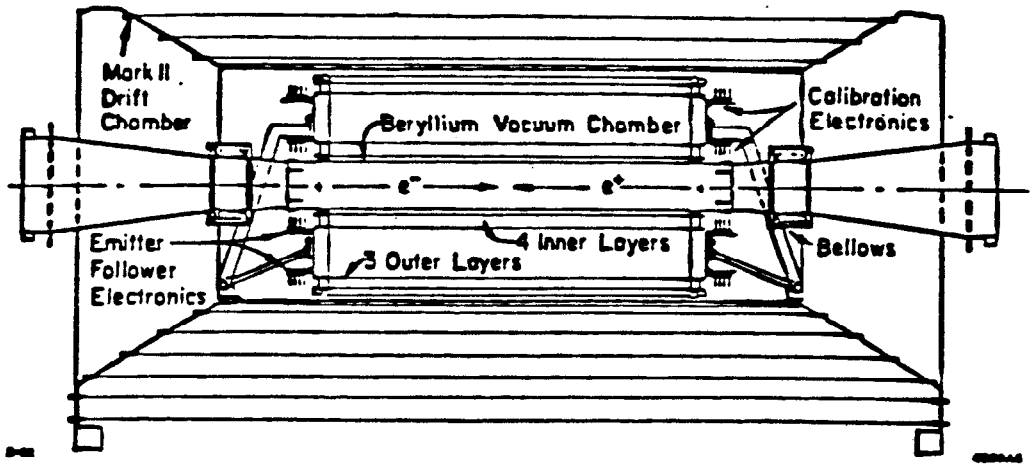

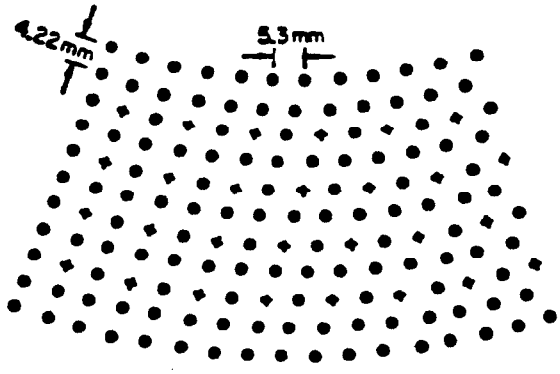

Fig. 5: The Mark II vertex detector and its wiring pattern

had two extra field wire layers outside of the drift cell array. One shielded the array from the ground surface of the inner wall of the pressure vessel while the other acted as an electrical shield between the array and the outer can of the pressure vessel. The chamber was operated in a 50/50 mixture of argon and ethane at an absolute pressure of 15.50 $\pm$ 0.05 psi.

In order to maximize the position resolution of the vertex detector, five conditions had to be met: First, the wires had to be precisely located. By visual inspection of each feedthru and the use of highly accurate machining techniques, the chamber wires were located to an accuracy of 15 μ (rms) throughout the chamber. The position of each sense wire feedthru was measured during construction for use in the tracking algorithm during event reconstruction. Table 2 lists the relevant parameters on wire spacing.

Table 2.

Placement of Sense Wires in Vertex Detector

	Layer	Radius (cm)	# of Sense Wires
Inner Band	1	10.1223	60
	2	10.9658	65
	3	11.8093	70
	4	12.6528	75
Outer Band	5	30.3668	180
	6	31.2103	185
	7	32.0538	190

Secondly, high resolution electronics were used to read out the chamber signals. Once every eight hours, calibration pulses were fanned out to each sense wire simultaneously (to within 350 ps) to ensure a common start time for all signal channels. The chamber pulses were coupled to amplifier/discriminators via 50 Ω

coaxial cables with a fast emitter-follower serving as an impedance matcher. A time-to-amplitude converter (TAC) measured the time between a discriminator pulse and a common stop pulse made with reference to the beam crossing signal. The TAC was read out with a dedicated microprocessor (BADC) which then sent data to the on-line computer. The time-measuring resolution for this system was better than 250 ps for all channels.

The third requirement was to minimize the multiple Coulomb scattering by minimizing the amount of material between the beam interaction point and the first position measurement. Thus, the section of beam pipe through the detector was formed of beryllium and also served as the inner wall of the vertex detector pressure vessel. The beryllium tube was 1.42 mm thick, 1.4 m long, and 15.6 cm in diameter. A 50 μ thick titanium foil was inserted inside the beryllium tube to absorb synchrotron radiation which backscattered off masks located 3 m from the interaction point. The outside of the tube was wrapped with a 50 μ thick mylar sheet and a 25 μ thick aluminum foil which served as the ground shield for the chamber.

The fourth condition was to operate the chamber at high gain. Fig. 6 shows the efficiency of the chamber as a function of voltage. The vertex detector was operated at 2.25 kV.

The stability of the drift velocity and calibration timing for the chamber were measured on-line by assuming a linear "space-time relation", i.e. an algorithm which related the 4 measured drift times of a track traversing the inner band of sense wire layers to: the slope and intercept of the particle's trajectory, the drift velocity, and the time corresponding to zero drift length. This linear relationship is accurate over about 80% of a cell in the VC. Fig. 7 depicts the parameters of the calculation. The space-time relation for the 4 individual layers is represented

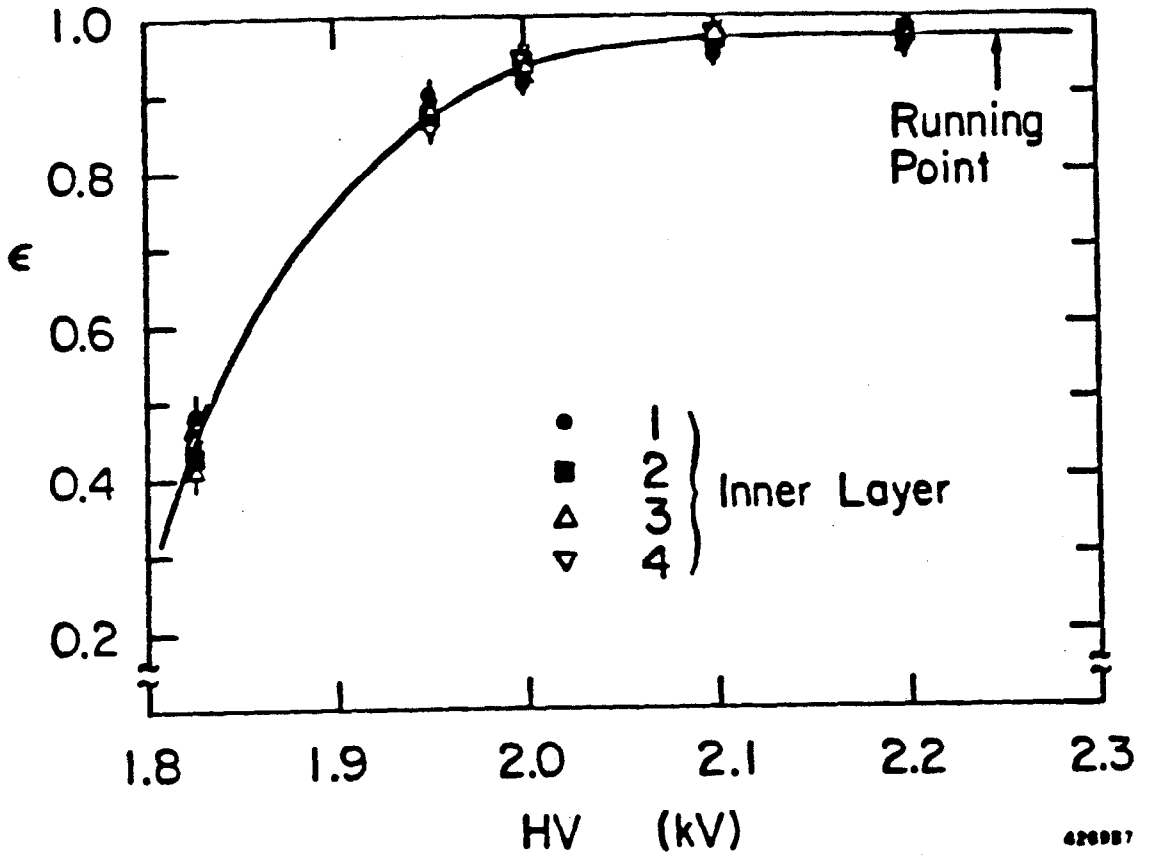

Fig. 6: Vertex chamber efficiency as a function of voltage

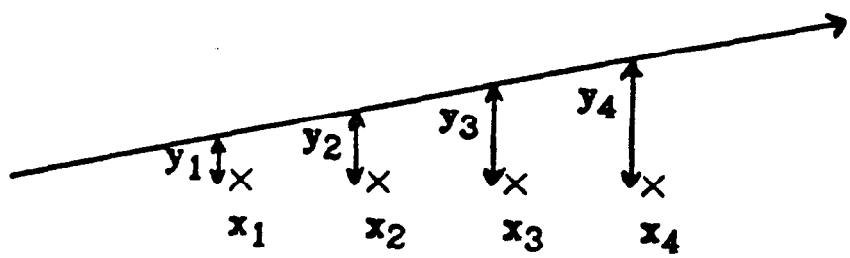

radius of layers x_1, x_2, x_3, x_4

distance to wire y_1, y_2, y_3, y_4

measured times t_1, t_2, t_3, t_4

Fig. 7: Schematic for a charged track passing the first 4 layers of the vertex detector

by the 4 simultaneous equations

$$t_1 = Ay_1 + Bx_1 \pm C + T_0$$
$$t_2 = Ay_2 + Bx_2 \pm C + T_0$$
$$t_3 = Ay_3 + Bx_3 \pm C + T_0$$
$$t_4 = Ay_4 + Bx_4 \pm C + T_0$$

where

A =1/drift velocity

B =slope of track

C =intercept of track

T_0 =measured time of track at y = 0

Fig. 8 shows the distribution of these quantities for a typical data run of two hours duration.

The vertex detector's ability to measure the position of secondary vertices from short-lived particle decays depended critically on the precision with which it allowed a track to be extrapolated to the vicinity of the beam interaction point. The error in such an extrapolation, the so-called "extrapolated-track resolution", can be written

$$\sigma_{ext}^2 = \sigma_{CH}^2 + \sigma_{MCS}^2$$

where σ_{CH} is the measurement error of the chamber layers and σ_{MCS} is the error arising from multiple Coulomb scattering in the beam pipe, chamber gas and wires. The derivation of σ_{MCS} and σ_{CH} is given in chapter 3. The result is that the chamber achieved an accuracy of about 95μ /layer so that $\sigma_{ext}^2(\mu) = [(85)^2 + (95/p(GeV/c))^2]$ in the x-y plane. The first term in brackets corresponds to σ_{CH} and the second to σ_{MCS}. Table 3 shows the amount and type of material along with the thickness in terms of radiation lengths for the various Mark II components.

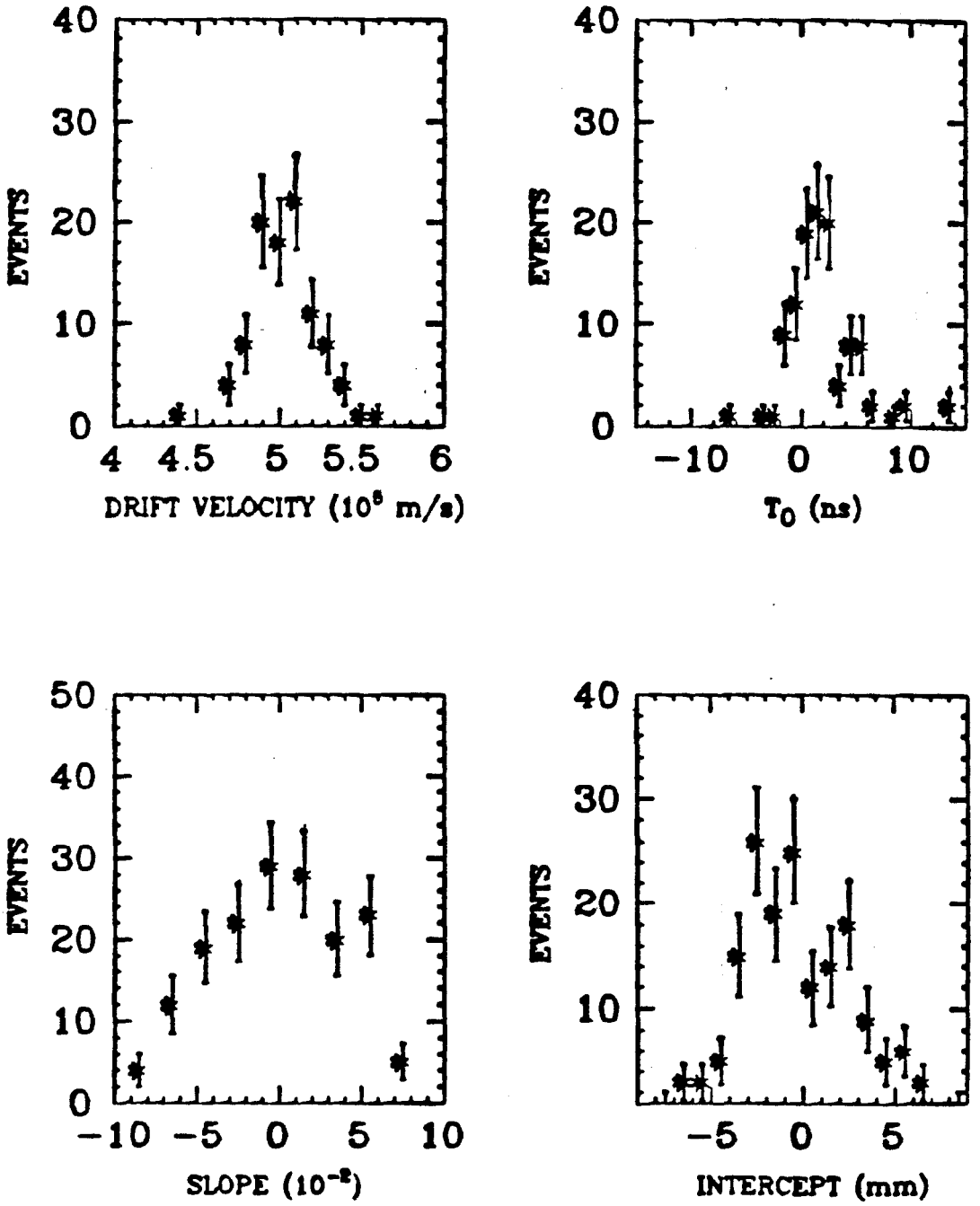

Fig. 8: Measurements of the slope, drift velocity, time 0 offset, and intercept for particle trajectories measured in a single run

Table 3.

MARK II DETECTOR COMPONENTS

(All dimensions in cm)				
Component	Inner Radius	Length	Thickness	Radiation Lengths
Beampipe	7.3	120	0.152	0.006
VC gas	7.8	120	27.1	0.002
VC wires	9.3	120	0.017	0.001
VC Shell	35.0	120	0.18	0.020
Lexan	37.1	179	0.32	0.009
DC gas	37.4	265	113.0	0.009
Outer Can	150.3	265	0.64	0.071
TOF	151.1	304	2.50	0.064
Coil	159.0	412	14.0	1.400
LA module	180.0	380	41.0	14
Muon Steel	235	450	22.9	13.0
Prop.Tubes	269	450	2.6	0.04
Muon Steel	282	450	22.9	13.0
Prop.Tubes	295	450	2.6	0.04

2.2 MAIN DRIFT CHAMBER

The main drift chamber[19] was composed of sixteen concentric cylindrical layers located between radii of 41 and 145 cm relative to the beam line. Six of the sense layers were axial while the other 10 had a $\pm 3°$ stereo pitch in order to provide longitudinal information along the track trajectory. The chamber was housed in a single gas volume with an inner wall made of Lexan and an aluminum outer shell. The chamber covered the polar angle between 32° and 148° with 2π azimuthal acceptance. During data-taking, the chamber operated with a 50/50 argon-ethane gas mixture at a field strength of 900 V/cm on the six innermost layers and a field strength of 500 V/cm on the outer 10 layers. The average spatial resolution of the chamber was $\sim$ 200 μ /layer. This system along with

the VC provided the charged particle tracking essential to detecting charmed mesons and determining their lifetimes in this analysis.

2.3 Time-of-Flight System

Time-of-flight measurements were made with a cylindrical system of 48 scintillation counters situated 1.51 m from the beam line. The scintillators covered the polar angle between 41° and 139° . They were viewed at each end by 2-inch photomultiplier tubes whose outputs provided both timing and pulse height information. Signal pulse heights were used off-line to perform slewing corrections for each tube. The rms resolution on time-of-flight measurements for electrons from Bhabha events was 340 ps. The TOF system was not directly used in this analysis.

2.4 Magnet Coil

The vertex detector, main drift chamber, and time-of-flight system were immersed in a solenoidal magnetic field provided by an aluminum coil at a radius of 1.6 m. The coil was composed of two water-cooled aluminum conductors which sandwiched a layer of insulating material. For the bulk of the data used here, only one coil was powered due to a break in the insulator. The coil provided a field of 2.3 kG. It was monitored by a nuclear magnetic resonance (NMR) probe located just outside the tracking chambers. Variations of the field strength throughout the tracking volume were mapped with a Hall probe before the chambers were inserted into the coil and found to be less than 2.5%. This map, when combined with the absolute field strength as measured by the NMR probe, provided a precise estimate of the field throughout the tracking volume so that the error in the measured track momenta due to the uncertainty in the field was much smaller

than the intrinsic measurement errors in the tracking chambers.

2.5 Liquid Argon Calorimeter

The liquid argon (LA) calorimeter[20–21] consisted of 8 lead-liquid argon shower modules arranged in an octagonal array just outside the magnet coil at an average radius of 1.97 m. Eighteen alternating layers of 2mm thick lead strips and plates with 3 mm gaps for liquid argon formed each module. The lead stacks constituted 14 radiation lengths of material for normally incident particles. The eighteen layers were ganged together, as shown in fig. 9, to provide six samples in depth for a shower; three of the azimuthal angle, two of the polar angle, and one at 45° . The rms energy resolution of these counters for Bhabha event electrons is Δ E/E = $15\%/\sqrt{E}$. In this analysis, the LA system was used for detection and energy measurements of neutral particles.

2.6 Muon System

Four walls of four alternating layers of steel and proportional tubes formed the muon system[22] . These walls were placed above, below, and to either side of the tracking system and LA calorimeters at an average radius of 2.8 m. The modules of proportional tubes were made of extruded aluminum and contained eight triangularly shaped tubes running the full length of the steel used for hadron absorption. Proportional tubes in the first layer of each wall measure the polar angle of a track while layers 2 through 4 measure the azimuth. The outermost layer of the system covered about 45% of 4π. By combining measurements from this system with information from the tracking system, muons were identified with an efficiency of about 85% with a rejection rate for pions of 99% or more. The muon system was not used in this analysis.

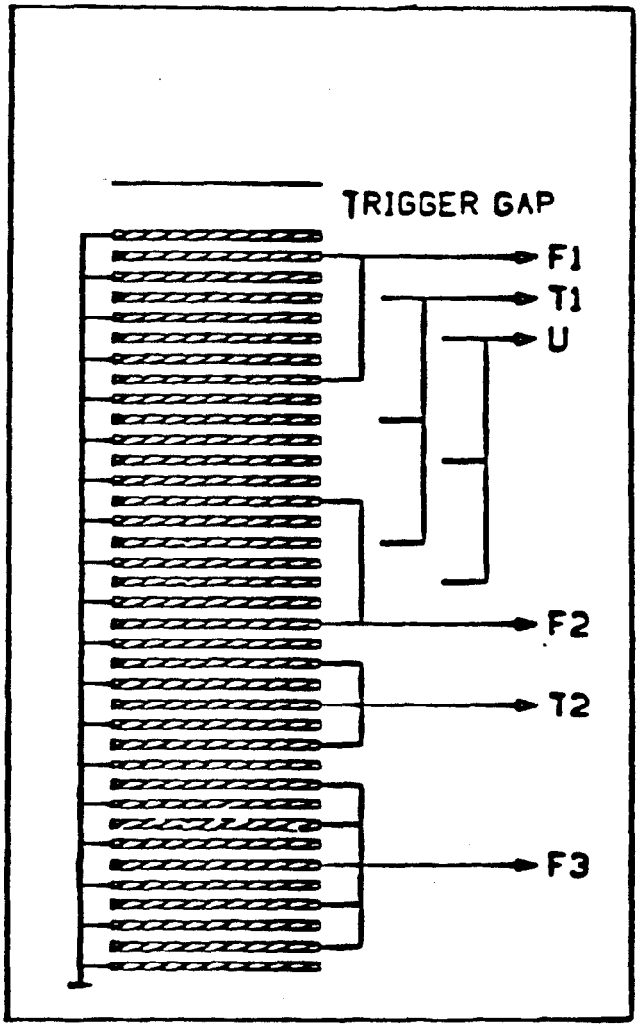

Fig. 9: Cross-sectional view of LA module

2.7 End Cap Calorimeters

Each end of the Mark II was covered by end cap calorimeters composed of two layers of proportional chambers. Each chamber was preceded by lead sheets 2.3 radiation lengths thick. The end caps covered the polar angle between 15° - 40° and 140° - 165° . There was a break in the azimuthal coverage from 4.2 to 5.2 radians for the insertion of a support stand for the magnet flux return. The energy resolution of this system was $\sigma(E)/E \sim 50\%/\sqrt{E}$ for electromagnetic showers. Information from the end cap calorimeters was not used in this analysis.

2.8 Small Angle Tagging System

The small-angle tagging system (SAT) detected charged particles emitted with polar angles between 21 and 82 mrad relative to the beam axis. The SAT counters consisted of 3 layers of planar drift chambers, 3 layers of scintillation counters which defined the acceptance for a SAT counter, and a lead scintillator shower counter. Each layer of the planar drift chambers had pairs of sense wires placed above an inductive delay line. This combination provided measurements of particle trajectories with an accuracy of about 300 μ in the coordinates perpendicular to the beam. The lead scintillator shower counter had eighteen layers of $\frac{1}{4}''$ lead sheets interspersed with $\frac{1}{2}''$ plastic scintillator. This system served as an electromagnetic calorimeter with an energy resolution of $\sim 15\%/\sqrt{E}$ (GeV). The acceptance counters on either side of the detector and the calorimeters were used to measure luminosity by "tagging" small angle collinear Bhabha events[23] .

2.9 Beam Position Monitor

Lifetime measurements at e^+e^- storage rings depend critically on knowledge of the beam-beam interaction point or charge-weighted center of the beam relative to the center of the detector. Two beam position monitors (BPM) were

installed on the Mark II at the same time as the vertex detector installation. One monitor sat 4.9 m ahead of the detector along the beam line while the other sat 4.9 m behind the Mark II . Each position monitor was formed of 4 copper buttons which protruded a small distance into the beam pipe; one on top, one on the bottom, and one on either side of the pipe. Each beam bunch crossing induced voltages on the buttons. The vertical (horizontal) position of the beam relative to the buttons was determined by measuring the ratio of induced voltages on the two buttons on the vertical (horizontal) axis. Since the radial component of the Mark II solenoidal field was quite small, the beam positions measured ahead and behind the detector were used to interpolate the beam position at the interaction point.

The induced voltage pulses on the buttons were passed through 100 feet of RG223 cable into a device which stretched and shaped the pulses before sending them to an analog-to-digital converter (ADC). The outputs of the ADC for each of the eight buttons was scanned and recorded on magnetic tape once every four minutes. At each four-minute interval, 32 voltage measurements were made for each of the 3 PEP bunches. An offline program used these 32 values to produce an average position for each of the 3 bunches. The average of the bunch positions was then used as the beam position for that 4-minute interval. The accuracy of voltage measurements by the ADC and the stability of the gain in the system limited the position accuracy of the BPM to $\sim 50\ \mu$. Since we desired the beam position relative to the main drift chamber origin, the beam positions used in this analysis were determined by a method to be described in chapter 3. The beam position was found to be stable over the course of several runs. Stability of the beam position within a run was checked by measuring the rms spread of the BPM measurements. Runs which had an rms spread greater than 250μ in x

or 150μ in y were eliminated from the data sample.

2.10 Event Trigger

The Mark II operated with a two-level trigger system[24–25] designed to minimize the deadtime of the detector while maximizing the probability for detection of events of interest. The first level, or primary, trigger was geared to decision-making on the time scale of 2.4 μsec, the repetition rate for beam collisions at PEP. The primary trigger required either a charged primary, neutral primary, or SAT trigger in coincidence with a beam crossing signal (BX) from PEP. The BX signal came from a beam pickup electrode situated inside the beam pipe a small distance away from the beam interaction point. A charged primary trigger was generated whenever 9 of 21 layers of the vertex detector - main drift chamber system recorded hits which were in a pattern which was designed to minimize the number of false tracks from stray hits in the drift chambers while maximizing the efficiency for true charged tracks. The pattern was:

at least 2 out of 4 inner VC layers
at least 1 out of 3 outer VC layers
at least 2 out of 4 from DC layers 1-4
at least 1 out of 3 from DC layers 5-7
at least 1 out of 3 from DC layers 8,10,11
at least 2 out of 4 from DC layers 12-15.

In addition, at least one TOF counter latch was required to be in coincidence with the drift chamber hits. The neutral energy trigger required a minimum amount of pulse height be found in 2 or more of the 8 LA modules or both of the endcap calorimeters, while the SAT trigger required hits in the drift chambers and shower counters of the SAT system that signalled a small-angle, back-to-back

Bhabha event.

The secondary trigger used a hardware track finding processor to determine whether the pattern of VC-DC hits constituted a suitable track. This processor made a rough measurement of the track curvature. This gave an estimate of the track momentum and allowed a check to see which of the latched TOF counters, if any, could be associated with the track. For charged primary triggers, the secondary trigger demanded that at least 2 tracks with momenta $> 100 - 200$ MeV/c be found within the central 70% of the solid angle covered by the detector before writing the event out to tape. For neutral primary triggers, the secondary trigger required 1 GeV or more of energy be deposited in at least 2 of the LA modules or ≥ 3 GeV in the end caps. SAT primary triggers were prescaled by a large factor (usually a factor of 16) before being written to tape.

2.11 Event Reconstruction and Particle Tracking

The offline charged particle tracking routines reconstructed the 3-dimensional orbits of tracks from the measured drift times of hit wires in the VC - DC tracking chambers and first approximations to the position, momentum, polar and azimuthal angles (θ and ϕ), and the distance of closest approach to the origin of the orbit. An additional parameter was included to allow for a kink in the track due to multiple Coulomb scattering in the outer wall of the vertex detector. A pattern-recognition program associated hit drift wires which might belong to a single track and made a first attempt at resolving left-right ambiguities. The distances of closest approach (DCA's) of the track to the hit chamber wires associated with it were calculated using the orbit parameters and known positions of the chamber wires. A chi-square was formed from the calculated DCA's and the DCA's derived from the measured drift times. A minimization procedure then iterated the orbit parameters until their optimal values were determined.

This system reconstructed tracks with an efficiency of 99.6% over 70% of the total solid angle. For a 2.3 kG magnetic field, the momentum resolution was found to be

$$\sigma_p/p = \sqrt{(.025)^2 + (.010p)^2}$$

for tracks which were not constrained to pass through the beam interaction point. The errors in ϕ for high-momentum tracks are shown in fig. 10. The mean value is $< \sigma\phi >= .5$mr. The momentum resolution could be improved by $\sim$ 15% by constraining tracks to pass through the beam spot.

The above procedure possessed the optimal track-finding efficiency and momentum resolution for charged tracks. It did not provide the optimal track parameters for lifetime measurements, however, since the vertex detector was simply treated as a high-resolution extension of the main drift chamber. This allowed the imperfections of the main drift chamber to adversely affect the track fit. Although these imperfections were irrelevant to track fits extrapolated to the vicinity of the origin with an error of $\sim$500 μ , they could be quite significant with the inclusion of the vertex detector. Thus, after the track-finding algorithm was applied and an appropriate lifetime sample of events selected, tracks identified as coming from interesting decays were refit by allowing a separate track fit in the vertex detector and main drift chamber. These fits were allowed to be discontinuous by as much as 0.3 milliradians in ϕ and 200 μ in the x-y plane. The advantage of this algorithm is that the vertex detector, with its much greater resolution and smaller systematic foibles, was primarily responsible for determining the ϕ and x-y position of the track while optimal use was made of the improved curvature information provided by the vertex detector - main drift chamber fit. Fig. 11 shows a plot of the separation distance of Bhabha event tracks fit with and without the separate fit tracking algorithm. There is little improvement in

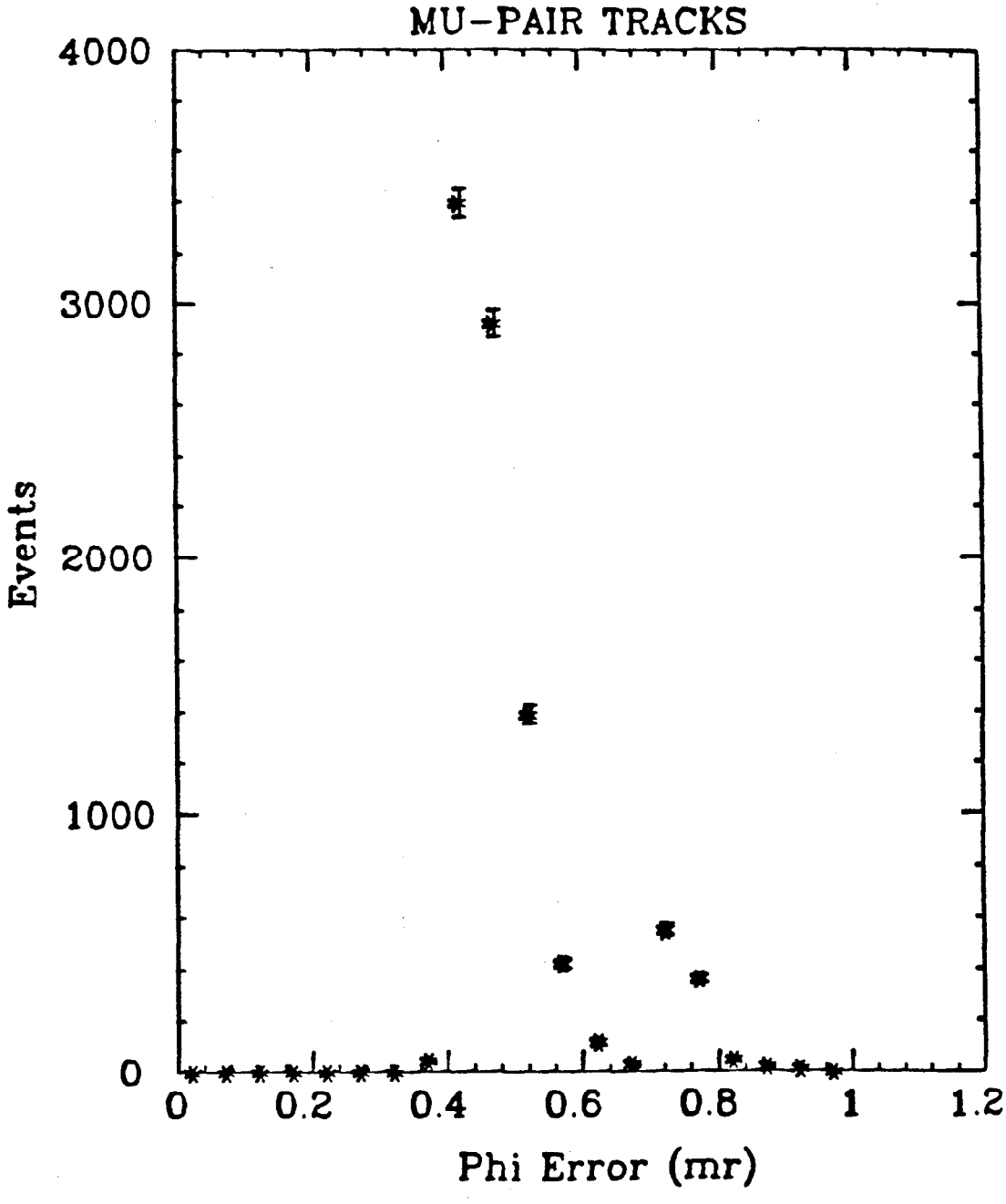

Fig. 10: Tracking error in ϕ for mu pair events

the resolution, but a noticeable improvement in the offset from 0 is evident.

2.12 Monte Carlo Simulation

Event simulation for the Mark II detector is done by Monte Carlo routines which generate the raw data corresponding to the final state particles of events which can be seen at PEP energies. The final state particles are assigned momenta, masses, and charge according to the known or assumed physics properties of the initial state reactions that produces them. The frequency and phase space distribution of these particles correspond to the measured (where measurements existed) or assumed differential cross sections characteristic of the type of event being simulated. For hadronic event simulations, the initial quark-anti-quark state is generated using a program QCDJET which includes QCD contributions up to third order in the coupling constant, α_s. The quark, anti-quark, and any radiated gluons are converted into jets of mesons and baryons according to a Field-Feynman fragmentation scheme. In this scheme, an initial quark is combined with an anti-quark pulled from a quark-anti-quark pair produced from the vacuum. The combination becomes a conventional meson or baryon with a total momentum chosen on the basis of a given functional form (i.e. a fragmentation function). The leftover quark is then combined with a partner from another quark-anti-quark pair from the vacuum. The process is continued until there is insufficient energy left to form another particle. The probability for producing a $u-\bar{u}, d-\bar{d}$, or $s-\bar{s}$ pair from the vacuum is a parameter of the model which is set by the experimenter. The ratio of vector to scalar mesons produced, the mean transverse momentum (relative to the jet axis), and the fragmentation function are also model parameters. These parameters have been adjusted to give the best representation of PEP hadronic events.

After its production, each particle is projected through the various detector

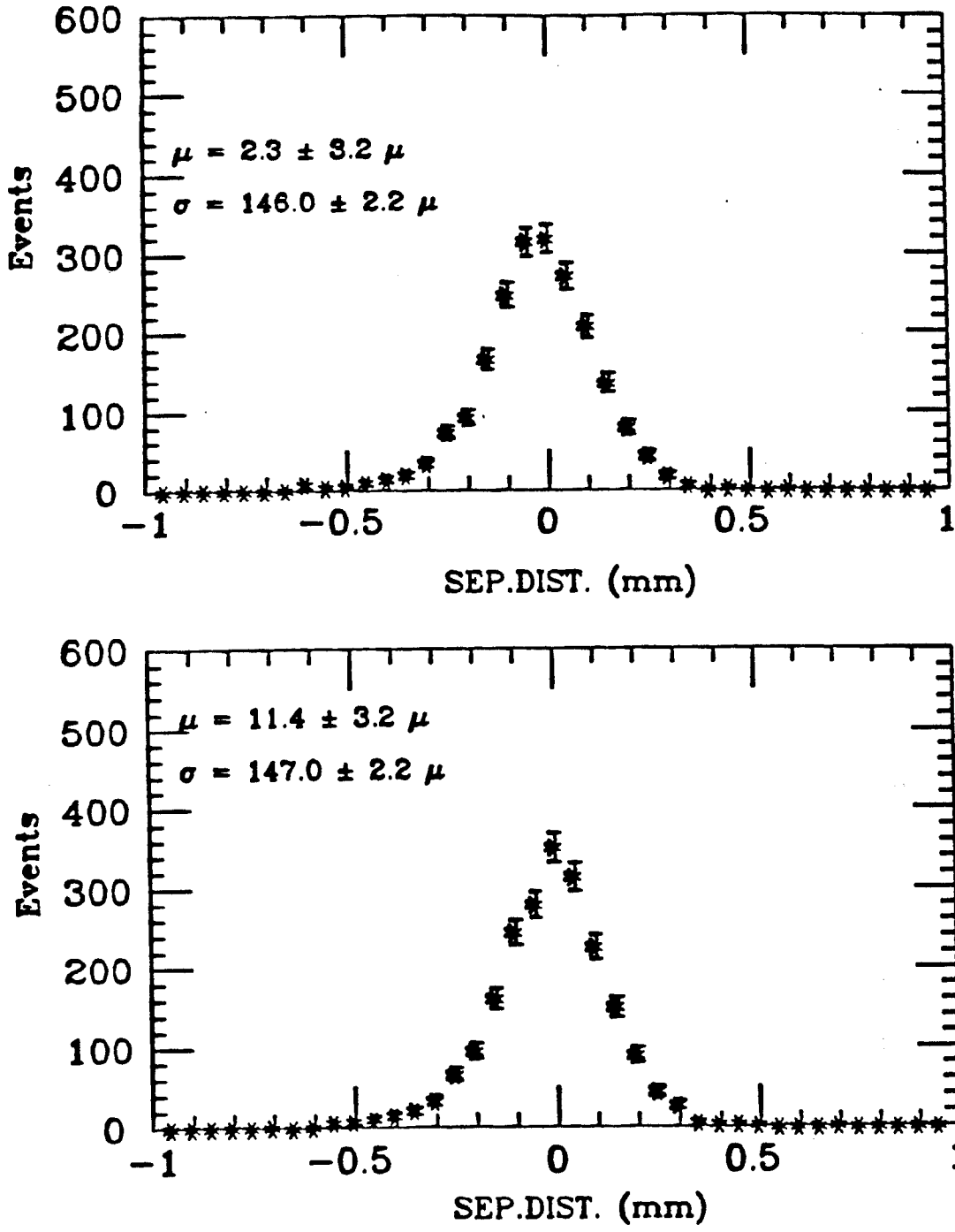

Fig. 11: Separation distance between Bhabha tracks in the vicinity of the beam position for

a. optimal vertex chamber tracking

b. normal tracking

elements and allowed to decay according to its known branching ratios, lifetime, and spin. Multiple Coulomb scattering, nuclear interactions, and particle momenta and charges are taken into account in calculating the particle trajectories. As a particle traverses a simulated detecting element such as a drift chamber wire or TOF scintillator, a hit is registered or not registered according to a Gaussian distribution representing the efficiency of the detector element as a function of distance from the particle track. The drift times generated by a hit are smeared to simulate the measured resolution in the vertex chamber and DC. The EGS shower code[26] is used to simulate electromagnetic showers in the LA calorimeters. The energy deposited as a function of depth in the LA modules is used to simulate measured pulse heights in the LA system. The raw data generated by the detector simulation routines are processed in the same fashion as the real data by the assorted subsystem tracking codes. Produced momenta and energies have been checked to ensure that they agree with the resolution observed in real data processing.

3. Tools for Making Lifetime Measurements

Before defining an algorithm for measuring short lifetimes, we must create tools which will provide crucial information about the decays of interest. For example, in order to derive a decay length for a particular event, we must know the position of the decay and the origin of the event. In this study, the decay position is simply the vertex position of the decay tracks of a charmed meson. We will approximate the origin of the event as being the charge-weighted center of the beam (henceforth called the beam position). Since this is a statistical measurement, the errors on these quantities are also an essential part of the procedure. This chapter will discuss the "tools of the trade" which enable us to derive information on the beam position, decay vertex, measurement errors, etc. It will also present evidence for the integrity of the vertex chamber as a measuring device. Such integrity is essential to a thorough understanding of the systematic errors on the final answer for the D^0 and D^+ lifetimes.

3.1 Resolution of Vertex Chamber Tracking

The resolution of continuous tracking devices such as bubble chambers and emulsions is limited only by the size of the track a charged particle makes in such a device. However, for devices such as drift chambers, which track a particle's trajectory by measuring its position at discrete intervals, the resolution is limited by both the intrinsic accuracy of the position measurements (typically a factor of 2 or more greater than that of emulsions or bubble chambers) and the proximity of the first measurement point to the origin of the track. To see this, consider the problem depicted in fig. 12 in which we wish to find the best estimate of the extrapolated track position near the origin and the error on that estimate. It is assumed that the track position has been measured only in the x-y plane at

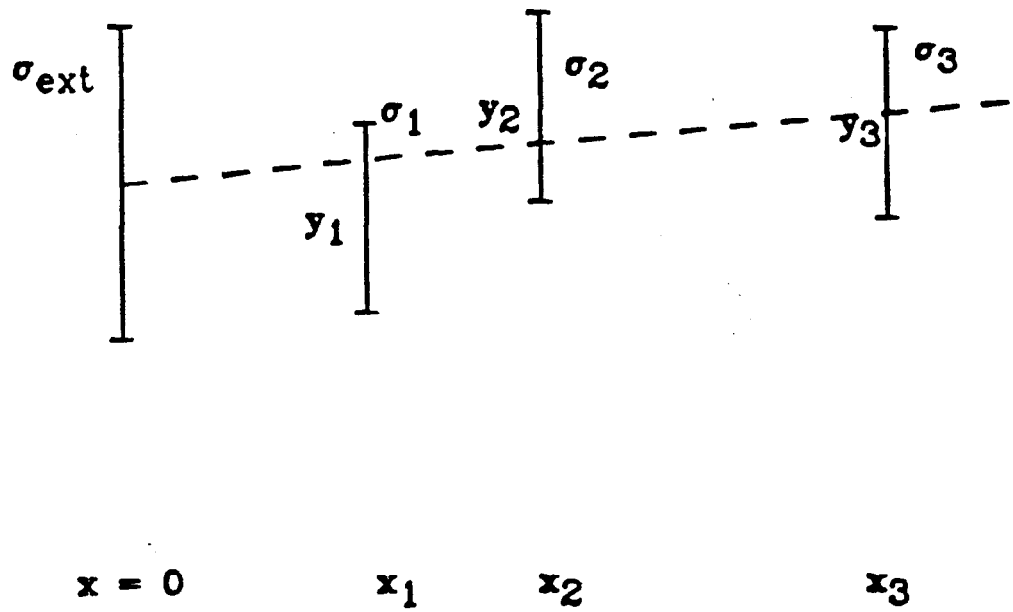

Fig. 12: Extrapolation of a track to the origin for discrete measurement devices

N discrete intervals, x_i, with an error of σ_i on each measurement. If we assume that the particle trajectory is a straight line, then it is simple to perform a linear least-square fit to the function y = a + bx to derive the best estimates of the slope b and intercept a. These, in turn, will give us the best estimate of y for x= 0. The solution is as follows: define the chi-square function

$$\chi^2 \equiv \sum\left(\frac{\delta y_i}{\sigma_i}\right)^2 = \sum\left[\frac{1}{\sigma_i^2}(y_i - a - bx_i)^2\right].$$

The best estimates of a and b are those which minimize the χ^2. Thus, set

$$\frac{\partial}{\partial a}\chi^2 = -2\sum_{i=1}^{N}\left[\frac{1}{\sigma_i^2}(y_i - a - bx_i)\right] = 0$$

and

$$\frac{\partial}{\partial b}\chi^2 = -2\sum_{i=1}^{N}\left[\frac{x_i}{\sigma_i^2}(y_i - a - bx_i)\right] = 0.$$

After some rearrangement, we have a pair of simultaneous equations.

$$\sum_{i=1}^{N}\frac{y_i}{\sigma_i^2} = a\sum_{i=1}^{N}\frac{1}{\sigma_i^2} + b\sum_{i=1}^{N}\frac{x_i}{\sigma_i^2}$$
$$\sum_{i=1}^{N}\frac{x_i y_i}{\sigma_i^2} = a\sum_{i=1}^{N}\frac{x_i}{\sigma_i^2} + b\sum_{i=1}^{N}\frac{x_i^2}{\sigma_i^2}$$

The solution is

$$a = \frac{1}{D}\left(\sum_{i=1}^{N}\frac{x_i^2}{\sigma_i^2}\sum_{i=1}^{N}\frac{y_i}{\sigma_i^2} - \sum_{i=1}^{N}\frac{x_i}{\sigma_i^2}\sum_{i=1}^{N}\frac{x_i y_i}{\sigma_i^2}\right)$$
$$b = \frac{1}{D}\left(\sum_{i=1}^{N}\frac{1}{\sigma_i^2}\sum_{i=1}^{N}\frac{x_i y_i}{\sigma_i^2} - \sum_{i=1}^{N}\frac{x_i}{\sigma_i^2}\sum_{i=1}^{N}\frac{y_i}{\sigma_i^2}\right)$$

where

$$D = \sum_{i=1}^{N}\frac{1}{\sigma_i^2}\sum_{i=1}^{N}\frac{x_i^2}{\sigma_i^2} - \left(\sum_{i=1}^{N}\frac{x_i}{\sigma_i^2}\right)^2.$$

From ref.[27] we find that defining a covariance matrix σ_{ij} as

$$\sigma_{ij}^{-1} = \sum_{k=1}^{2}\frac{f_i(x_k)f_j(x_k)}{\sigma_k^2}$$

where $f_1(x) = 1$ and $f_2(x) = x$, allows us to express the variance on an extrapolated value of y at point x as,

$$\overline{(y-\bar{y})^2} = \sum_{ij} \sigma_{ij} f_i(x) f_j(x)$$

Thus, the contribution to the extrapolated track resolution from measurement error for a set of cylindrical drift chambers with radii $x_1, x_2, ..., x_N$ is

$$\sigma_{CH} = \sqrt{\frac{1}{D}\left(\sum_{i=1}^{N} \frac{x_i^2}{\sigma_i^2}\right)}$$

for the value of y at x= 0.

The error contribution from multiple Coulomb scattering depends on the deflection angle imparted to a track due to a scatter and the lever arm provided by the distance from the scatter to the next measurement point (see fig. 13). If we define $d\theta^2$ as the differential mean square deflection angle for a Coulomb scatter in the material between r and r + dr (note that we are working only in the x-y plane here), then

$$\sigma_{MCS}^2 = \int_0^{r_1} r^2 d\theta^2 + \sum_{i=1}^{N-1} \frac{r_i^2}{(r_{i+1}-r_i)^2} \int_{r_i}^{r_{i+1}} (r_{i+1}-r)^2 d\theta^2.$$

We now set

$$d\theta^2 = \left(\frac{.015}{\beta p(GeV/c)}\right)^2 \frac{dr}{x_0}$$

where p is the track momentum in units of GeV/c and x_0 is the radiation length of the scattering material at radius r.

For the Mark II vertex detector, the critical parameters are given in tables 2 and 3 in chapter 2. Using these values and the formulae shown above,

$$\sigma_{CH} = 85\mu$$
$$\sigma_{MCS} = 95\mu/p(GeV/c).$$

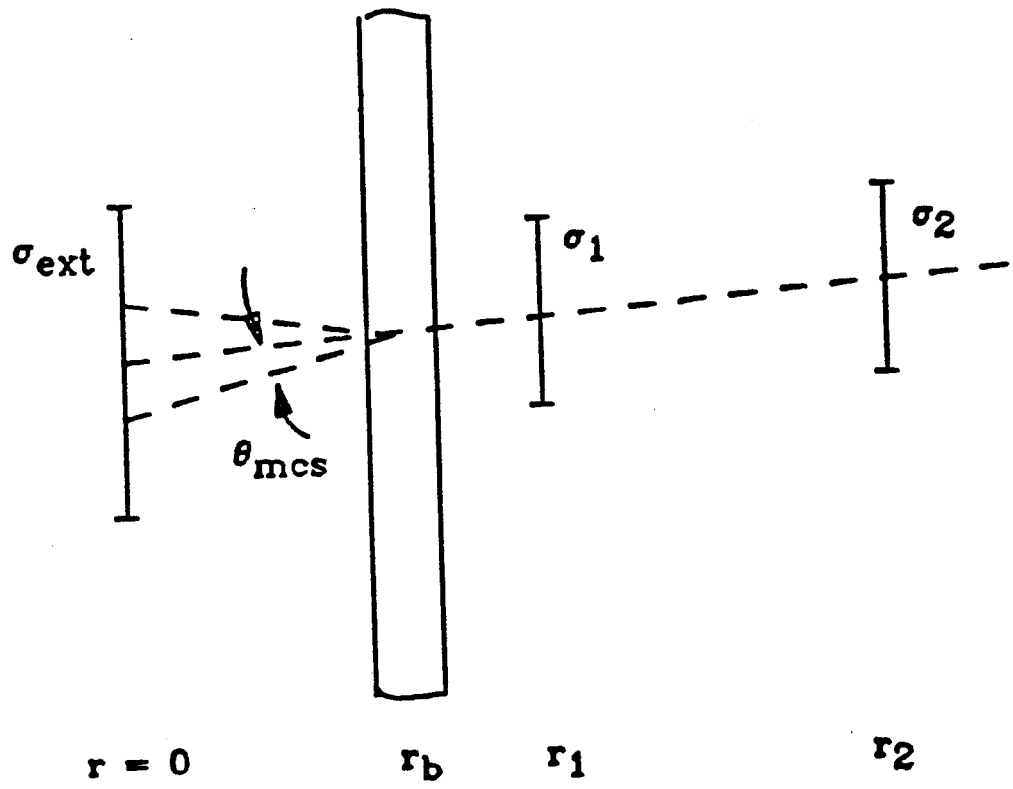

Fig. 13: Extrapolated track error from multiple Coulomb scattering

The experimental verification of the intrinsic measurement accuracy of the VC can be seen in fig. 14. It is a plot of the separation distance (in the vicinity of the beam position) between Bhabha tracks. Since these tracks were required to have momenta greater than 12 GeV/c, multiple Coulomb scattering provides only a small source of error on the extrapolated track position. Thus, if the overall operation of the chamber is understood, then the mean of this plot should be close to zero and have a width given by $\sqrt{2} \cdot \sigma_{CH}$. The mean of fig. 14 was found to be -3μ . The width is 124$\pm$3μ, which corresponds to an intrinsic extrapolation error of 88μ.

It should be noted that the plot represents data only from the sections of the chamber which excluded the I2B section. I2B is that section of the inner layers of the chamber between 72 and 144° . This section of the chamber was operated at about 200 V below the nominal 2.25 kV of the rest of the chamber because of "glow" problems which caused excessive current draw at higher voltages. The lower voltage produced less gain and therefore reduced resolution in this section. The resolution as measured by the tracking residuals was found to be $\sim$ 150μ for I2B for most of the data sample.

3.2 Beam Position Determination

We will use the beam position as a constraint on the origin of our charmed mesons. Although a better estimate of the event origin could, in principle, be gotten from the event tracks which accompany the D^0 or D^+ decay tracks, such an event origin could be biased by the fact that there must be one other charm decay in the event. Since that decay is also be expected to have a finite lifetime, the accuracy of the vertex position would be difficult to estimate without making a priori assumptions about the charm lifetime. For this reason it was decided that the beam position would be a better origin in terms of understanding the

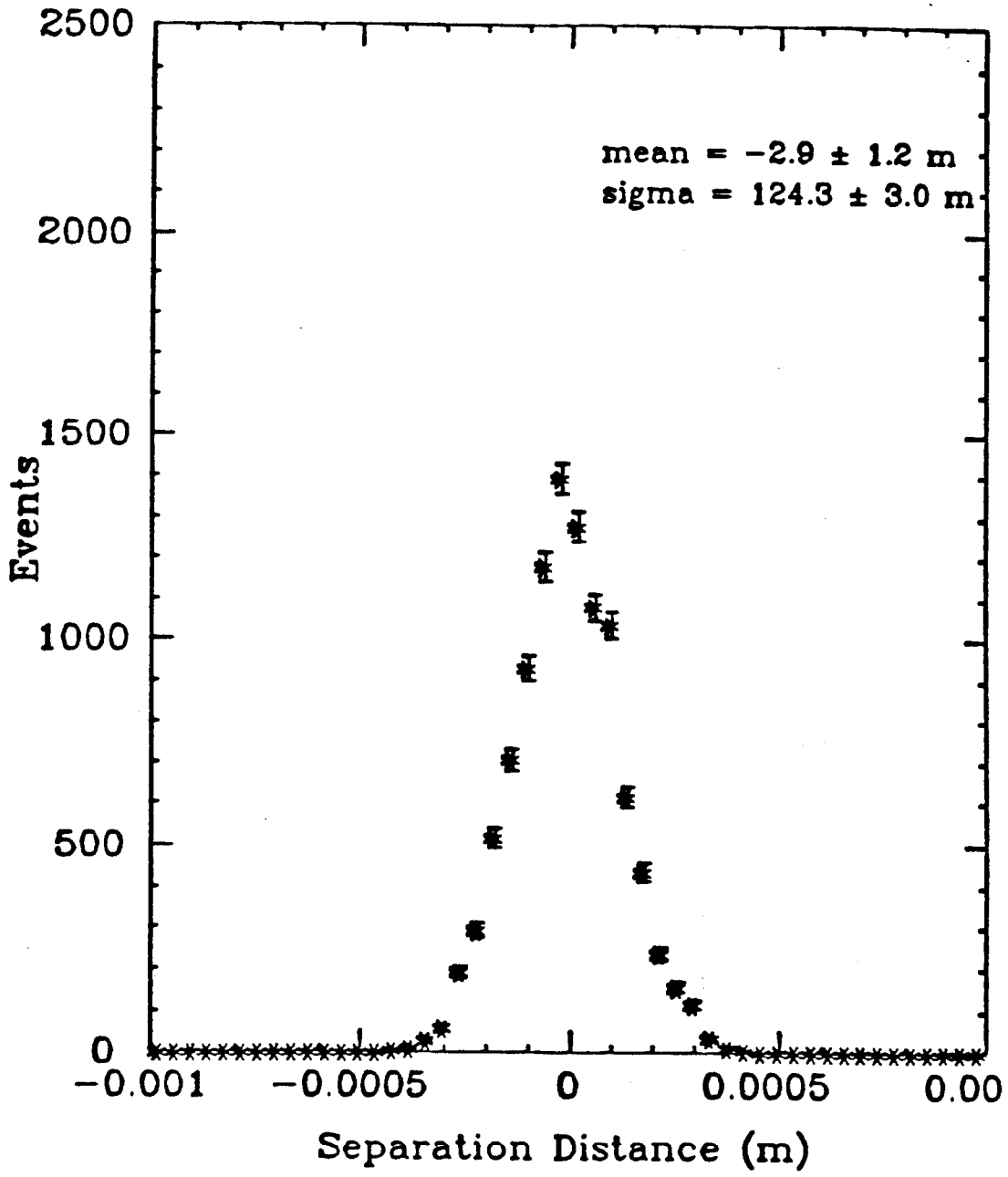

Fig. 14: Separation distance of Bhabha tracks in the vicinity of the beam position

systematic error on the measurement.

In principle, the beam position monitor or BPM could provide the most accurate estimate of the beam interaction point, since its resolution was far smaller than the intrinsic error in the lifetime measurement for an individual event. The BPM, however, was susceptible to both sudden and long term gain changes so that it alone could not be used as an absolute standard. Thus, ORCALC, a program for determining the optimal average beam position for a data run from event tracks was developed. The mean beam position from the BPM measurements made within a run was then fixed to the ORCALC position. This allowed the use of the BPM measurements taken every four minutes during a run to be used as offsets to the average beam position. In this way, small beam position changes which occurred on short time scales could be accounted for properly.

ORCALC finds the mean beam position in the x-y plane (transverse to the beam line) by determining the point which minimizes a chi-square formed from the projected impact parameters with their errors, for a large number of tracks. As depicted in fig. 15, we define the impact parameter, δ, in terms of the x,y values, x_{DCA}, y_{DCA} of the distance of closest approach relative to the drift chamber origin, the azimuth angle, ϕ, of the track, and the unknown beam positions x_B, y_B as

$$\delta = (y_B + x_{DCA} - y_{DCA})cos\phi - x_B sin\phi.$$

with error

$$\sigma_\delta = \sqrt{\sigma_{ext}^2 + \sigma_{Bx}^2 \sin^2\phi + \sigma_{By}^2 \cos^2\phi}.$$

Then, for N tracks, we define the chi-square

$$\chi^2 = \sum_i^N \left(\frac{\delta_i}{\sigma_i}\right)^2.$$

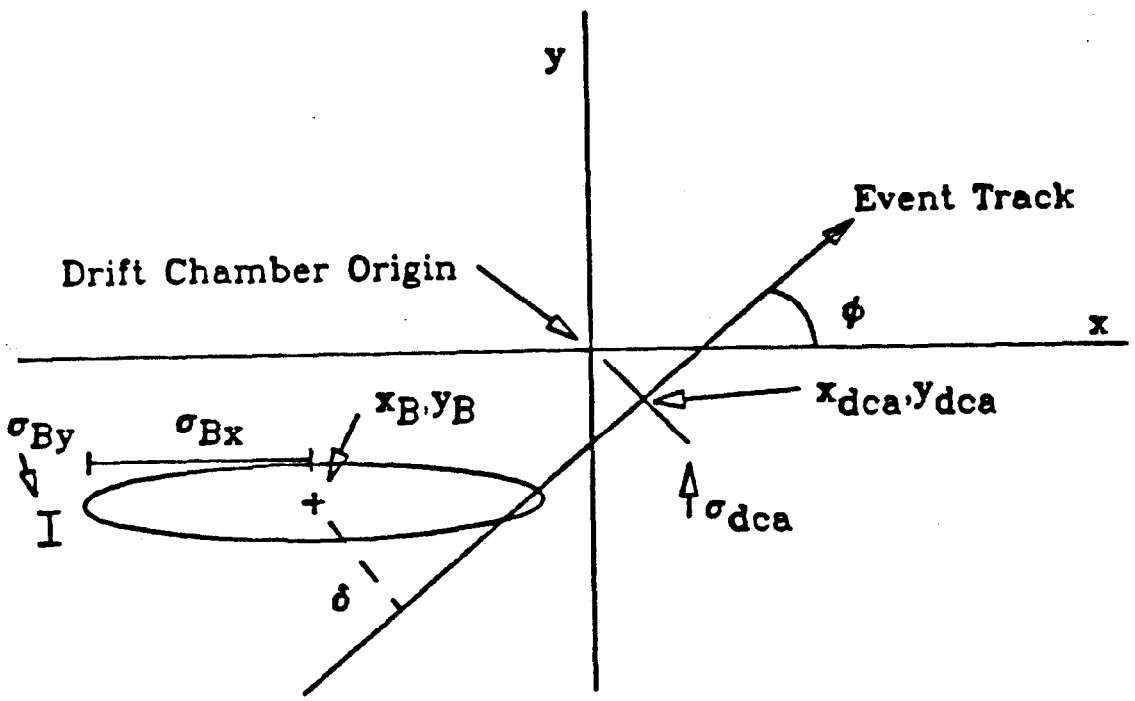

Fig. 15: Relation between the impact parameter, δ and the x,y position of the track at its point of closest approach to the origin

We now solve for the values which minimize the χ^2 by getting the values of x_B, y_B for which

$$\frac{\partial \chi^2}{\partial x_B} = \frac{\partial \chi^2}{\partial y_B} = 0.$$

The solution is given by the expression,

$$x_B = \frac{(EC - AF)}{(A^2 - BC)}, \quad y_B = \frac{(E + Bx_B)}{A}$$

where

$$A = \sum_{i=1}^{N} \left| \left(\prod_{j=1}^{N} \sigma_{ij}^2 \right) \sin\phi_i \cos\phi_i \right|$$

$$B = \sum_{i=1}^{N} \left| \left(\prod_{j=1}^{N} \sigma_{ij}^2 \right) \sin\phi_i \right|$$

$$C = \sum_{i=1}^{N} \left| \left(\prod_{j=1}^{N} \sigma_{ij}^2 \right) \cos^2\phi_i \right|$$

$$E = \sum_{i=1}^{N} \left| \left(\prod_{j=1}^{N} \sigma_{ij}^2 \right) \left(y_{i\ DCA} - x_{i\ DCA} \tan\phi_i \right) \sin\phi_i \cos\phi_i \right|$$

$$F = \sum_{i=1}^{N} \left| \left(\prod_{j=1}^{N} \sigma_{ij}^2 \right) \left(y_{i\ DCA} - x_{i\ DCA} \tan\phi_i \right) \cos^2\phi_i \right|$$

with $\sigma_{ii} = 1$ and $\sigma_{ij} = \sqrt{(\sigma_{j\ x} \sin\phi_i)^2 + (\sigma_{j\ y} \cos\phi_i)^2 + \sigma_{j\ DCA}^2}$ for $i \neq j$.

3.3 Impact Parameter Check

The distribution of impact parameters provides a final check on the integrity of the chamber and the accuracy of the beam position determination. In fig. 16 we see the final result. The plot was made using tracks from Bhabha events. The impact parameter for each track was put into one of 60 bins in phi corresponding to the phi angle of the track. After sufficient statistics had been gathered, the mean impact parameter and its error was found for each bin. The means and errors are plotted in fig. 16. We note immediately the phi symmetry of the chamber. No systematic shift of $> 20\mu$ in impact parameters occurs

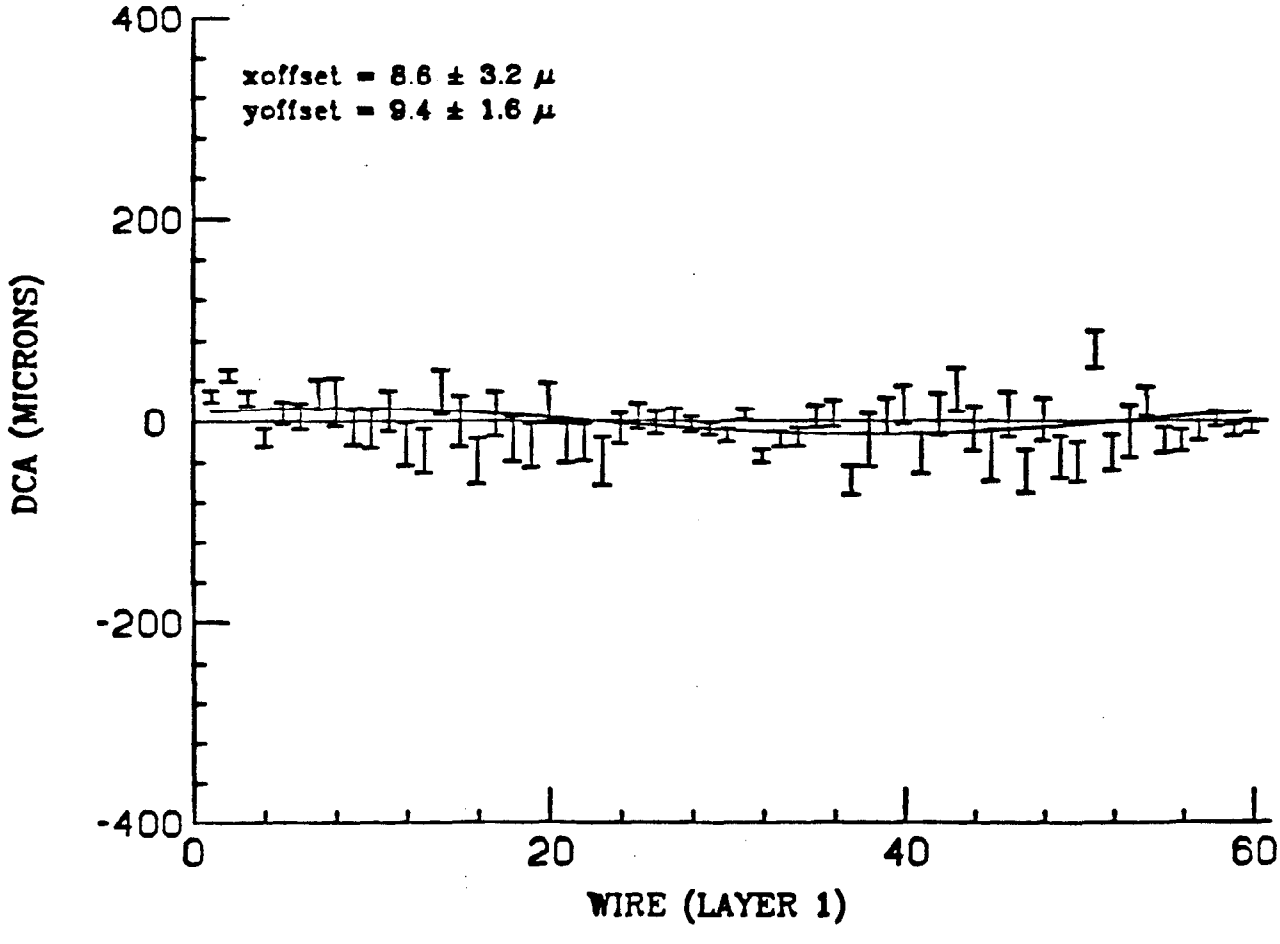

Fig. 16: Mean impact parameter of Bhabha tracks as a function of ϕ. The solid curve shows the expected shape of the distribution for positive offsets in x and y of ~ 8 and 9μ , respectively

at any phi value. The asymmetry in the errors as a function of ϕ reflects the asymmetry in the beam dimensions in x and y as discussed below. This is rather important for lifetime measurements in cylindrical drift chambers since it is easy to show that some systematic effects which might pull lifetimes tend to cancel if the chamber is phi symmetric. Thus, many small systematic effects tend to cancel. The data in fig. 16 has been fit to a roughly sinusoidal distribution which is parametrized by systematic offsets in x and y. The solid curve in fig. 16 shows the result. A small systematic shift of about 10μ is observed in x and y. This is presumed to come about largely because of the I2B section of the chamber. The effects of low-voltage in this section have been largely corrected for, but a small systematic shift is still evident. It will be evident from the discussion of the D^0 and D^+ vertex errors in chapter 5 that such small shifts are negligible in evaluating the lifetimes. Since most of the tracks we will deal with for the D^0 and D^+ mesons are at a relatively lower momentum, this impact parameter check has also been done for tracks from hadronic events. We observe very similar results.

3.4 Determination of the Beam Size

Once the beam position has been determined for a large number of runs, then one can also measure the size of the beam envelope. By design, the beam bunches at PEP are thin ribbons roughly 500μ across in the horizontal direction, x, and 40-60 μ across in the y, or vertical direction. Since the beam spread contributes to the error on the extrapolated track position relative to the beam position, it is possible to use tracks from events to get an accurate estimate of the actual beam size. For example, the error on the impact parameter of a charged track relative to the beam center is

$$\sigma_t = \sqrt{\sigma_{ext}^2 + \sigma_{Bx}^2 \sin^2\phi + \sigma_{By}^2 \cos^2\phi}.$$

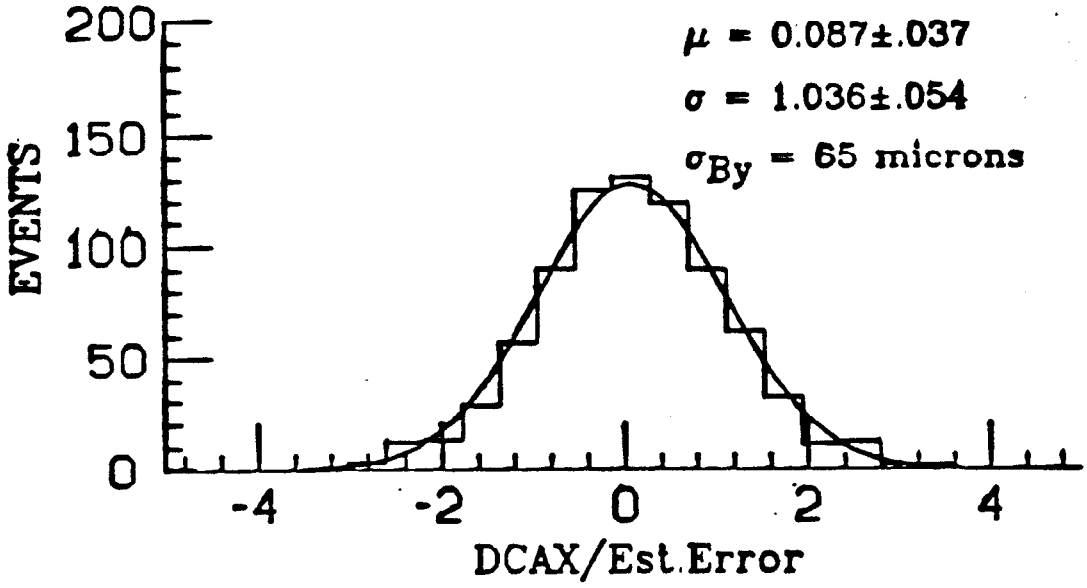

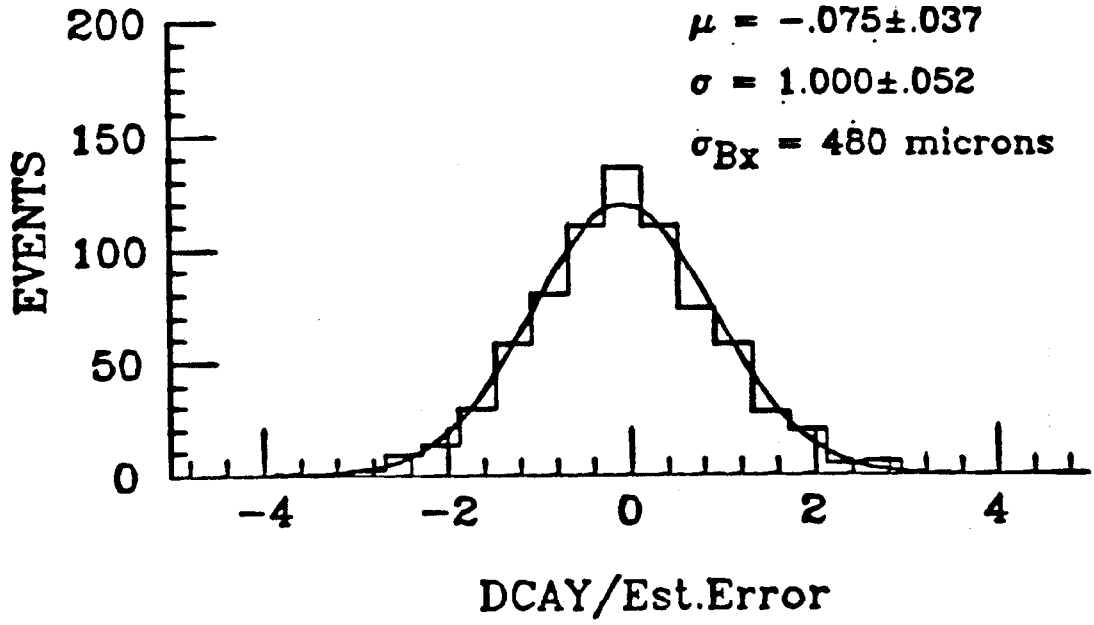

Fig. 17: Measurements of impact parameter/estimated error for

a. horizontal tracks

b. vertical tracks

where σ_{ext} is the extrapolated track error described in section 3.1 and σ_{Bx}, σ_{By} are the horizontal and vertical beam dimensions. Assuming that σ_{ext} is calculated correctly, we have estimated σ_{Bx} and σ_{By} by examining the impact parameter distribution for Bhabha event tracks which are within 100 mr of the y axis and x axis, respectively. Fig. 17a and b show the distribution of impact parameters divided by estimated errors for these vertical and horizontal tracks. The distributions are best fit by Gaussians of unit width for $\sigma_{Bx} = 65\mu$ and $\sigma_{By} = 480\mu$, respectively. The error on the beam size determination from this method is about 10μ . It should be noted that the distributions have essentially no non-Gaussian tails. Since the beam position is determined once per run, this proves that the beam positions are stable at least to the order of the beam widths observed over the course of most runs.

3.5 Vertex Reconstruction

We want to estimate the position of the decay vertex of a charmed meson in order to calculate its proper decay time. Thus, we must find an algorithm which produces the most probable estimate of that vertex position from the information provided by the decay tracks of the meson. We begin a description of such an algorithm with a short synopsis of the charged track information available from the Mark II tracking software.

A charged track that traversed the tracking chambers followed a helical path which is parametrized by 6 variables: the azimuth angle, ϕ, the reciprocal of the momentum transverse to the beam line, $\kappa \equiv \frac{1}{pcos\lambda}$, (where $\lambda = 90°$ minus the polar angle, θ), tanλ, and the x (horizontal), y (vertical), and z (electron beam direction) position of a point on the track. These quantities are usually evaluated at a point close to the beam interaction point. It can easily be shown that only 5 of these quantities are independent since the orbit defines a continuum of points

in one dimension. Thus, the track position is represented by two quantities, ξ and η, with η measured along the magnetic field direction, $\hat{h}$, and ξ along a direction defined by the tangent to the track orbit, $\hat{t}$, and $\hat{h}$ as

$$\hat{\xi} = \frac{\hat{t} \times \hat{h}}{|\hat{t} \times \hat{h}|} \quad , \qquad \hat{\eta} = \hat{h}.$$

The coordinates ξ, η are measured from the track position determined in the single track fit. Their errors and the errors on ϕ, κ, λ go into the 5×5 track error matrix obtained in that fit. Thus, for the nominal single track fit, $\xi = \eta = 0$ with uncertainties given in the error matrix. When a track is fit into a vertex, ξ and η become non-zero to the extent that the track is displaced parallel to itself in order to pass through the vertex.

We will later find it convenient to define one other vector which is not a unit vector, namely

$$\vec{\epsilon} \equiv \frac{\hat{\eta} - \hat{t}(\hat{\eta} \cdot \hat{t})}{1 - (\hat{\eta} \cdot \hat{t})^2}.$$

The vector $\vec{\epsilon}$ has a simple geometrical significance. If a track goes through a point $\vec{r}_0$ and one wants to displace it until it passes through a different point $\vec{r}_V$, the displacement along $\hat{\eta}$ is given by

$$\Delta\eta = (\vec{r}_V - \vec{r}_0) \cdot \vec{\epsilon}.$$

Therefore, if we wish to find a common vertex for N tracks, we need for each track, measurements of its 5 parameters which we define as $\alpha_1^{(k)}, \alpha_2^{(k)}, \alpha_3^{(k)}, \alpha_4^{(k)}$, and $\alpha_5^{(k)}$ for k = 1,2,...,N. The vertex reconstruction procedure then finds the most likely x, y, z vertex position which is common to all N tracks and the corresponding $\phi^{(k)}, \kappa^{(k)}$, and $\tan\lambda^{(k)}$ values at the vertex position for each of the N tracks. The single track fitting algorithm described in section 2.11 calculates the $\alpha_{j=1,5}^{(k=1,N)}$ values for each track along with their errors. The squares of the

errors on each $\alpha_j^{(k)}$ are then assembled into an error matrix by the tracking routine. We make use of the inverse of these error matrices which we call $\mathbf{H}^{(k)}$. If we define the new values of the orbit parameters to be $\mathcal{A}_j$, for tracks going through the vertex point, then we can form a χ^2 from the new and old values as

$$\chi^2 = \sum_{k=1}^{N} \sum_{i,j=1}^{5} (\mathcal{A}_i^{(k)} - \alpha_i^{(k)}) H_{ij}^{(k)} (\mathcal{A}_j^{(k)} - \alpha_j^{(k)})$$

The vertex reconstruction routine seeks optimal values of orbit parameters evaluated at the vertex position, referred to here as $\beta_1^{(k)} = \phi_V^{(k)}, \beta_2^{(k)} = \left(\frac{1}{pcos\lambda}\right)_V^{(k)}, \beta_3^{(k)} = \tan\lambda_V^{(k)}$, and $x_{1-3} = x, y, z$ of the vertex. Therefore, we need to solve equations given by

$$\frac{\partial \chi^2}{\partial \beta_{l=1,3}^{(\nu=1,N)}} = \sum_{k=1}^{N} \sum_{i,j=1}^{5} \left\{ \frac{\partial \mathcal{A}_i^{(k)}}{\partial \beta_l^{(\nu)}} H_{ij}^{(k)} \left[\mathcal{A}_j^{(k)} - \alpha_j^{(k)} \right] + \left(\mathcal{A}_i^{(k)} - \alpha_i^{(k)} \right) H_{ij}^{(k)} \frac{\partial \mathcal{A}_j^{(k)}}{\partial \beta_l^{(\nu)}} \right\} = 0$$

and similarly for $\frac{\partial \chi^2}{\partial x_{l=1,3}}$. The detailed solution to the above equations is given in the appendix. For the moment, we simply say that the procedure starts with the single-track fit information and an initial guess of the vertex position x_{V0}, y_{V0}, z_{V0}. It is assumed that the track parameters and track error matrices are determined near the vertex point. We then calculate the displacement of each track from its starting point, $x_0^{(k)}, y_0^{(k)}, z_0^{(k)}$, to x_{V0}, y_{V0}, z_{V0} along the axes $\hat{\xi}$ and $\hat{\eta}$ as defined above. The first estimates of the $\mathcal{A}_l^{(k)}$ parameters are therefore

$$\begin{aligned}
\mathcal{A}_{10}^{(k)} &= \phi^{(k)} = \alpha_1^{(k)} \\
\mathcal{A}_{20}^{(k)} &= \left(\frac{1}{pcos\lambda}\right)^{(k)} = \alpha_2^{(k)} \\
\mathcal{A}_{30}^{(k)} &= \tan\lambda^{(k)} = \alpha_3^{(k)} \\
\mathcal{A}_{40}^{(k)} &= (\vec{r}_V - \vec{r}_0)^{(k)} \cdot \hat{\xi}^{(k)} = \xi_V^{(k)} \\
\mathcal{A}_{50}^{(k)} &= (\vec{r}_V - \vec{r}_0)^{(k)} \cdot \hat{\epsilon}^{(k)} = \eta_V^{(k)}
\end{aligned}$$

where $\vec{r}_0^{(k)}$ is the vector from the origin to the track's point of closest approach to the origin. The solution of the χ^2 minimization equations yields a set of corrections $\delta\beta_{l=1,3}^{(k)}$ to the $\phi_V^{(k)}, \kappa_V^{(k)}$, and $\tan\lambda_V^{(k)}$ values of each track k and a new estimate of the vertex position (x_V, y_V, z_V). These values are then used to calculate a new set of orbit parameters $A_{l=1,5}^{(k)}$ and the entire process is repeated until the $\delta\beta$ corrections are very small. The final values of $x_V, y_V,$ and z_V and the error matrix for the vertex fit are used in the lifetime algorithm as described in chapter 4.

4. Method for Measuring Lifetimes

The basic procedure for estimating the lifetime of charmed meson decays is as follows: first, we must isolate a clean sample of D^0 or D^+ mesons. Then, using the information from their decay tracks, we estimate the position of the decay vertex. This position plus the known beam position allows us to estimate the decay length and decay length error for each D^0 or D^+ . Information from the decay tracks also allows us to calculate the D^0 or D^+ momentum and, from that, the proper decay time of the meson. The algorithm used was designed with three assumptions in mind.

1. The production point was close to the beam interaction point.

2. The direction of the D is known perfectly.

3. The errors in the estimated vertex and beam position are Gaussian in nature.

Assumption 1 is based on the physics of the reactions we will study. We assume simply that the D^0 and D^+ mesons in this analysis are produced in the vicinity of the beam spot. Assumption 2 is an approximation based on the fact that the error on the estimated decay distance due to errors on the D direction determination is small in comparison to the error due to the vertexing procedure. The small angular error on the charged track direction makes this obvious. Assumption 3 can be verified directly as shown in the previous chapter. We now show, in detail, how the information derived from the algorithms in chapter 3 are used in the lifetime calculation.

4.1 Lifetime Calculation

Since the resolution in the x-y plane was more than an order of magnitude better than the resolution along the beam direction (remember that the VC delivered only x-y information), only the x-y projection of the D decay lengths were measured. The full 3-dimensional length was then calculated using the measured angle between the beam line and the D flight direction. The most probable projected decay length for a given vertex is derived by considering the problem depicted in fig. 18 which has the beam interaction point as its origin. σ^B_{xx} and σ^B_{yy} are simply the x and y beam spreads squared. The error ellipse and beam spread are represented mathematically by the error matrices

$$\sigma_V = \begin{pmatrix} \sigma_{Vxx} & \sigma_{Vxy} \\ \sigma_{Vyx} & \sigma_{Vyy} \end{pmatrix} \text{ and } \sigma_B = \begin{pmatrix} \sigma_{Bxx} & \sigma_{Bxy} \\ \sigma_{Byx} & \sigma_{Byy} \end{pmatrix}.$$

It is assumed that the beam widths in x and y are independent of each other so that $\sigma_{Bxy} = \sigma_{Byx} = 0$. The beam spreads were determined by the studies described in chapter 3. The values for the vertex error matrix are derived from the vertex reconstruction algorithm as described in the previous chapter.

To find the most probable estimate for the projected decay length, ℓ', we follow a method found by Craig Blocker and note that the probability of measuring the vertex position x_V, y_V given the error matrices σ_V and σ_B can be defined as

$$\begin{aligned} P = \frac{1}{(2\pi)^2\sigma_V^2\sigma_B^2}\exp\Big\{ & -\frac{1}{2\sigma_B^4}[\sigma_{Byy}x_p^2 + \sigma_{Bxx}y_p^2 - 2\sigma_{Bxy}x_py_p] - \\ & \frac{1}{2\sigma_V^4}[\sigma_{Vyy}(x_0 - x_V)^2 + \sigma_{Vxx}(y_0 - y_V)^2 \\ & - 2\sigma_{Vxy}(x_0 - x_V)(y_0 - y_V)]\Big\} \end{aligned}$$

where x_p, y_p is the actual production point of the D, $\sigma_V^2 = \sigma_{Vxx}\sigma_{Vyy} - \sigma_{Vxy}^2$ (and similarly for σ_B^2), and $\hat{t}$ is the unit vector in the direction of the D momentum.

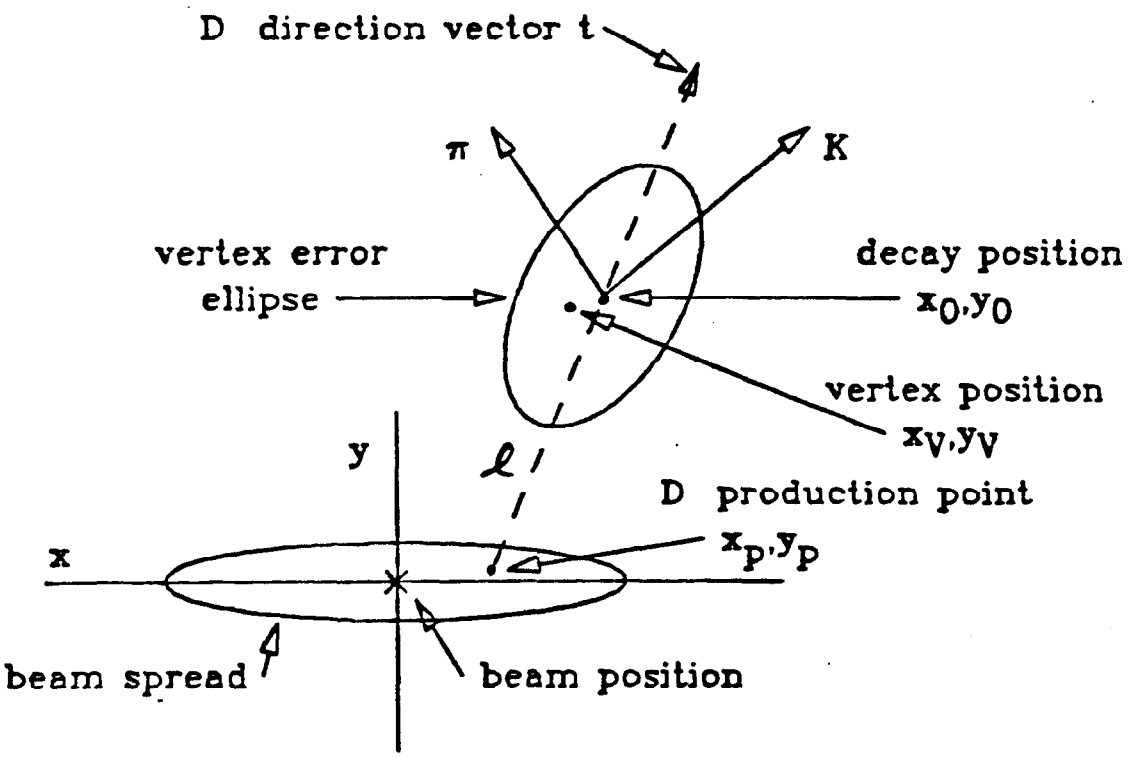

Fig. 18: Calculation of most probable decay length for an event

We now refer to fig. 18 to see that $x_0 = x_p + \ell' t_x$ and $y_0 = y_p + \ell' t_y$ where t_x, t_y are the 2-dimensional direction cosines of $\hat{t}$. We use these relations to express our probability function, P, as

$$P = \frac{1}{(2\pi)^2 \sigma_V^2 \sigma_B^2} \exp\Big\{ -\frac{1}{2\sigma_B^4}\Big[\sigma_{Byy} x_p^2 + \sigma_{Bxx}^2 y_p^2 - 2\sigma_{Bxy} x_p y_p\Big] - \frac{1}{2\sigma_V^4}\Big[\sigma_{Vyy}(\ell t_x + x_p - x_V)^2 + \sigma_{Vxx}(\ell t_y + y_p - y_V)^2 - 2\sigma_{Vxy}(\ell t_x + x_p - x_V)(\ell t_y + y_p - y_V)\Big]\Big\}.$$

The most probable value for ℓ' is the one for which $\frac{\partial P}{\partial \ell'} = 0$. Since x_p, y_p and ℓ' are all unknown, we need the simultaneous solution of the 3 equations

$$\frac{\partial P}{\partial x_p} = \frac{\partial P}{\partial y_p} = \frac{\partial P}{\partial \ell'} = 0.$$

After much algebra, the solution for ℓ' is found to be

$$\ell' = \frac{x_V B_{Txx} t_x + y_V B_{Tyy} t_y + B_{Txy}(x_V t_y + y_V t_x)}{B_{Txx} t_x^2 + B_{Tyy} t_y^2 - 2B_{Txy} t_x t_y}$$

where the matrix B_T is the inverse of the sum of the error matrices σ_B and σ_V. The error on ℓ' is given by

$$\sigma_{\ell'} = \left(\frac{\partial^2 P}{\partial \ell'^2}\right)^{-\frac{1}{2}} = \left[B_{Txx} t_x^2 + B_{Tyy} t_y^2 + 2B_{Txy} t_x t_y\right]^{-\frac{1}{2}}.$$

The full decay length is $\ell = \ell' / sin\theta_D$ where θ_D is the polar angle of the D flight path.

This method also allows us to find an expression for the most likely production point, x_p, y_p. With the solution for ℓ in hand, we find that

$$x_p = \frac{\sigma_B^4[(\sigma_B^4 \sigma_{Vxy}^2 - \sigma_{Vyy}(\sigma_V^4 \sigma_{Bxx} + \sigma_{Vxx}\sigma_B^4))(\ell t_x - x_V)}{(\sigma_V^4 \sigma_{Byy} + \sigma_B^4 \sigma_{Vyy})(\sigma_V^4 \sigma_{Bxx} + \sigma_{Vxx}\sigma_B^4) - (\sigma_B^4 \sigma_{Vxy})^2} - \frac{(\sigma_{Vxy}\sigma_{Vxx}\sigma_B^4 - \sigma_{Vxy}(\sigma_V^4 \sigma_{Bxx} + \sigma_{Vxx}\sigma_B^4))(\ell t_y - y_V)]}{(\sigma_V^4 \sigma_{Byy} + \sigma_B^4 \sigma_{Vyy})(\sigma_V^4 \sigma_{Bxx} + \sigma_{Vxx}\sigma_B^4) - (\sigma_B^4 \sigma_{Vxy})^2}$$

$$y_p = \frac{\sigma_B^4 \sigma_{Vxy}(\ell t_x - x_V) + \sigma_B^4 \sigma_{Vxy} x_p - \sigma_B^4 \sigma_{Vxx}(\ell t_y - y_V)}{\sigma_V^4 \sigma_{Bxx} + \sigma_{Vxx}\sigma_B^4}$$

with errors

$$\sigma_x = [\frac{\sigma_{Byy}}{\sigma_B^4} - \frac{\sigma_{Vyy}}{\sigma_V^4}]^{-1} \qquad \sigma_y = [\frac{\sigma_{Bxx}}{\sigma_B^4} - \frac{\sigma_{Vxx}}{\sigma_V^4}]^{-1}.$$

Values of ℓ and σ_ℓ were determined for each event. These decay lengths were converted to proper decay times via the formula

$$\tau = \ell/\gamma\beta c.$$

The mean lifetime and its error was derived from the sample of decay times.

4.2 Fitting Function

A maximum likelihood technique was used to extract the best estimate of the mean lifetime, τ_D, from the proper decay time sample. The logarithm of the likelihood function has the form

$$\ln \mathcal{L} = \sum_{i=1}^{N} \ln\Big[(1 - B_H - B_B)F_i(t) + B_H H_i(t) + B_B G_i(t)\Big]$$

where B_H and B_B are the background fractions of light-quark hadrons and D mesons from B hadron decays, respectively, which made it into the D lifetime sample. N is the number of events in the sample, and

$F_i(t) =$ Lifetime distribution of D's convoluted with a Gaussian resolution function

$H_i(t) =$ Lifetime distribution of light-quark hadronic background

$G_i(t) =$ Lifetime distribution for B$\rightarrow$ D background convoluted with a Gaussian resolution function

$F_i(t)$ was defined for each event by convoluting an exponential decay distribution for the lifetime with a Gaussian resolution function whose width is equal to the calculated error on the measurement. Thus, for each measurement

$$F_i(t) = \int_0^\infty \underbrace{\left[\frac{e^{\frac{-(t-\epsilon)^2}{2\sigma_t^2}}}{\sqrt{2\pi}\sigma_t}\right]}_{\text{Gaussian resolution}} \underbrace{\left[\frac{e^{-(\epsilon/\tau_D)}}{\tau_D}\right]}_{\text{exp. decay}} d\epsilon \qquad \text{where} \begin{cases} \tau_D = \text{ mean lifetime of D} \\ \sigma_t = \text{ error on measurement of} \end{cases}$$

Therefore,

$$\begin{aligned} F_i(t) &= \frac{1}{\sqrt{2\pi}\sigma_t\tau_D}\int_0^\infty e^{-\frac{(t-\epsilon)^2}{2\sigma_t^2}} e^{-\frac{\epsilon}{\tau_D}} d\epsilon \\ &= \frac{1}{2\tau_D}\left[e^{\left[\frac{\sigma_t^2}{2\tau_D^2}-\frac{t}{\tau_D}\right]}\left(1 - \text{ erf }\left(\frac{\sigma_t}{\sqrt{2}\tau_D} - \frac{t}{\sqrt{2}\sigma_t}\right)\right)\right]. \end{aligned}$$

A Gaussian distribution with a small mean was assumed for the lifetime distribution of the light-quark background. The measured mean from a control sample (see fig. 39) with 0 lifetime was used as the offset from 0 lifetime. Hence,

$$H_i(t) = \frac{1}{\sqrt{2\pi}\sigma_t} e^{-\frac{(t-\tau_H)^2}{2\sigma_t^2}}$$

where τ_H is 0.4×10^{-13} sec. Finally, we express $G_i(t)$ as

$$G_i(t) = \int_0^\infty \left[\frac{e^{-\frac{(t-\epsilon)^2}{2\sigma_t^2}}}{\sqrt{2\pi}\sigma_t}\right]\Big[D(\epsilon)\Big] d\epsilon.$$

$D(\epsilon)$ is the lifetime distribution of D mesons from the decay chain B$\rightarrow$ D^0 or D^+. It has the form

$$\begin{aligned} D(\epsilon) &= \int_0^\epsilon \frac{e^{-\frac{\lambda}{\tau_B}}}{\tau_B}\frac{e^{-\frac{(\epsilon-\lambda)}{\tau_D}}}{\tau_D} d\lambda \qquad \text{where } \tau_B = \text{mean lifetime of B hadrons} \\ &= \frac{1}{\tau_B - \tau_D}\left[e^{-\frac{\epsilon}{\tau_B}} - e^{-\frac{\epsilon}{\tau_D}}\right]. \end{aligned}$$

This simplifies the expression for $G_i(t)$ to

$$G_i(t) = \frac{1}{\sqrt{2\pi}\sigma_t(\tau_B - \tau_D)} \int_0^\infty e^{\left[-\frac{(t-\epsilon)^2}{2\sigma_t^2}\right]} \left[e^{-\frac{\epsilon}{\tau_B}} - e^{-\frac{\epsilon}{\tau_D}}\right] d\epsilon$$

$$= \frac{1}{2(\tau_B - \tau_D)} \left\{ e^{\left(\frac{\sigma_t^2}{2\tau_B^2} - \frac{t}{\tau_B}\right)} \left[1 - \operatorname{erf}\left(\frac{\sigma_t}{\sqrt{2}\tau_B} - \frac{t}{\sqrt{2}\sigma_t}\right)\right] - e^{\left(\frac{\sigma_t^2}{2\tau_D^2} - \frac{t}{\tau_D}\right)} \left[1 - \operatorname{erf}\left(\frac{\sigma_t}{\sqrt{2}\tau_D} - \frac{t}{\sqrt{2}\sigma_t}\right)\right] \right\}.$$

5. Charmed Hadron Identification

In order to minimize the systematic errors on a lifetime measurement, we must find an event sample which is highly-enriched in the decays which we wish to study. Separating charm events from the light-quark hadronic background available at PEP energies is complicated by the fact that the charm quark, although it is much heavier than the u,d, or s quarks, is not sufficiently massive enough to allow efficient selection of a highly charm-enriched sample on the basis of strictly dynamical studies. For example, it is possible to select a charm-enriched sample by cutting on the total momentum and transverse momentum (relative to the jet axis) of leptons found in hadronic events[28] . The enrichment for charm, however, is only about 45% at best. This is not much larger than the $\simeq$ 30% enrichment in a general hadronic sample which comes about simply because, in the QED model of quark production, the $+\frac{2}{3}$ charge of the charm quark demands that it contribute $\frac{4}{11}$ of the total hadronic cross section at PEP energies. The mass resolution of the Mark II detector for reconstruction of D^0 and D^+ mesons was not sufficient to take advantage of such a small enrichment factor.

We can take advantage of one prime source of D^0 and D^+ mesons. For example, clean samples of D^0 and D^+ mesons can be obtained by observing the decay reactions

$$D^{*+} \rightarrow D^0\pi^+ \qquad\qquad D^{*+} \rightarrow D^+\pi^0$$
$$\hookrightarrow K^-\pi^+ \text{ or } K^-\pi^+\pi^0 \qquad\qquad \hookrightarrow K^-\pi^+\pi^+$$

where the D^{*+} is the excited state of the D^+ . Note from table 1 that the D^{*+} - D^0 and D^{*+} - D^+ mass difference is just a few MeV/c^2 greater than the π^+ or π^0 mass, respectively. This means that the relative decay angle and momenta, in the lab frame, of the D and the bachelor pion are very restricted.

These tight kinematical bounds make it easy to identify the decay reactions with very little background if the detector's momentum and angular resolution on the low momentum π^+ and π^0 are sufficiently high. Ref.[29] details the first observation of the D^{*+} meson at PEP energies. The methods for identifying the D^{*+} in the analysis presented here are quite similar to that of ref.[29]. Several important differences arise due to the necessities of lifetime measurements. These are explained below.

The basic philosophy for identifying a lifetime sample is as follows: a first stage of cuts is made to isolate a reasonably clean sample of events in which these decays have occurred. A second stage of cuts is then made to eliminate events in which it was likely that the D decay tracks have scattered or been mismeasured. Special care is taken at this stage to minimize any possible biases against long or short lifetimes. We begin the description of the event selection with a discussion of the $D^{*+} \rightarrow D^0\pi^+$ decay.

5.1 $D^0 \rightarrow K\pi$ Event Selection

The first stage of cuts chose D^{*+} candidates from a sample of 60,000 hadronic events gathered from 207 pb^{-1} of data. Hadronic events are defined as having 7 or more charged tracks, a total energy (charged + neutral) greater than 25% of the beam energy and an event vertex which is within 5 cm radius (in the x-y plane) of the beam interaction point and 10 cm of that point in the longitudinal direction, z. As noted in chapter 1, the estimated decay length for D^0 mesons is < 1 mm, so that this cut is not considered a possible lifetime bias. Finally, any event which has a photon with energy between 7 and 20 GeV is considered to be a gamma-gamma event (where one gamma had converted) and is therefore rejected.

Invariant mass values are calculated for all 2-track combinations in these events, assuming one track is a kaon and one is a pion. Information from the TOF system could provide kaon, pion identification for tracks with momenta less than 1.0 GeV/c, but, in order to maximize efficiency, no attempt at particle identification is made. Instead, all tracks are tried as both kaons and pions. The momenta of the tracks are corrected for dE/dx losses which the charged tracks suffered in going through the 1.5% of a radiation length of material between the interaction point and the main drift chamber. Fig. 19 shows the invariant mass distribution for all assumed $K\pi$ combinations. Since there is no obvious peak at the D^0 mass, all combinations with invariant mass between 1.72 and 2.00 GeV/c^2 are taken as D^0 candidates. This range of 28 MeV/c^2 was chosen on the basis of Monte Carlo studies to be fully efficient and sufficiently far above the S* resonance[30] . The kinematic fitting routine, SQUAW, is used to vary the parameters of these tracks in order to satisfy a constraint to the D^0 mass while minimizing a chisquare formed from the amount of the variations and the track error matrices. These tracks are then combined with other appropriately charged tracks (π^+ for a negative kaon, π^- for a positive kaon) in the event to form $K\pi\pi$ combinations. Fig. 20 shows the distribution of $\Delta M_{K\pi\pi-D^0}$, the difference between the invariant mass of the $K\pi\pi$ combinations and the D^0 mass. A clear peak exists for events in which z, the energy of the $K\pi\pi$ system divided by the beam energy is greater than 0.6. Events which have a $K\pi\pi$ combination with z> 0.6, mass difference < 200 MeV/c^2 , and χ^2 /dof less than 10 for the kinematic fit to the D^0 mass are retracked using the procedure described in section 2.11, then advanced to the second stage of cuts.

All the $K\pi\pi$ prongs are subjected to the second stage of cuts to ensure that the information provided by them is accurate. These quality cuts begin by

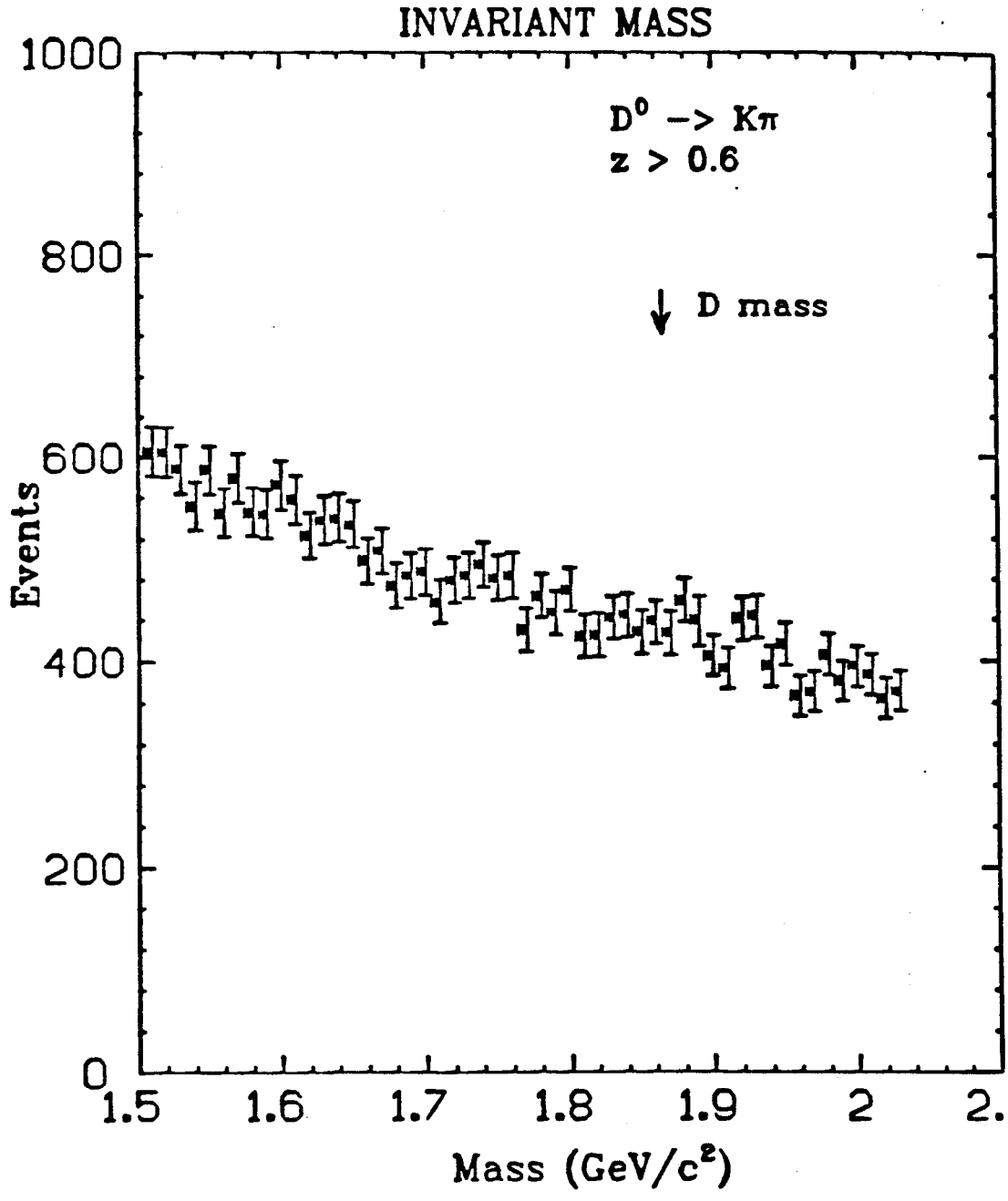

Fig. 19: Invariant mass distribution for all possible $K\pi$ combinations

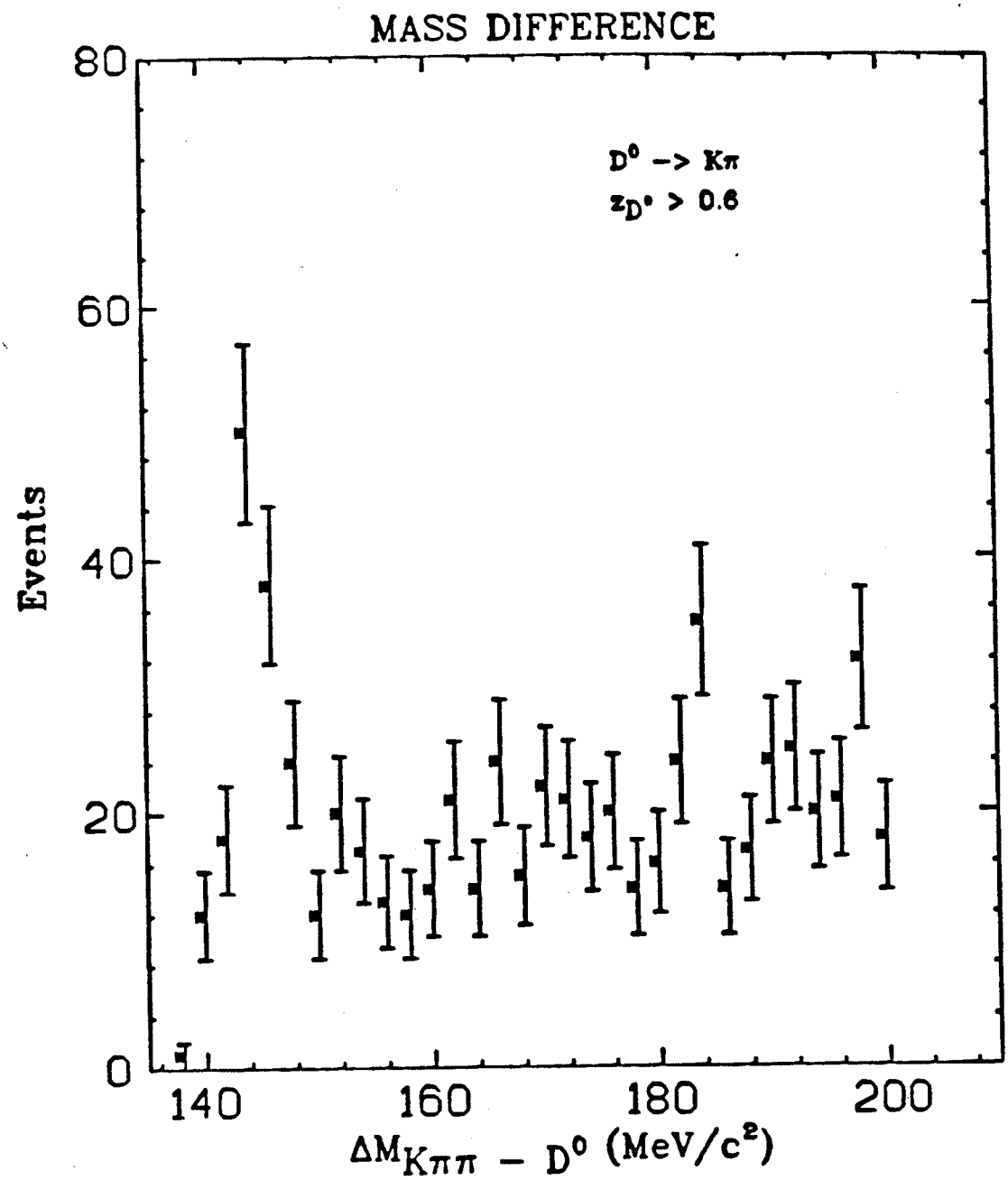

Fig. 20: Mass difference distribution for combinations assumed to be from the decay mode $D^{*+} \rightarrow D^0\pi$, $D^0 \rightarrow K\pi$

demanding that each of these tracks have

- 10 or more hits in the VC-DC tracking chambers
- the χ^2 per degree of freedom or "goodness of fit" of the track to the raw drift times of its hits must be less than 7
- all tracks except the bachelor pion must have a momentum greater than 0.5 GeV/c. The bachelor pion must have a momentum greater than 0.3 GeV/c
- each track must have 2 or more hits in the inner band of the VC and at least one hit in the outer band
- the χ^2 per degree of freedom of the track fit in the VC alone must be less than 5
- each D^{*+} decay track must be more than $\frac{1}{5}$ of a wire spacing from any other track at each layer of the VC in order to prevent misassignment of a drift time to the wrong track

In addition, any VC hit on the decay tracks which contributes more than 3/dof to the VC track fit χ^2 is eliminated. The track is then refit and passed through the above cuts again. A maximum of three VC hits are allowed to be removed in this way.

The K and π from the D^0 decay are fit to a common vertex using the algorithm described in section 3.5. All track errors from the VC are boosted by 10% before the vertex fit. To see why this must be done, we refer to fig. 21. Fig. 21a shows the χ^2 /dof for single track fits for tracks in a D^{*+} sample which have all 7 VC dazms. The solid curve shows the expected shape of this distribution, a χ^2 distribution for 5 degrees of freedom. The data is noticeably wider than the

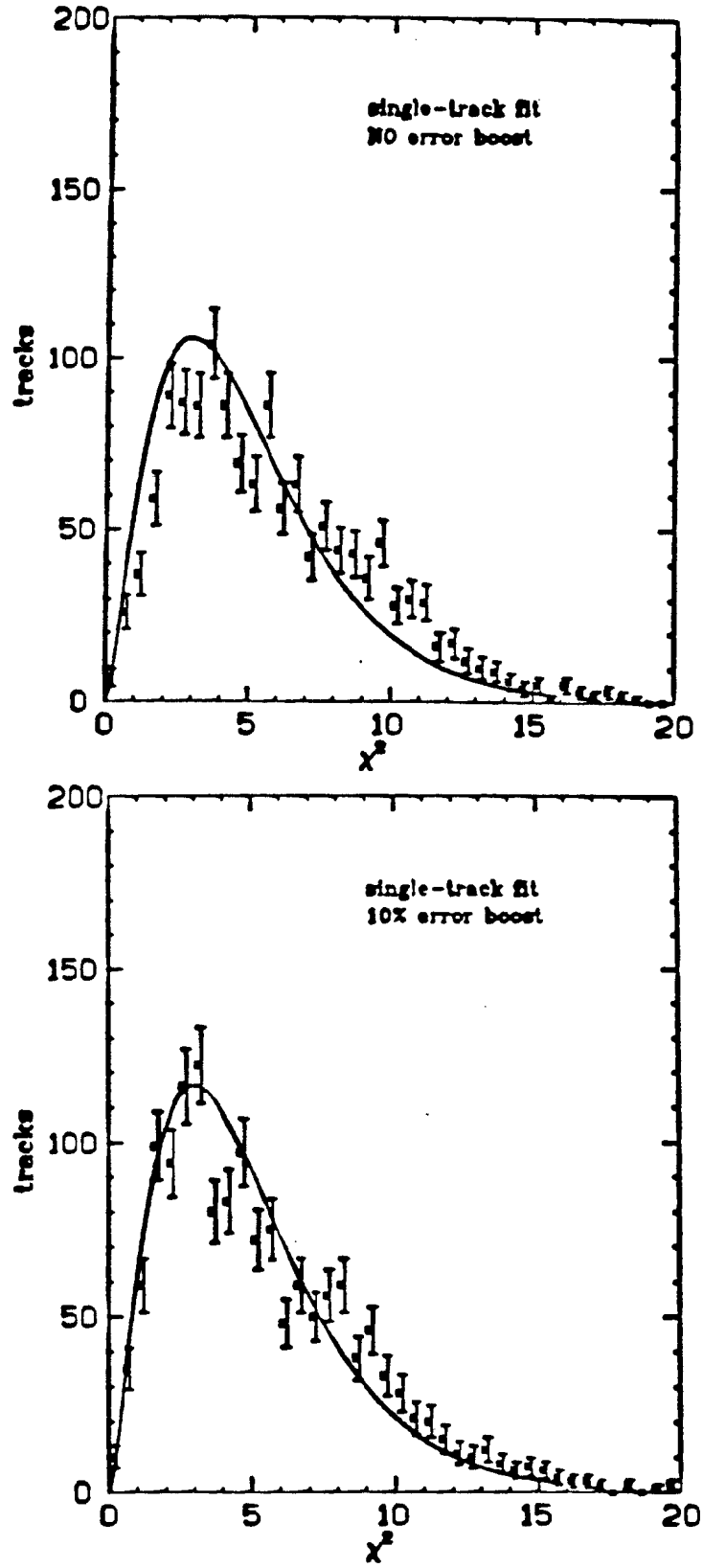

Fig. 21: a. χ^2 of single track fits in the vertex chamber.

b. χ^2 of single track fits after boosting the VC tracking errors by 10%.

All tracks are taken from the $D^0 \rightarrow K\pi$ data sample

theoretical curve. The most likely reason is due to the fact that the errors used in the VC tracking were derived from Bhabha-type events with low multiplicity and high momentum. The tracking environment in the middle of an hadronic jet was thus quite a bit different than that used in determining these errors. The higher track density in hadronic events presumably causes more confusion in the assignment of hits to the proper tracks, and, therefore, greater tracking errors. The requirement that tracks not overlap has little effect in correcting the problem. Fig. 21b shows the single track fit χ^2 after boosting the VC tracking errors by 10%. The agreement with the theoretical prediction is now much better.

Immediately after the vertex fit, the vertex errors are boosted by 8%. The reasons for this will be explained in chapter 6 which deals with systematic errors. The χ^2/dof of the 2-particle vertex is required to be less than 5. The distribution of vertex χ^2 is shown in fig. 22.

We also require that the D^0 flight trajectory be consistent with the hypothesis that it originated in the vicinity of the beam interaction spot. The D^0 flight trajectory is defined to be the line which is parallel to the D^0 momentum and which is used to determine the optimal decay length. It was demanded that the distance of closest approach of this trajectory to the beam interaction point be less than 3 standard deviations in the transverse error on the trajectory. The transverse error includes contributions from the 2-particle vertex position error and the beam spread. The transverse error contribution coming from the uncertainty in the D^0 momentum direction is quite small in comparison to the contribution from the vertex and beam errors.

We should now recall that the angle of the bachelor pion relative to the D^0 flight path is of crucial importance in determining the mass difference, $\Delta M_{K\pi\pi-D^0}$. It is possible to discriminate against events in which the low

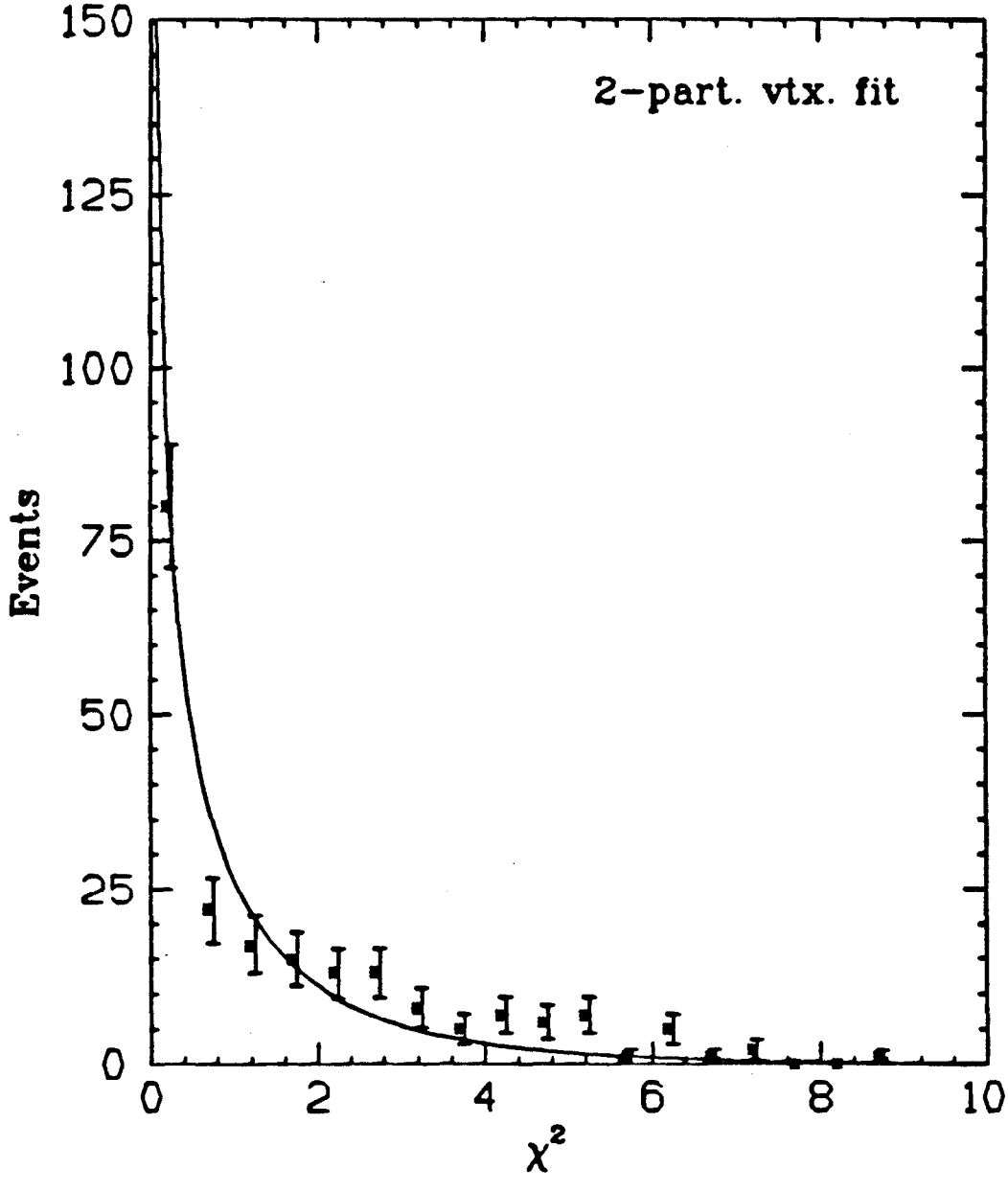

Fig. 22: Distribution of χ^2 for vertex fits of the K and π for the sample $D^0 \rightarrow K\pi$. The curve shows the expected shape for a χ^2 distribution with 1 degree of freedom

momentum bachelor pion has scattered or been mismeasured, by performing a vertex fit of this track and the virtual D^0 track using the D^0 production point as a constraint. The transverse errors on the D^0 trajectory and the bachelor pion are shown in fig. 23. We required the χ^2 of the vertex fit to be less than 5 per degree of freedom. This procedure not only cuts events in which the bachelor pion has been badly measured, but allows, in principle, a better determination of the relative angle between the D^0 and bachelor π than a single-track fit on the bachelor π alone. This, in turn, gives a better estimate of the $\Delta M_{K\pi\pi-D^0}$ and a consequent reduction in the combinatorial background under the peak at $\Delta M_{K\pi\pi-D^0} = .145$ GeV/c^2 in fig. 20. The distribution of vertex χ^2 is shown in fig. 24. We discuss in chapter 6 the expected effect this and other cuts might have on the detection of very long-lived D^0 's.

Two further checks are made to verify that the $K\pi$ candidates are consistent with coming from D^0 decays. The first cut is derived by looking at fig. 25 which shows the momentum distribution of bachelor pions from the process $D^{*+} \rightarrow D^0\pi$ for Monte Carlo-generated events. Noting the sharp cut-off of this distribution at 1.0 GeV/c, we ask that no D^{*+} candidate in the lifetime sample have a bachelor pion with momentum greater than 1.3 GeV/c. Secondly, we ask that the χ^2/dof of the kinematic fit of the K and π momenta to the D^0 mass be less than 5. The final kinematic fit is done using track information constrained by the D^0 - bachelor pion vertex fit described above. This ensures maximum precision on the $\Delta M_{K\pi\pi-D^0}$ determination. As a final assurance of the quality of the decay length information from the event, a cut is made on the rms spread of measured beam positions for the run from the BPM. Events are rejected if the run shows more than 250μ motion in x or 150μ motion in y. These limits are found by studying the width of the impact parameter distributions for Bhabhas vs. the BPM rms

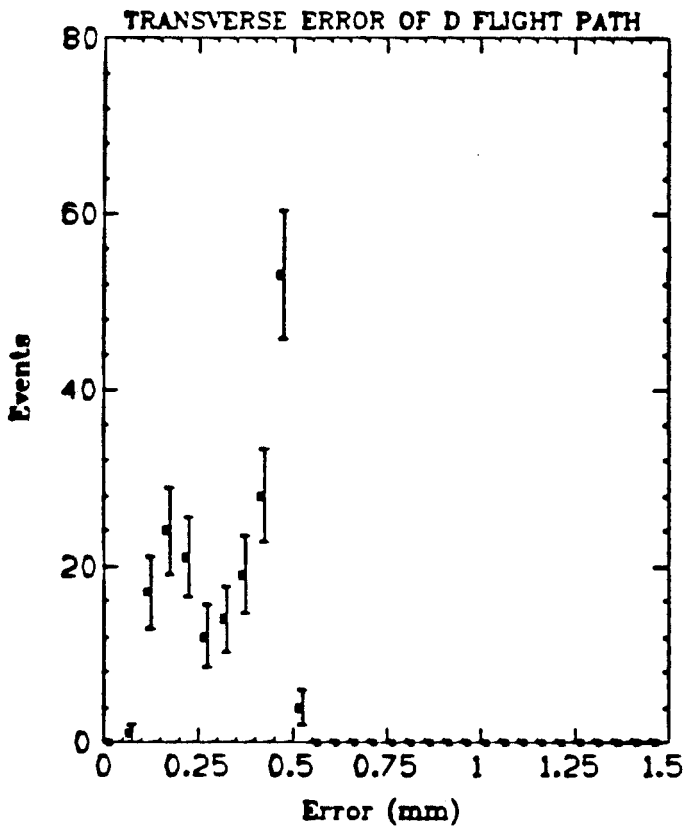

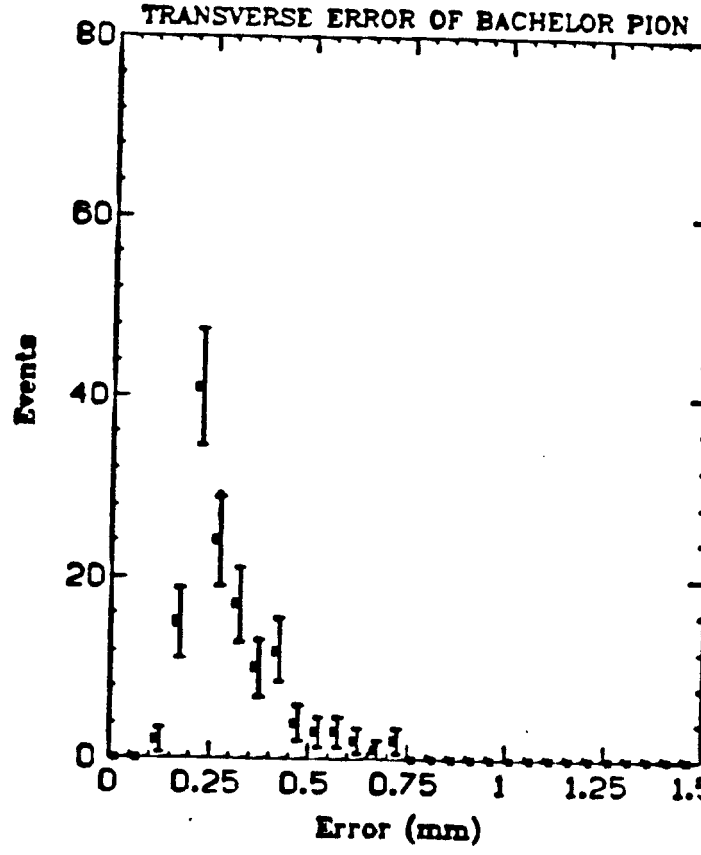

Fig. 23: a. Positional error on the virtual D^0 track in the direction transverse to the D^0 flight path. This error includes the beam spread

b. Positional error in the direction transverse to the bachelor pion track

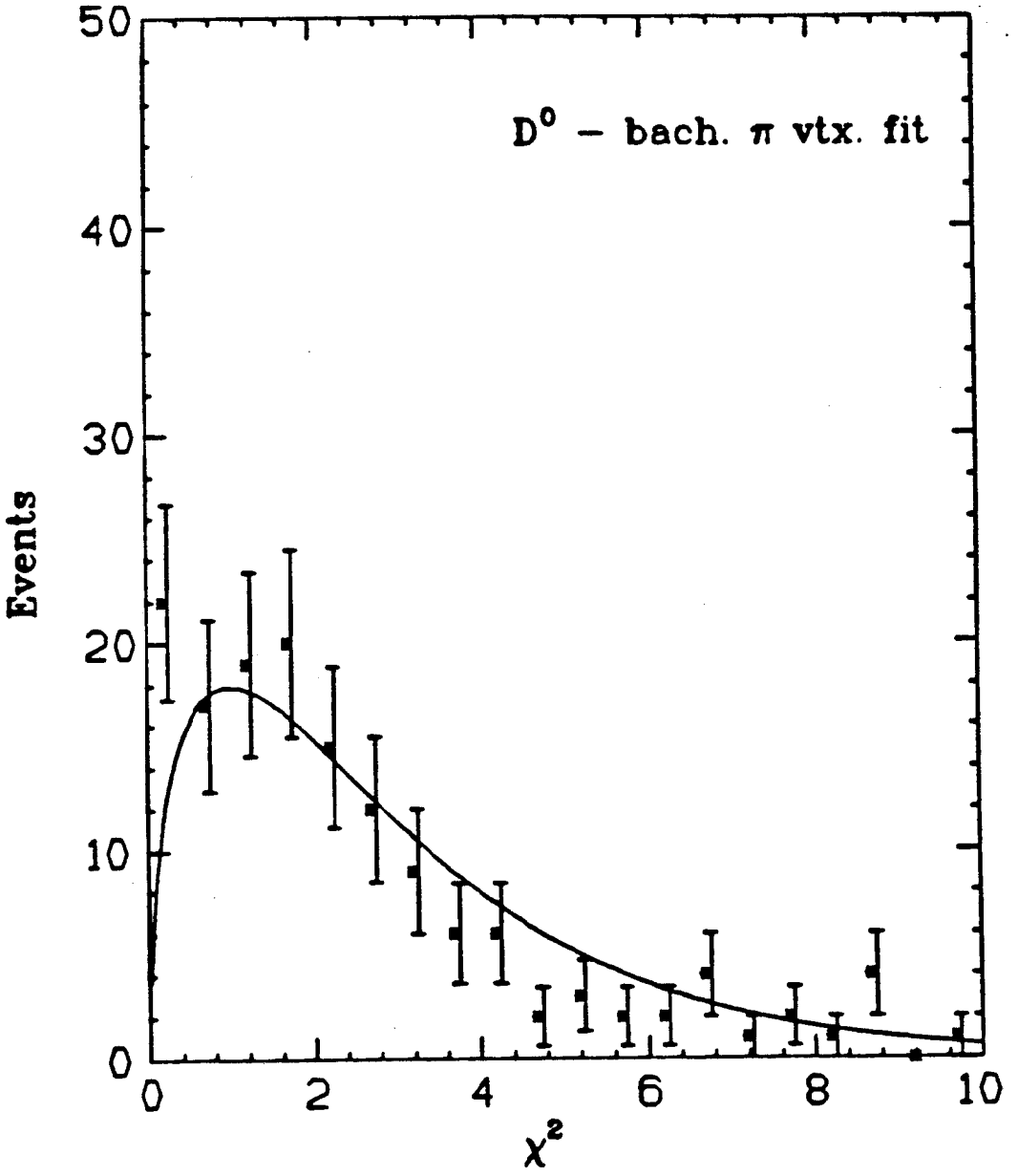

Fig. 24: χ^2 distribution for the vertex fit of the bachelor pion and the virtual D^0 track. The curve shows the expected shape for a χ^2 distribution with 3 degrees of freedom

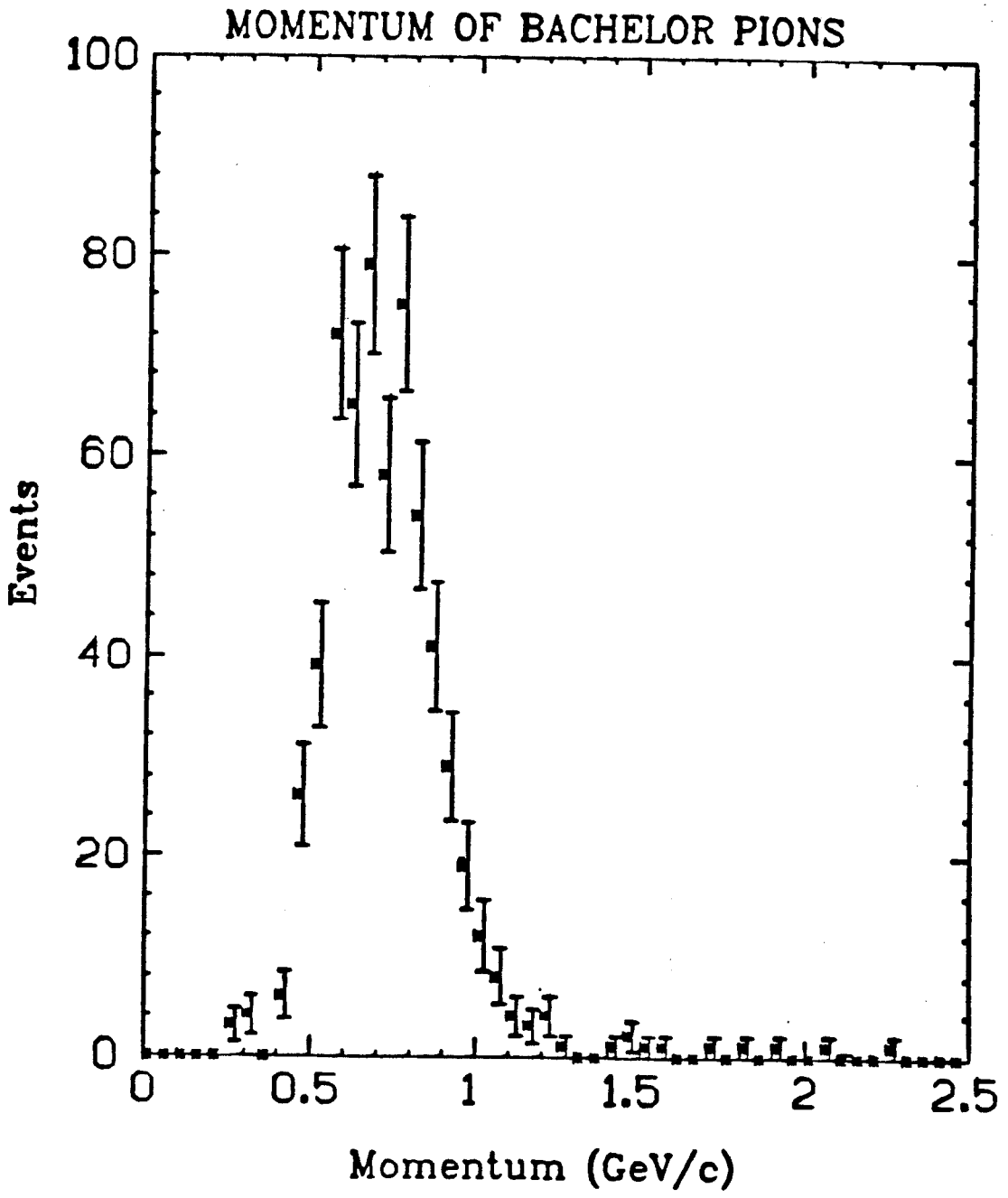

Fig. 25: Measured momenta of bachelor pions found in Monte Carlo produced D^{*+} events.

spread in x and y for the run. As an example, consider fig. 26 which shows the impact parameter/estimated error distribution of Bhabha tracks within 100 mr of the x or y-axis for several values of the rms spread in BPM y and x measurements within the run. The increase in width of this distribution as the rms spread increases indicates a loss in resolution for runs which had significant amounts of beam steering.

Using the track momenta from the D^0 - bachelor pion vertex fit, the mass difference for all surviving events is recalculated. Fig. 27 now shows a markedly improved $\Delta M_{K\pi\pi-D^0}$ distribution. D^{*+} events are defined to be the 39 events with a mass difference between 0.143 and 0.150 GeV/c^2 and z> 0.6. From this figure, the combinatorial background under the peak is estimated by assuming a linear fit to the shape of the plot for $\Delta M_{K\pi\pi-D^0}$ greater than 0.150 GeV/c^2 . The estimated background is 4.6 ± 2.1 events. Backgrounds from B decays are estimated from a Monte Carlo study of the efficiency of these cuts for the sequence $B \rightarrow D^{*+} \rightarrow D^0\pi$. The relevant parameters assumed in the Monte Carlo, e.g. B fragmentation function, B branching fraction to D^{*+} , momentum distribution of D^{*+} decays from B's, etc. are taken from published results of the MAC, Mark II , and CLEO collaborations[31–34] . On the basis of the Monte Carlo study, our best estimate of the contamination of the final sample due to B decays is between 3 and 5%. As described in section 4.2, combinatoric and B backgrounds are taken into account in determining the mean D^0 lifetime.

The decay length for each D^0 is determined by the method described in chapter 4. The decay length distribution is shown in fig. 28. These lengths are converted into proper decay times using the measured D^0 momenta. It should be noted that only the 2-particle vertex is used in determining the decay length of the D^0 candidates. Fig. 29 shows the distribution of proper decay times for

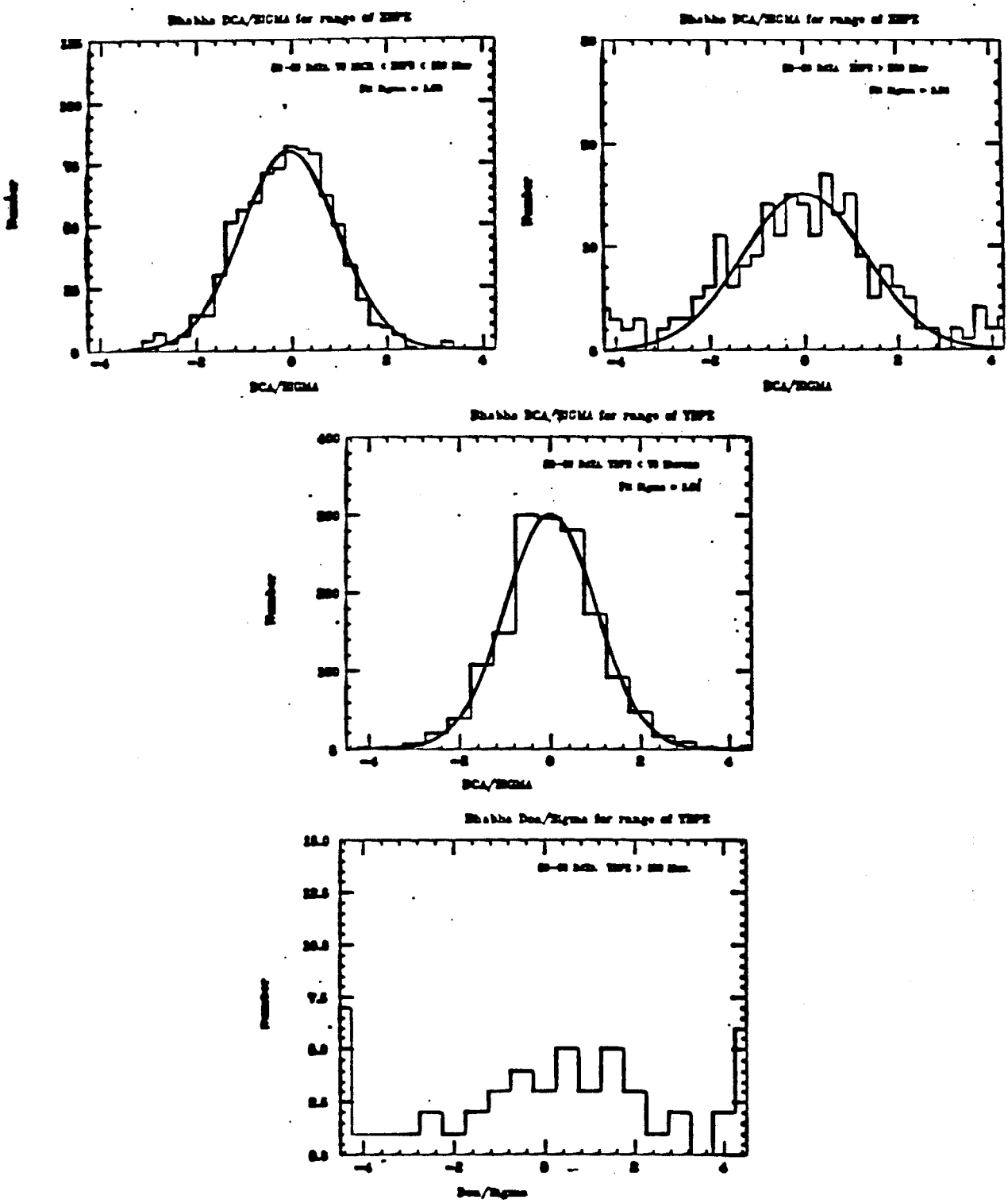

Fig. 26: Distribution of impact parameter/estimated error of vertical and horizontal Bhabha tracks for various values of the rms spread in BPM beam position measurements

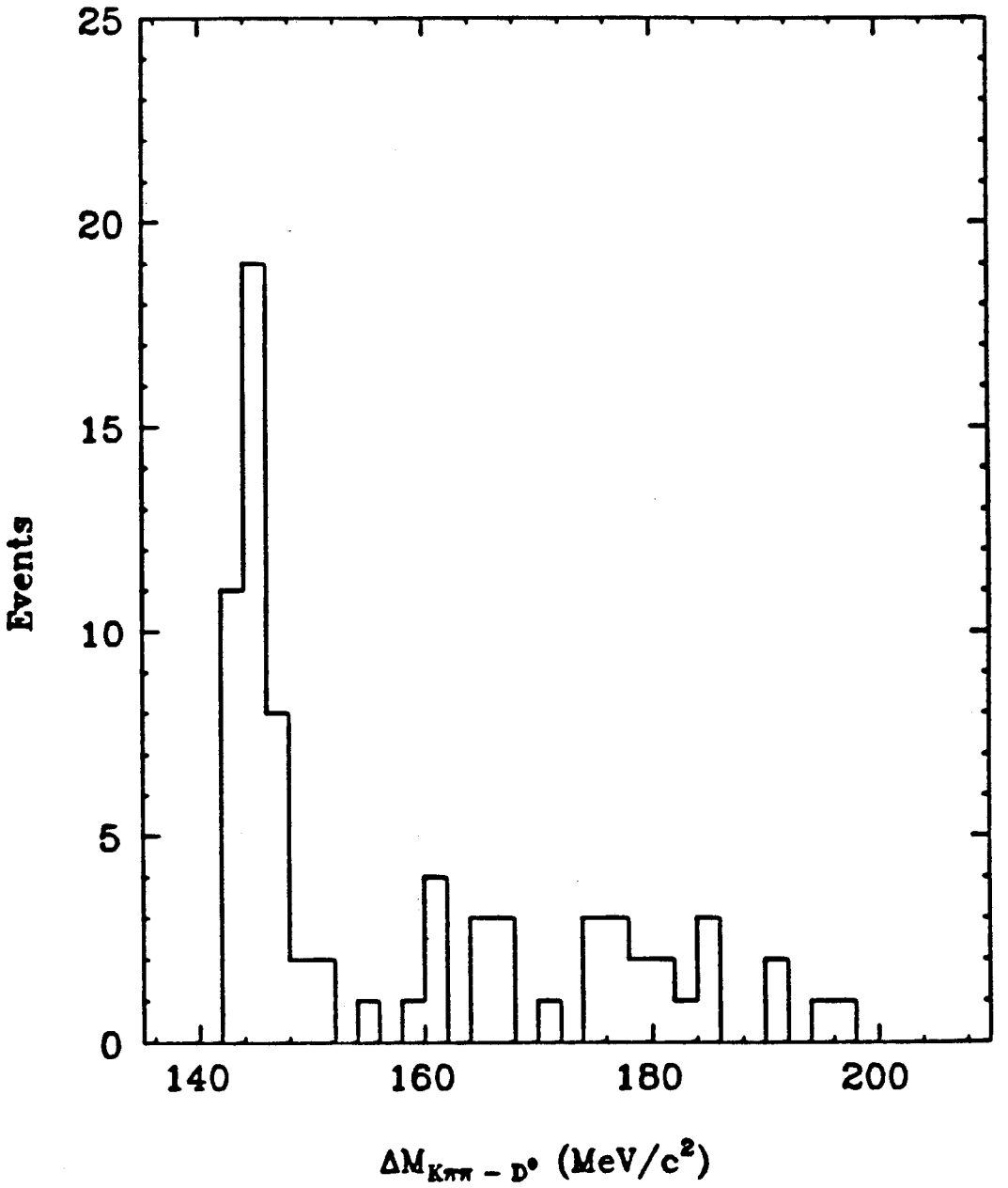

Fig. 27: Mass-difference plot for $D^0 \rightarrow K\pi$ events after the D^0 - bachelor pion vertex χ^2 cut

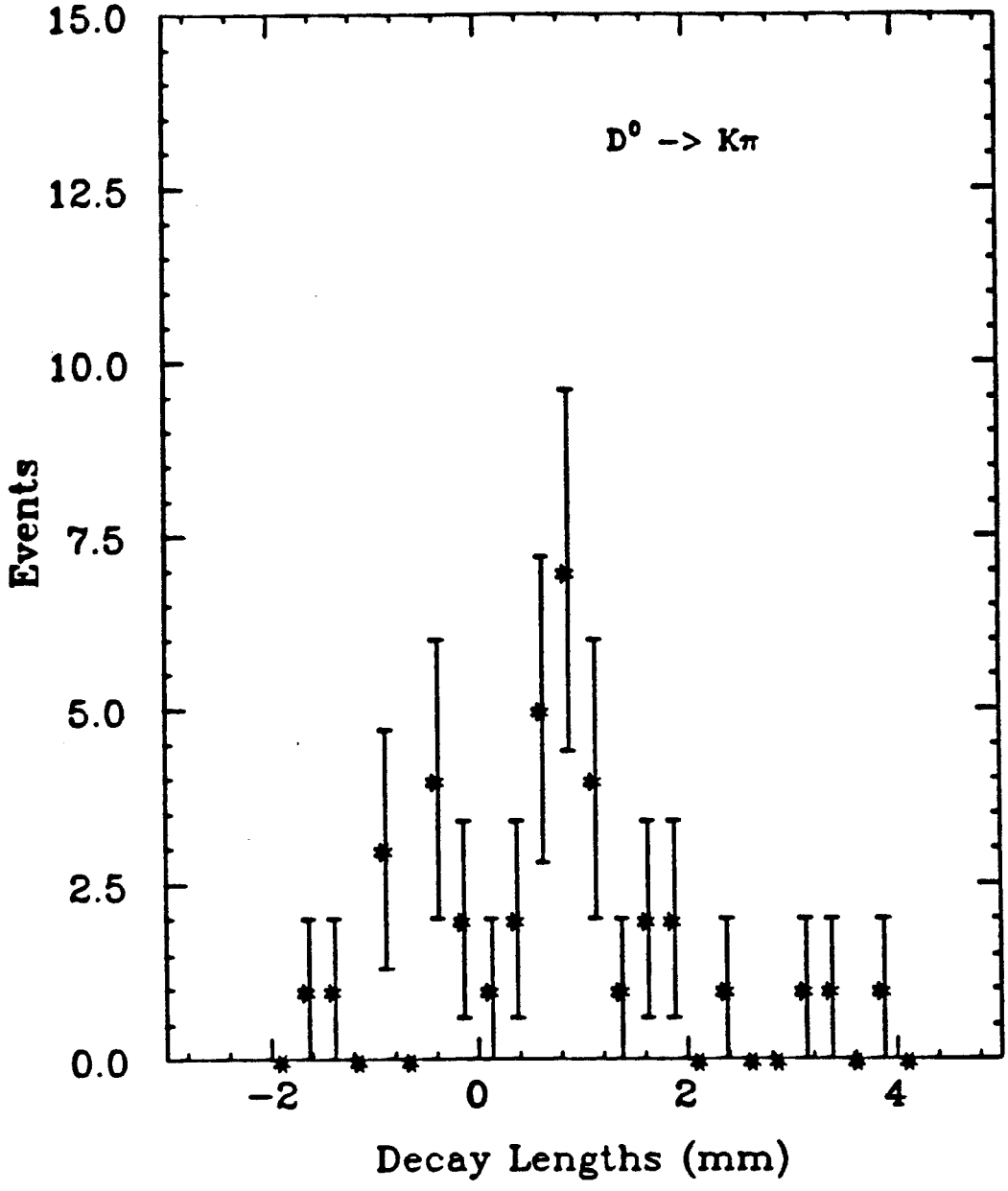

Fig. 28: Distribution of decay lengths for $D^0 \to K\pi$ events

the D^{*+} events. Fig. 30 shows the distribution of lifetime errors.

The maximum likelihood method described in section 4.1 was used to extract the mean lifetime of this sample. The result was $4.7^{+1.3}_{-1.0} \times 10^{-13}$ s, where the errors are purely statistical. The curve shown in fig. 29 shows the expected shape of the distribution of proper decay times. The curve is normalized to the total number of events in the sample and represents the shape of the fitting function discussed in section 4.2.

5.2 $D^0 \rightarrow K\pi\pi^0$ Event Selection

We can extend the data sample of D^0 mesons using methods very similar to those described above simply by searching for other decay modes of the D^0 . One possibility which proved successful, is the decay sequence

$$\begin{aligned} D^{*+} &\rightarrow D^0\pi^+ \\ &\quad\big\lfloor\!\rightarrow K^-\pi^+\pi^0. \end{aligned}$$

where we again take advantage of the low Q value of the D^{*+} decay to significantly enhance the signal to background ratio. The procedure for identifying this sample is basically identical to that for $D^0 \rightarrow K^-\pi^+$ except for the requirement of a π^0 . Again, we do not attempt any particle identification of charged tracks using the TOF system, but instead took all combinations of tracks in an hadronic event assuming all tracks to be both kaons and pions. π^0 candidates are formed from photons in the LA system which are more than 2° away from the azimuthal edge of a module and less than 1.7 m in $|z|$[35] . Photons which have energy between 0.1 GeV and 4.0 GeV (as measured by the LA calorimeter) are paired. Those pairs with an invariant mass less than 20 MeV/c^2 or greater than 700 MeV/c^2 are rejected. The momenta of the remaining pairs is constrained to the π^0 mass. Any photon which has 4.0GeV $<$ E_γ $<$ 7GeV and which passes the fiducial

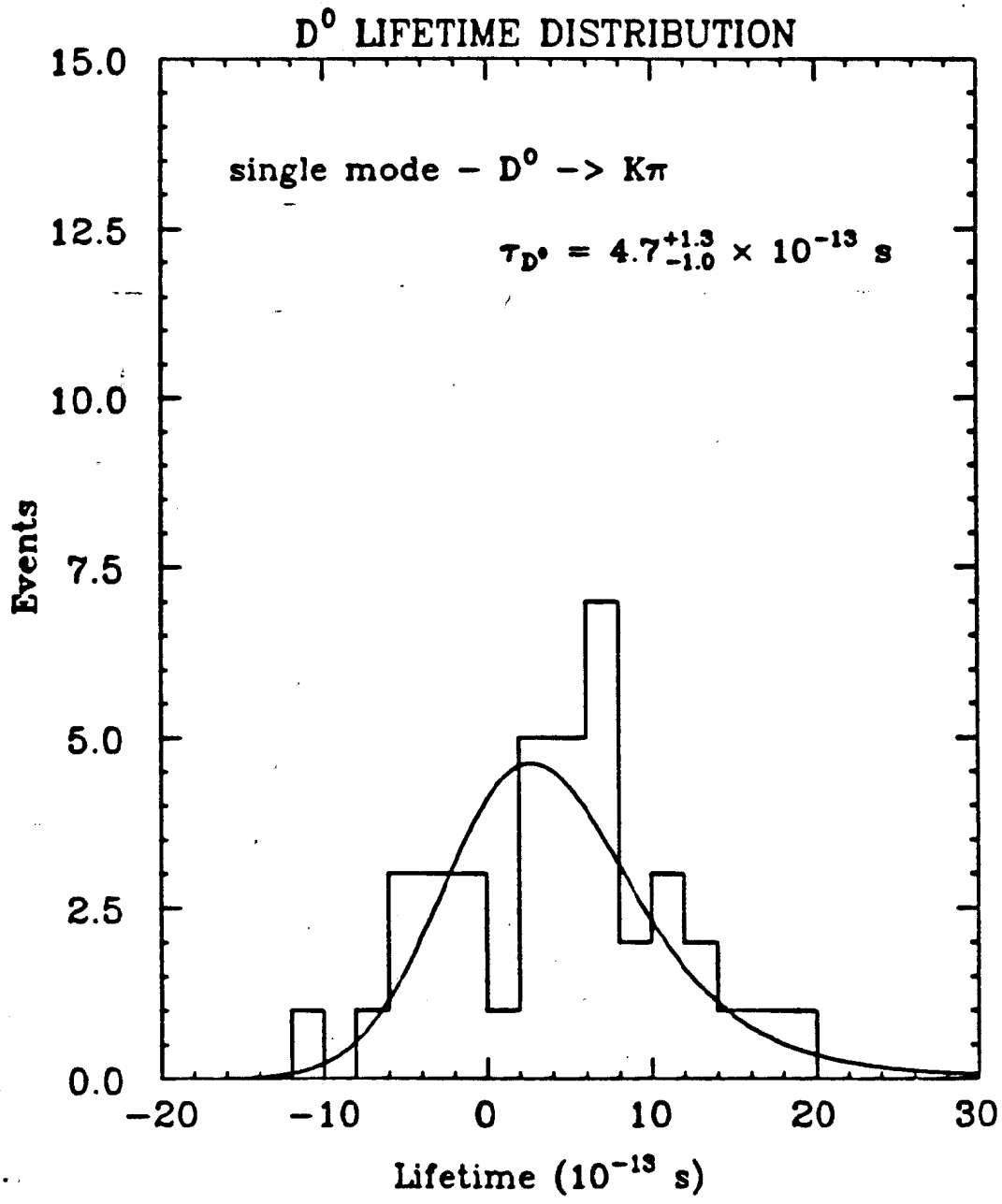

Fig. 29: Lifetime distribution for $D^0 \to K\pi$ events along with the curve showing the expected distribution for the measured lifetime

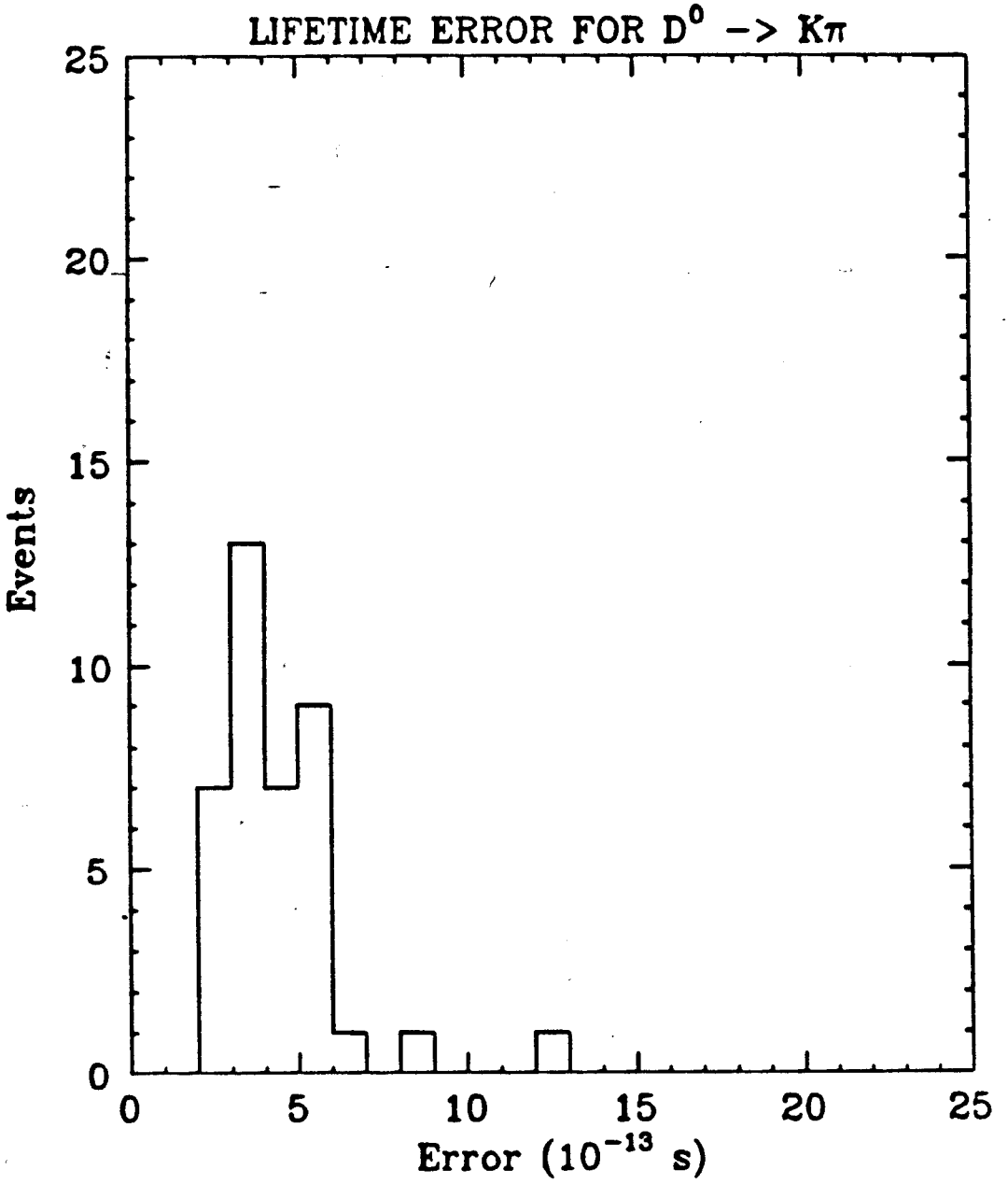

Fig. 30: Distribution of lifetime errors for the $D^0 \to K\pi$ sample

requirements is considered to be a π^0 with merged decay products. π^0 candidates are rejected if they have momentum less than 400 MeV/c. As expected, there is again no obvious peak in the invariant mass distribution. All combinations between 1.76 and 1.96 GeV/c^2 are taken to be D^0 candidates. The momenta of the tracks is kinematically fit to the D^0 mass. D^0 candidates where the χ^2 /dof of the kinematic fit is less than 10 are combined with other appropriately charged tracks in the event to form $K\pi\pi^0\pi$ combinations.

Fig. 31 shows the distribution of $\Delta M_{K\pi\pi^0\pi-D^0}$, the difference between the invariant mass of the $K\pi\pi^0\pi$ combinations and the D^0 mass for z > 0.6. Events with z greater than 0.6 and mass difference less than 200 MeV/c^2 are retracked, then put through the same second stage cuts as described above for the $K\pi$ mode. Fig. 32 shows the invariant mass of the π^0 candidates used for these events.

The second stage cuts described in the previous section apply only to charged tracks. For the π^0 candidates, we merely tightened constraints on the quality of the fit to the π^0 mass. The first requirement is that the invariant mass of the gamma pairs which form π^0 candidates be less than 400 MeV/c^2. Secondly, we demand that the χ^2/dof for the quality of the fit to the π^0 mass be less than 3.

Fig. 33 shows the final plot of $\Delta M_{K\pi\pi^0\pi-D^0}$ after all cuts for events with $z_{D^{*+}} > 0.6$. D^{*+} events are defined to be the 35 events with a mass difference between 0.143 and 0.150 GeV/c^2 and $z_{D^{*+}} > 0.6$. From this figure, the combinatorial background under the peak is estimated by assuming a linear fit to the shape of the plot for $\Delta M_{K\pi\pi^0\pi-D^0}$ greater than 0.150 GeV/c^2 (two bins below the D^{*+} peak were included in the fit in order to add some constraint corresponding to the absence of phase space due to the kinematic limit at 139.6 MeV/c^2). The estimated background is 5.0 events. The amount of background

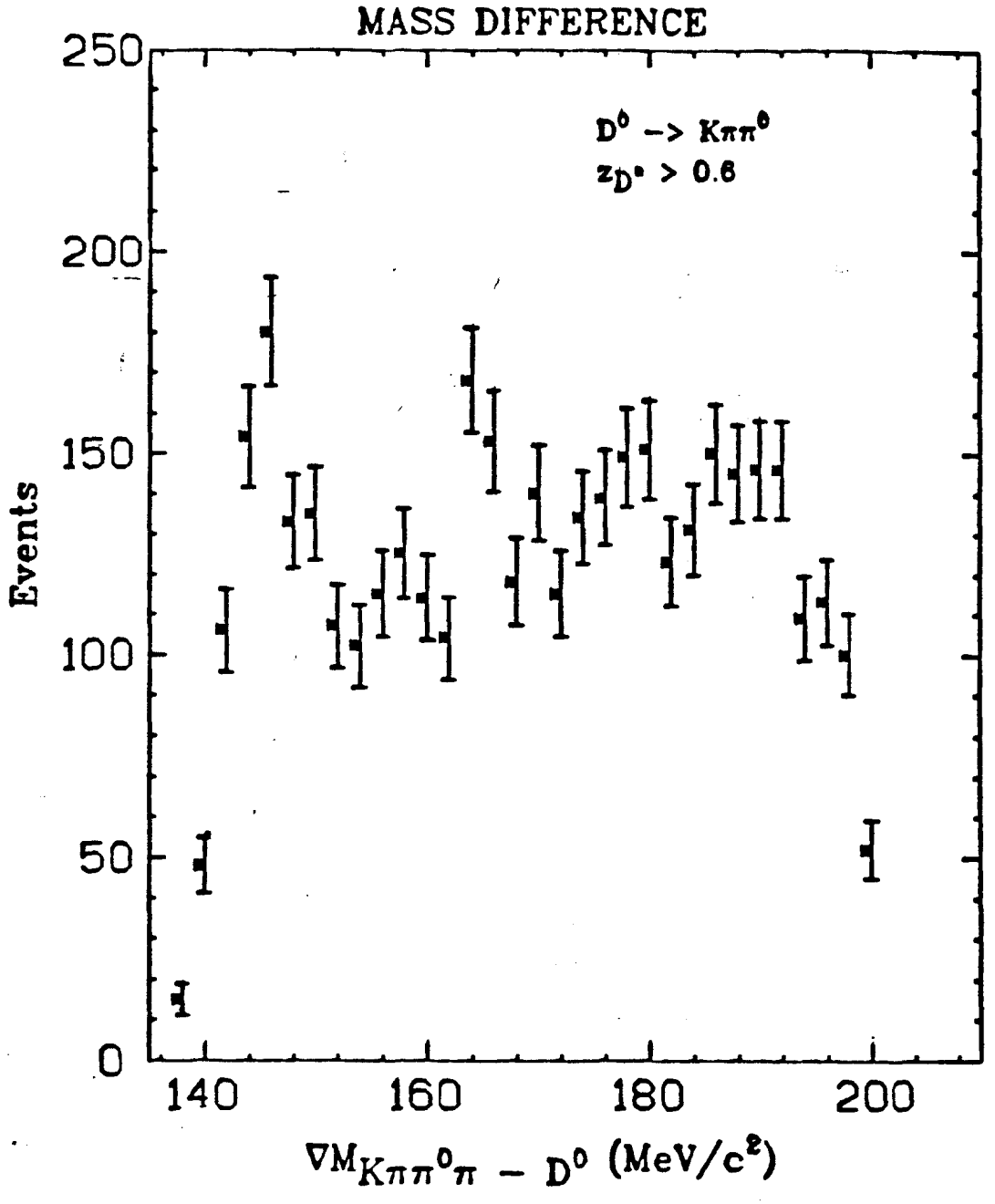

Fig. 31: Distribution of $\Delta M_{K\pi\pi^0\pi-D^0}$ for z greater than 0.6

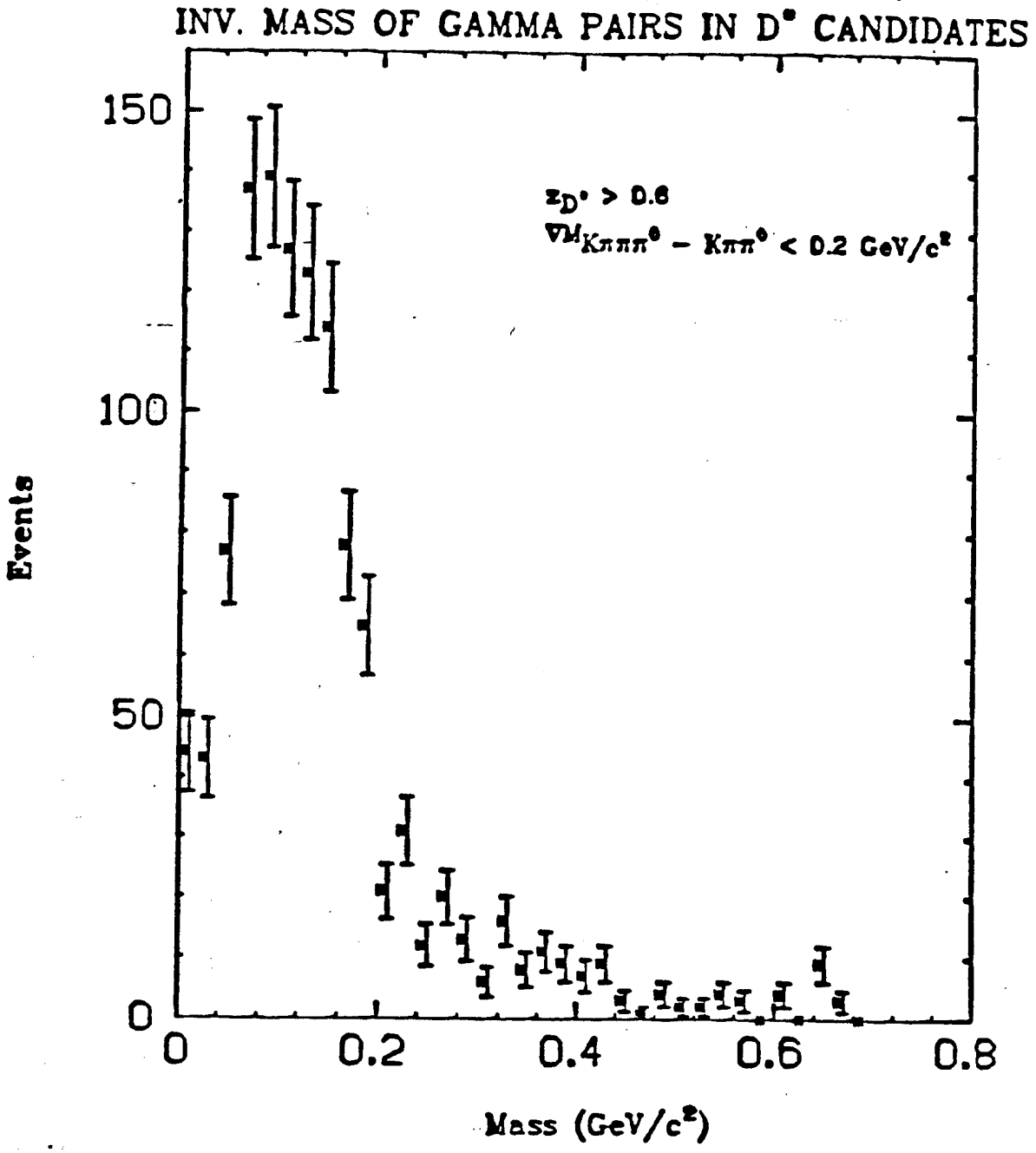

Fig. 32: Invariant mass of π^0 candidates found in events with small mass difference and large z.

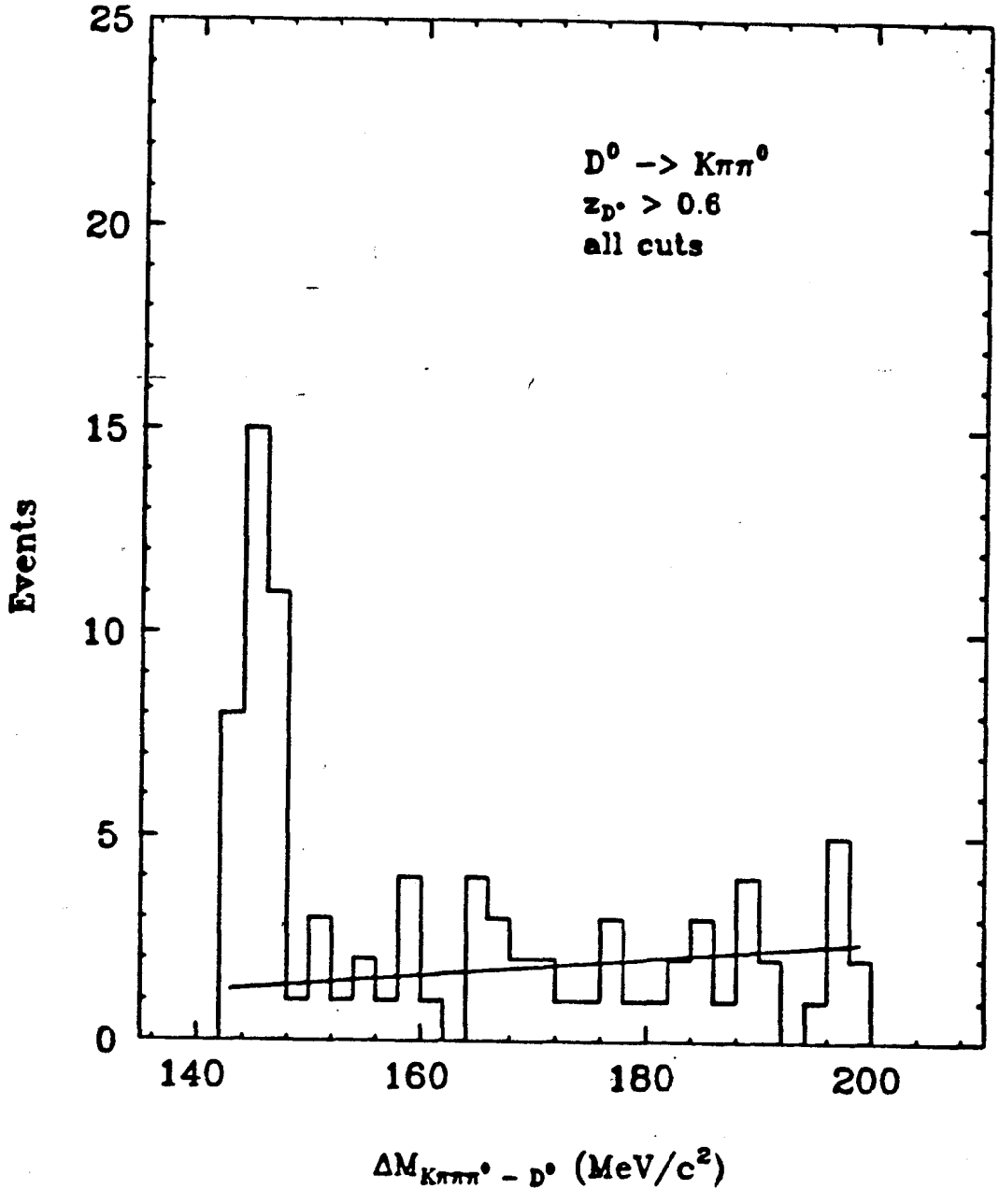

Fig. 33: Distribution of mass difference for the decay mode $D^0 \rightarrow K\pi\pi^0$. The solid curve shows the result of a linear fit to the combinatorial background outside the signal region

from B decays is assumed to be 3% as in the $D^0 \to K\pi$ case.

Figs. 34 and 35 show the proper decay time and lifetime error distribution of this sample. The mean determined with the maximum likelihood method is $4.8^{+1.5}_{-1.2} \times 10^{-13}$ s.

5.3 Other Decay Modes of the D^0

Several other decay modes of the D^0 could, in principle, be detected by the Mark II . However, the cleanliness of the signals from these other modes would not be likely to match that of the two already presented. The combinatoric background for decay modes with higher charged multiplicities goes up rapidly. As an example, we consider fig. 36 which shows the mass difference distribution for 5-particle combinations made under the assumption that they are from the decay mode

$$\begin{array}{l} D^{*+} \to D^0\pi^+ \\ \qquad\quad \big\lfloor\!\!\to K^-\pi^+\pi^+\pi^-. \end{array}$$

Only a small signal can be seen. Other distinct decay modes have branching fractions which are either too small to be seen or involve particles (such as η's or K^*'s) which have a low efficiency of detection in the Mark II . In principle, we could also search for D^0 mesons via the decay sequence

$$\begin{array}{l} D^{*0} \to D^0\pi^0 \\ \qquad\quad \big\lfloor\!\!\to K^-\pi^+\pi^0 \text{ or } K^-\pi^+. \end{array}$$

We can again take advantage of the low Q value of this reaction to enhance the mass resolution on the D^* peak, however we must now contend with a low momentum π^0 . As will be shown in the section dealing with the D^+ lifetime, the low momentum bachelor π^0 presents special problems which ensure that the resolution on the mass difference peak for such a decay will be considerably lower

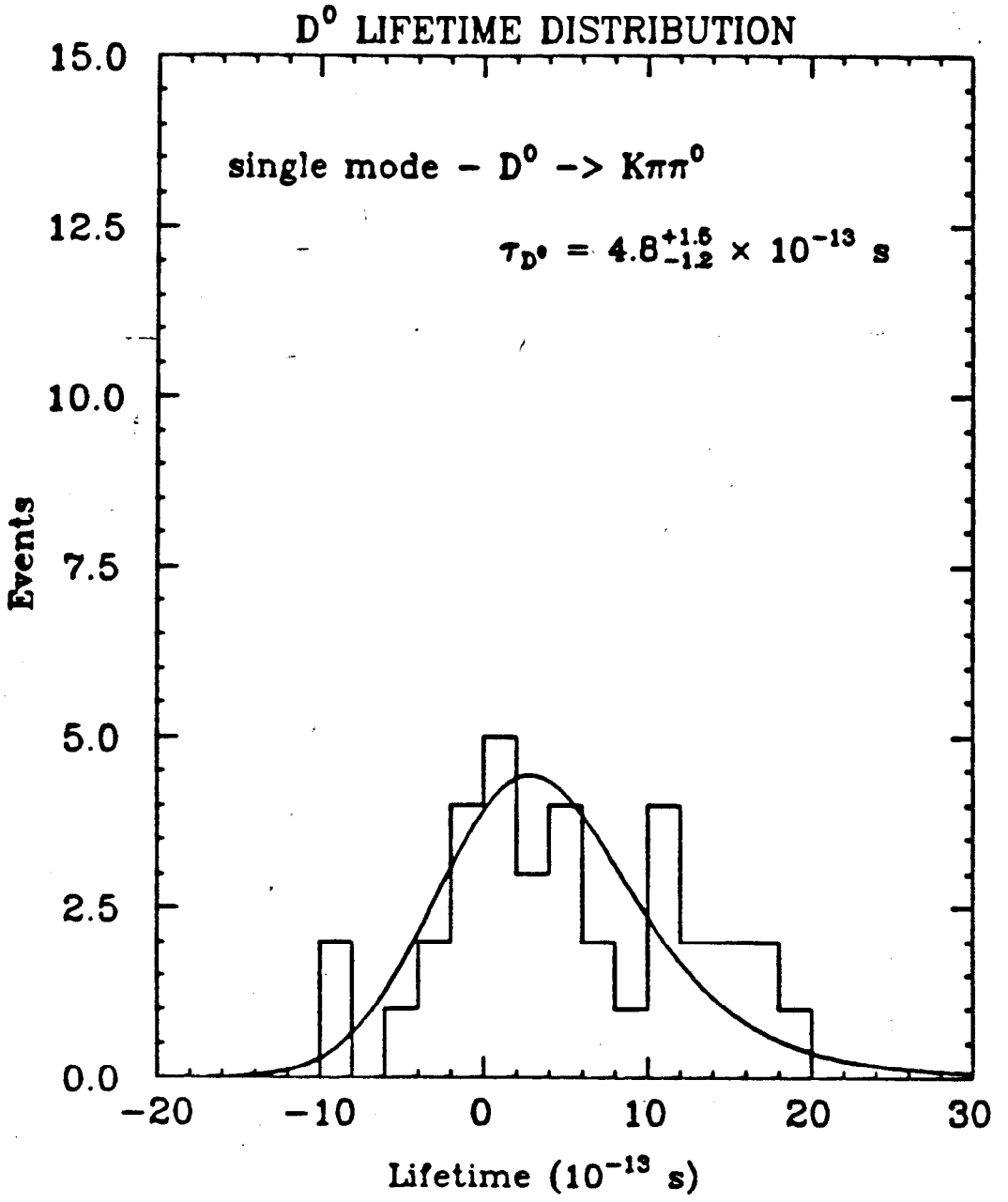

Fig. 34: Distribution of proper decay times for the decay mode $D^0 \to K\pi\pi^0$

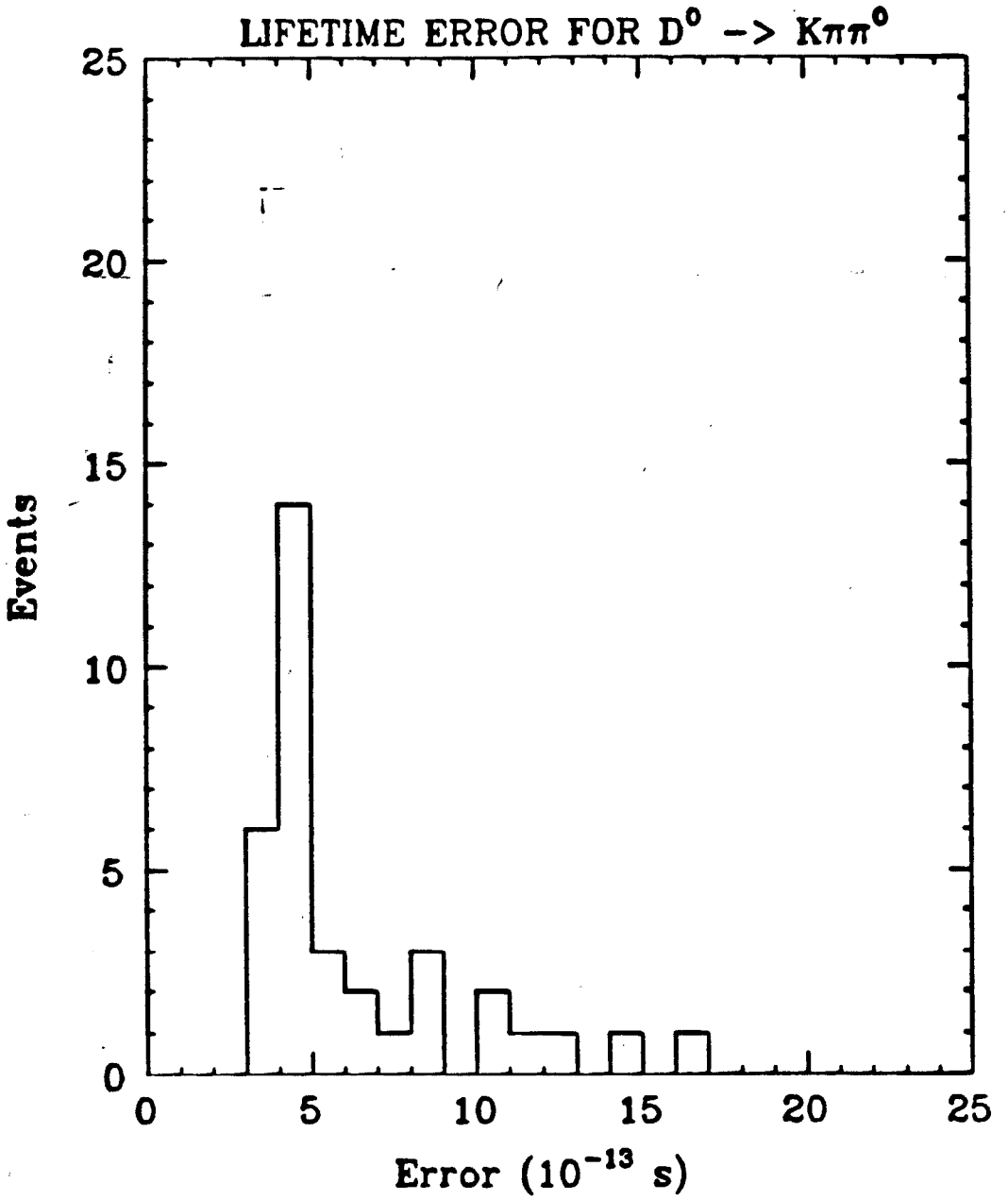

Fig. 35: Distribution of decay time errors for the decay mode $D^0 \to K\pi\pi^0$

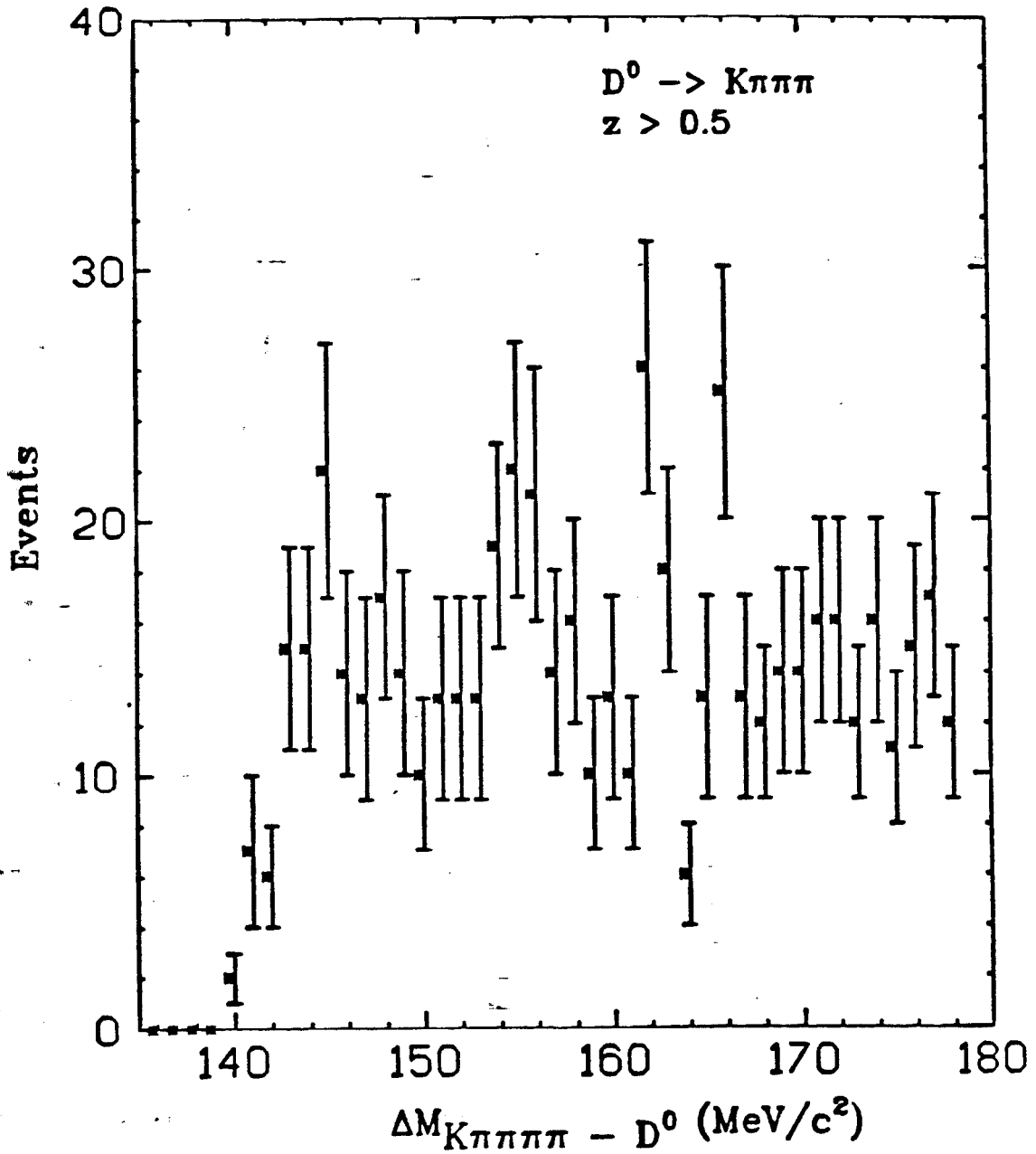

Fig. 36: Mass difference distribution for combinations assumed to be from the decay sequence $D^{*+} \to D^0\pi$, $D^0 \to K\pi\pi\pi$

than for the modes with charged bachelor pions. Thus, if we want a clean sample of D^0 mesons, we must be content with the 74 events in hand.

5.4 D^0 Lifetime

The background levels and average event error for the two samples discussed above are comparable and the cuts used to obtain them are very nearly identical. Thus, it is not expected that there will be any systematic errors which are not common to both samples. We have therefore added the two samples to get fig. 37. The curve superimposed on the data shows the shape of the fitting function for the measured mean lifetime of $4.7^{+0.9}_{-0.8} \times 10^{-13}$ s.

5.5 D^0 Control Sample

In order to test the correctness of the vertexing procedure and fitting function, a control sample of hadron tracks was developed. The control sample is formed by making fake D^{*+} decays out of hadronic tracks with approximately the same kinematics as true D^{*+} decays. Separate control samples are used for the D^0 and D^+ systematic checks. The D^0 control sample will be discussed here.

In order to make fake D^{*+} decays with approximately the same kinematics as true D^{*+} decays, we made the following requirements: first, the stage 1 event quality cuts described in the previous section are applied to the hadronic event sample. For the events which pass these cuts, $K\pi$ pairs are formed. Again, no attempt at particle identification is made, instead all tracks are tried as both kaons and pions. In each event, all $K\pi$ pairs with invariant masses between 2.05 and 2.42 GeV/c^2 are considered as D^0 control candidates. The K and π were not required to have opposite charge. Each candidate is combined with all other appropriately charged tracks in the event and those combinations with

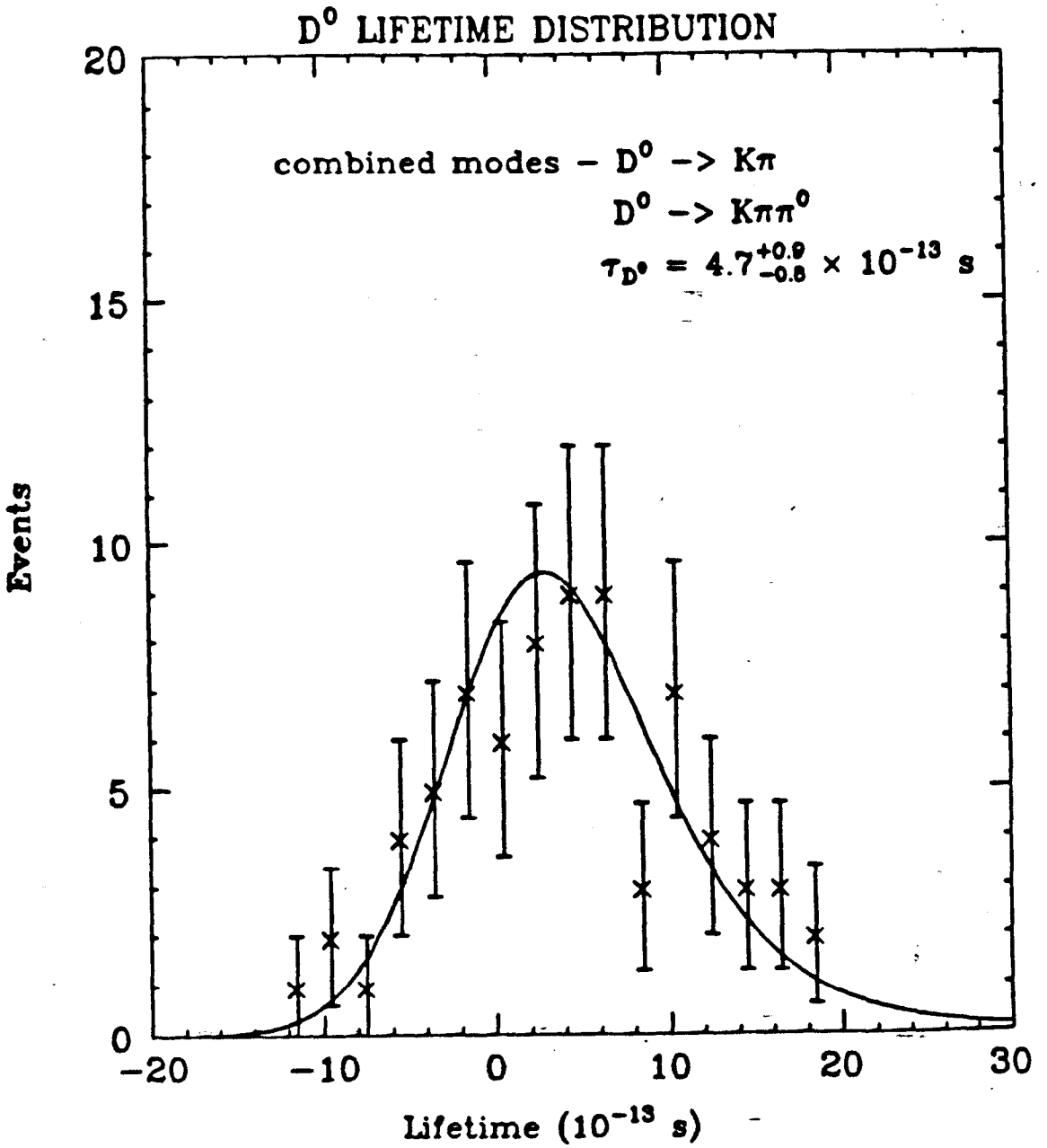

Fig. 37: Lifetime distribution of the combined sample, $D^0 \to K\pi$ and $D^0 \to K\pi\pi^0$. The curve shows the expected shape of the distribution corresponding to the measured lifetime of the combined sample

an invariant mass difference, $M_{3particle} - M_{2particle} < 300$ MeV/c^2 and z value above 0.6 are put into the D^{*+} control sample. All D^{*+} control tracks are then subjected to the same stage 2 cuts applied to the data. In order to eliminate vertices from K_s^0 and Λ decays, any track which, when combined with another track of opposite charge, gave a pair with an invariant mass within 20 MeV/c^2 of the K_s^0 mass or within 10 MeV/c^2 of the Λ mass is deleted from the pool of control sample candidates. Fig. 38 shows the final mass difference distribution for the D^0 control sample after all cuts.

Fig. 39 shows the proper decay times found for these vertices. The shape and mean of this distribution is markedly different from fig. 37 which shows the same distribution for the D^0 sample. The measured value of $0.6 \pm 0.3 \times 10^{-13}$ s is small, but decidedly positive. This is expected since some tracks from charm and bottom decays have to be in the control sample. We checked that the effect of such decays on the control sample was correct by forming a control sample from Monte Carlo events using the same procedure outlined above. The Monte Carlo control sample produced a mean lifetime of $0.5 \pm 0.3 \times 10^{-13}$ s. The average charm lifetime in the Monte Carlo, weighted by the amount of D^0 and D^+ mesons expected in PEP data (D^0 mesons are produced about 2.5 times as often as D^+ mesons), was 5.6×10^{-13} s. The average B lifetime was 10^{-12} s. The lifetime for a Monte Carlo control sample where the charm and bottom lifetimes were set to 0 yielded a mean lifetime consistent with 0.

5.6 $D^+ \to K\pi\pi$ Analysis

We now describe the method for determining the D^+ lifetime. The analysis

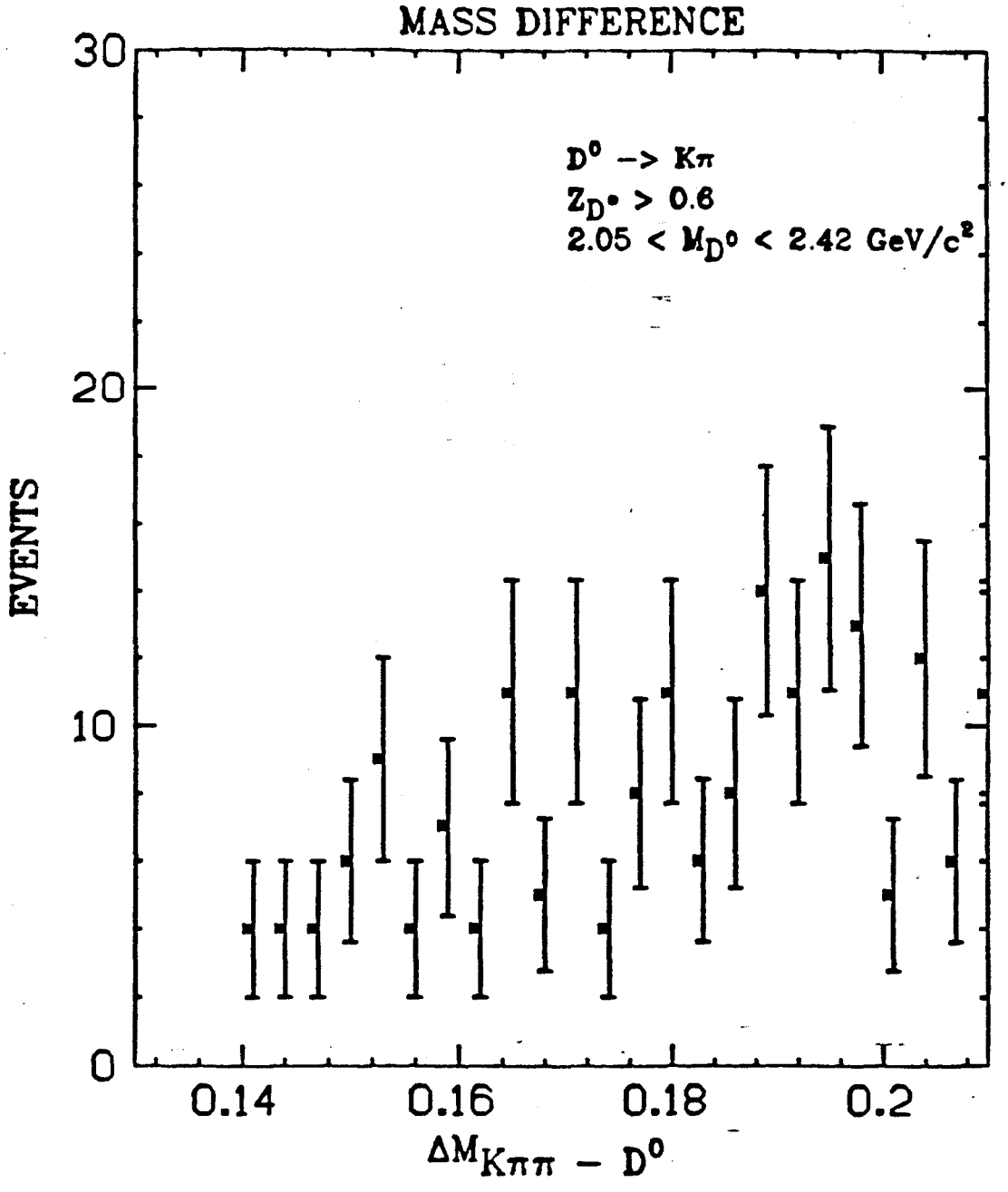

Fig. 38: Mass difference values for D^0 control sample

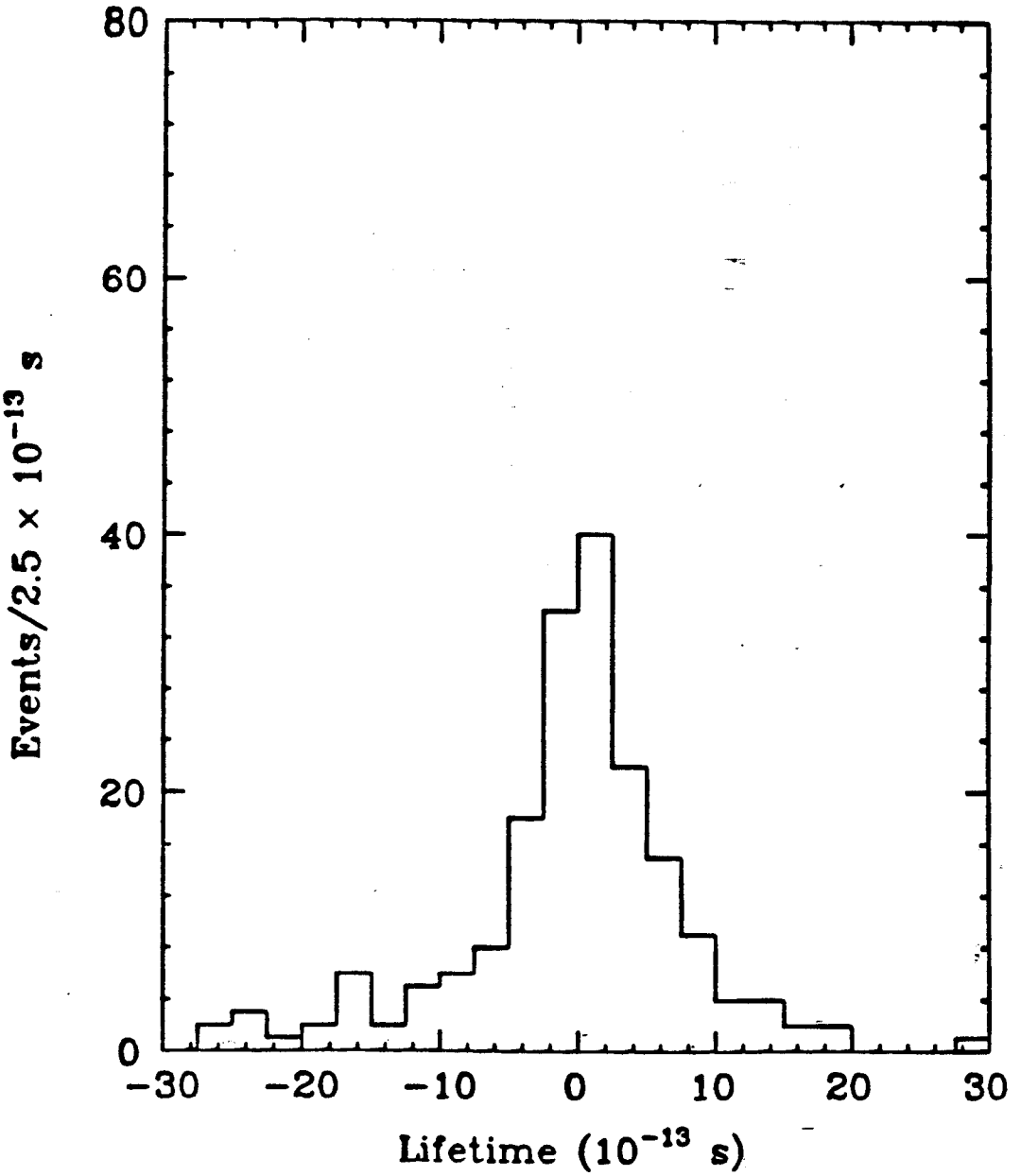

Fig. 39: Lifetime distribution for the D^0 control sample

procedure locates D^+ mesons via the decay reaction

$$D^{*+} \rightarrow D^+\pi^0$$
$$\hookrightarrow K^-\pi^+\pi^+$$

The event sample is selected using cuts as similar as possible to those of the D^0 analysis in order to minimize any systematic differences between the measurements of the lifetimes of the D^0 and D^+ . As with the D^0 , cuts are done in two stages. The first stage attempts to show evidence for the signal by maximizing the efficiency for the decay mode specified above. The second stage of cuts eliminates events which have been mismeasured in some way. The D^+ flight path length is measured by finding the non-beam-constrained vertex of the K and two π's from the D^+ and using the standard formula for estimating the most likely decay length relative to the known beam position.

The first stage of cuts are as follows:

- Events are not considered unless they have event vertices with R less than 2 cm and |z| less than 15 cm (with respect to the beam position) and more than 25% of the total center-of-mass energy in charged and neutral tracks

- No particle ID is attempted, instead all tracks with R less than 5 cm, |z| less than 15 cm, 10 or more dazms, and a total track-fit χ^2 /dof less than 7 are considered as both a K and a π. dE/dx corrections to the particle momenta are made according to the particle type assumed

- π^0 candidates are made from gammas which have energy between 0.1 and 1 GeV and position coordinates within the LA fiducial volume. π^0 candidates are rejected if the invariant mass of the two gammas used is less than 20 MeV/c^2 or greater than 500 MeV/c^2 or the χ^2 /dof of the fit to the π^0 mass

is greater than 6. Candidates are also rejected if the π^0 momentum is less than 300 MeV.

As expected, there is no evidence of a peak in the invariant mass spectrum for $K\pi\pi$ combinations. $K\pi\pi$ candidates with an invariant mass between 1.68 and 2.05 GeV/c^2 are defined to be D^+ candidates. These candidates are then combined with each π^0 candidate in the event to form $K\pi\pi\pi^0$ combinations. Fig. 40, the plot of the mass difference, $\Delta M_{K\pi\pi\pi^0-D^+}$, shows little evidence of a peak until use is made of the fact that the ratio of the π^0 energy to the D^{*+} energy is nearly a constant because of the small Q value of the decay. Fig. 41 shows the range of detected values for this quantity for Monte Carlo produced D^{*+} 's decaying to $D^+ \pi^0$. Fig. 42 shows the mass difference values for D^{*+} candidates with ratios between 0.045 and 0.105 and z (energy of the D^{*+} /beam energy) above 0.6. We will determine the significance of the peak in fig. 42 by performing the same analysis on a control sample.

The control sample is determined using all of the stage 1 cuts described above, with the exception of the invariant mass cut. Control sample D^+ 's must have invariant mass between 2.05 and 2.42 GeV/c^2. There is one additional cut applied. If a track, when combined with another track of opposite charge, gives a pair with an invariant mass within 20 MeV/c^2 of the K^0_s mass or within 10 MeV/c^2 of the Λ mass, then that track is not considered as part of a control sample candidate. The plot of the mass difference for the control sample D^{*+} 's after the ratio cut discussed above is shown in fig. 43. Note that this distribution peaks at a $\Delta M_{K\pi\pi\pi^0-D^+}$ of $\sim$ 152 MeV/c^2 before dropping to zero on the low end due to phase space. Similar behavior occurs in the corresponding region outside the peak in fig. 42. As a double-check on the shape of the phase space around the signal region, the analysis is repeated on a control sample in which

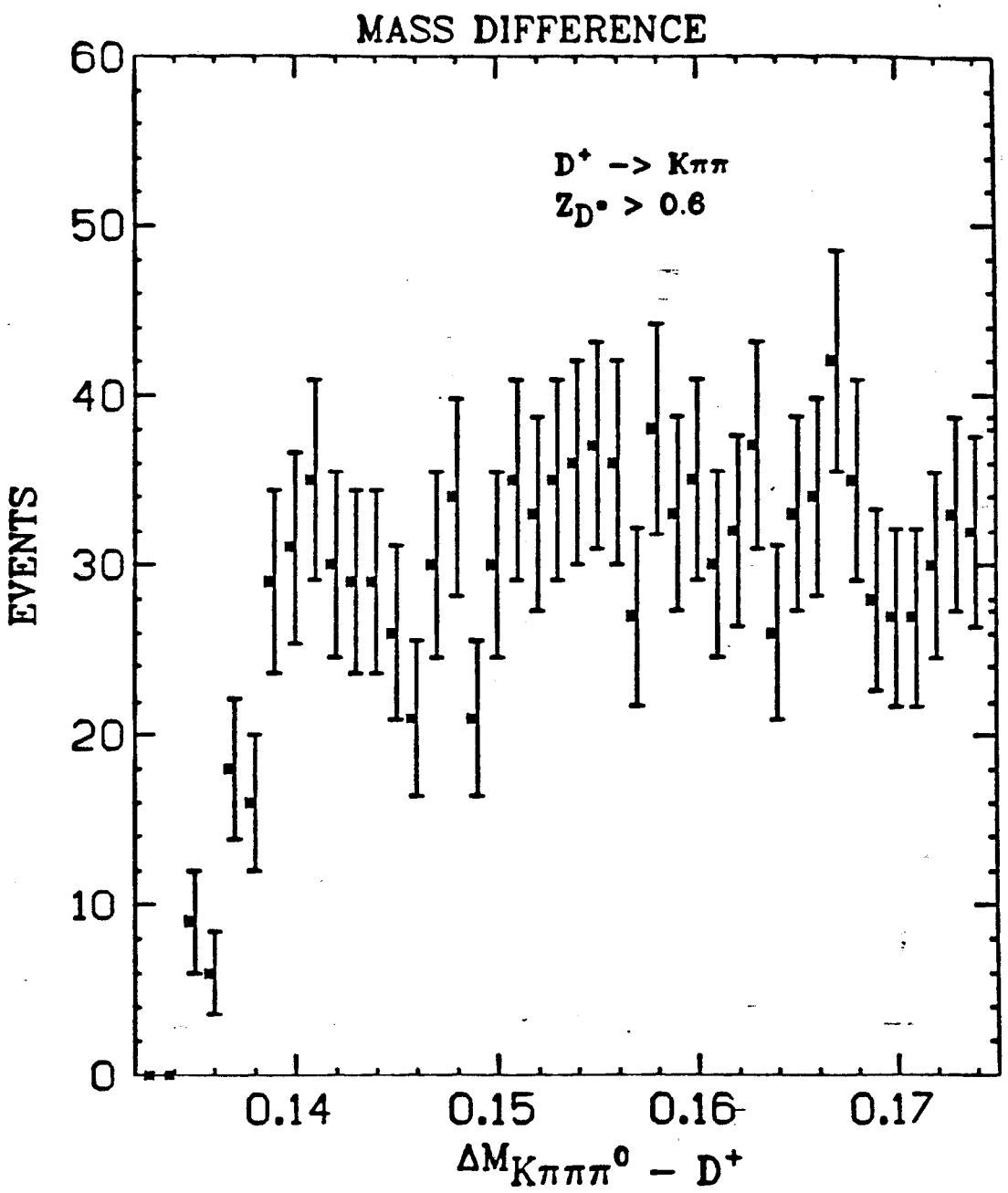

Fig. 40: Mass difference distribution for $D^{*+} \to D^{+}\pi^{0}, D^{+} \to K\pi\pi$ before a cut on the ratio of π^{0} energy to D^{*+} energy

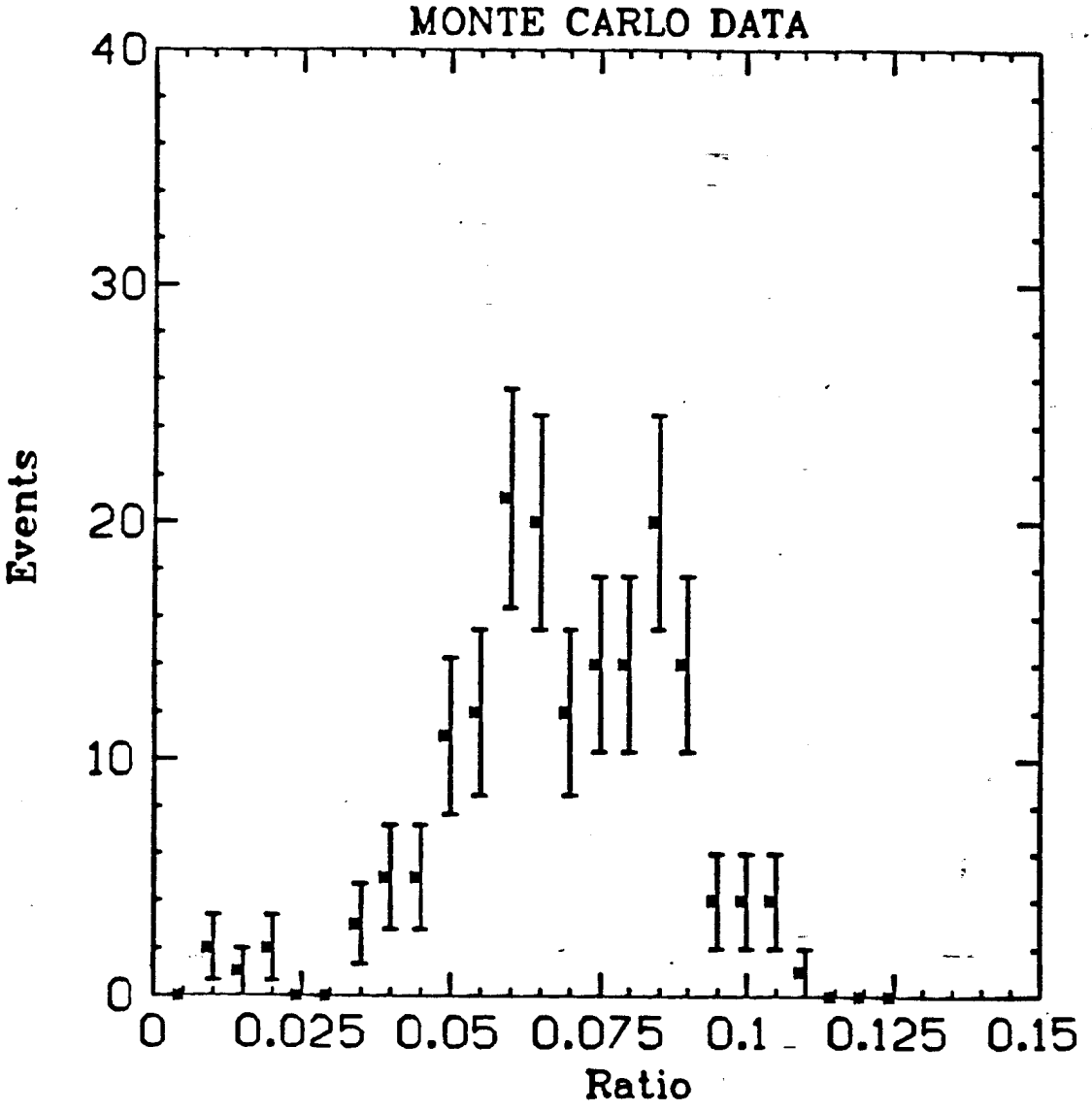

Fig. 41: Plot of the detected ratio of π^0 energy to D^{*+} energy for a Monte Carlo simulation of the process $D^{*+} \rightarrow D^+\pi^0; D^+ \rightarrow K\pi\pi$

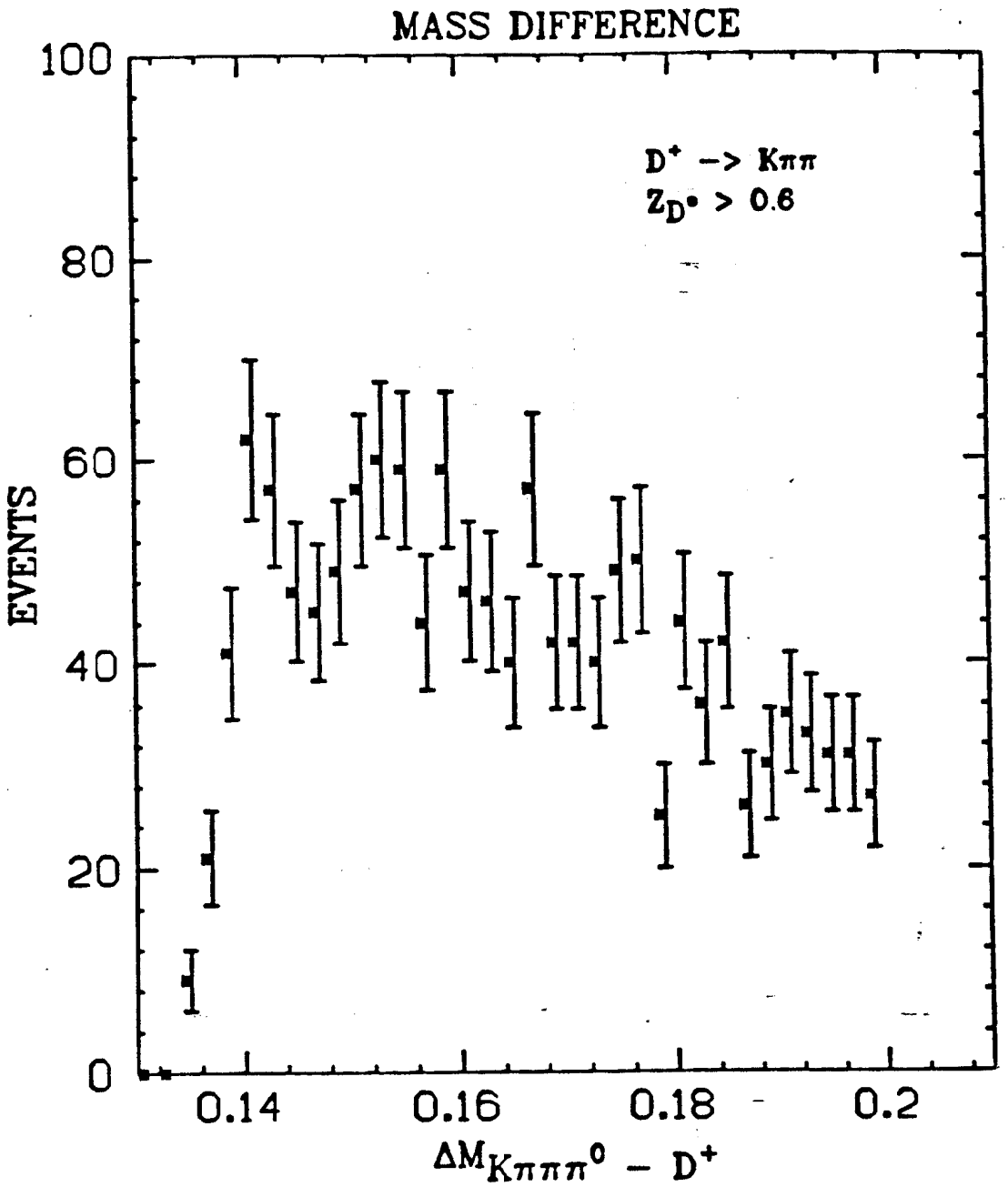

Fig. 42: Mass difference distribution after a cut on the ratio of π^0 energy to D^{*+} energy

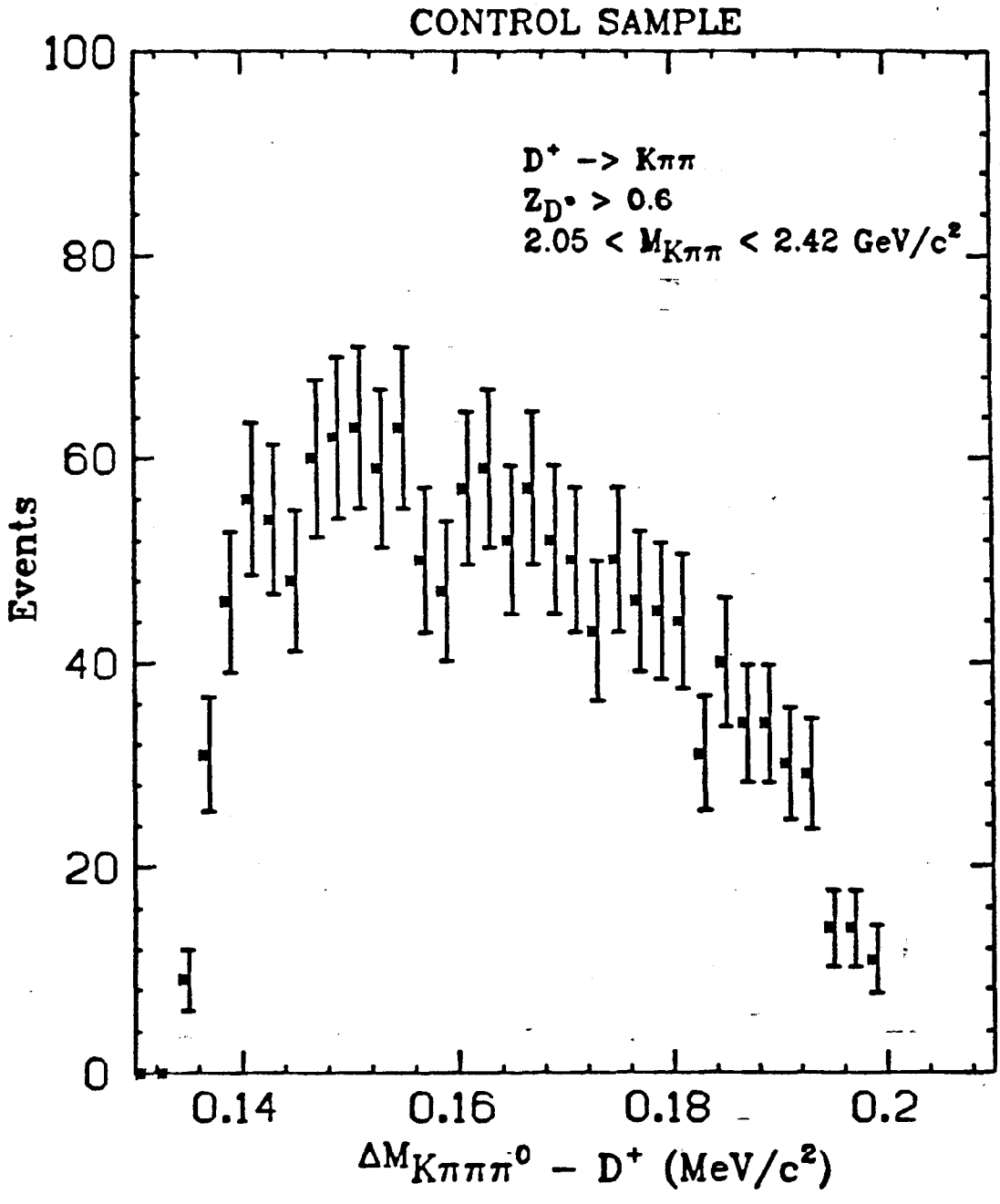

Fig. 43: Mass difference distribution for control sample events in which the invariant mass of the fake D^+ lies between 2.05 and 2.42 GeV/c^2

the fake D^+ 's have an invariant mass between 1.31 and 1.67 GeV/c^2. The $\Delta M_{K\pi\pi\pi^0-D^+}$ distribution for this control sample is shown in fig. 44. Keep in mind that the numbers in these plots are deceptive since there are roughly 3 π^0 candidates for each $K\pi\pi$ combination in both the data and the control sample. Fig. 45 shows the invariant mass of the gammas from the π^0 candidates in the D^+ data sample.

In order to avoid any bias in the selection of events put through the lifetime analysis, the lifetime-algorithm is applied to both D^{*+} candidates and candidates from both control samples which have z> 0.6 and $\Delta M_{K\pi\pi\pi^0-D^+}$ less than 200 MeV/c^2, regardless of their ratio value. The events are retracked using the method described in section 2.11. The second stage of cuts applied to D^{*+} tracks are as follows:

- R and z less than 2 cm and 5 cm, respectively
- total track-fit χ^2 less than 7, VC track-fit χ^2 less than 5
- 10 or more dazms of which at least 2 must be in the inner layers of the VC and at least 1 must be in the outer layers of the VC
- track momentum greater than 300 MeV/c
- no other tracks are allowed to be within $\frac{1}{5}$ of a wire spacing of a D^{*+} charged track at each VC layer

In addition, any VC dazm on the decay tracks which contributes more than 3/dof to the VC track fit χ^2 is eliminated. The track is then refit and passed through the above cuts again. A maximum of three dazms are allowed to be removed in this way. For π^0 candidates, we simply demand that the χ^2 /dof for the fit to the π^0 mass be less than 3.

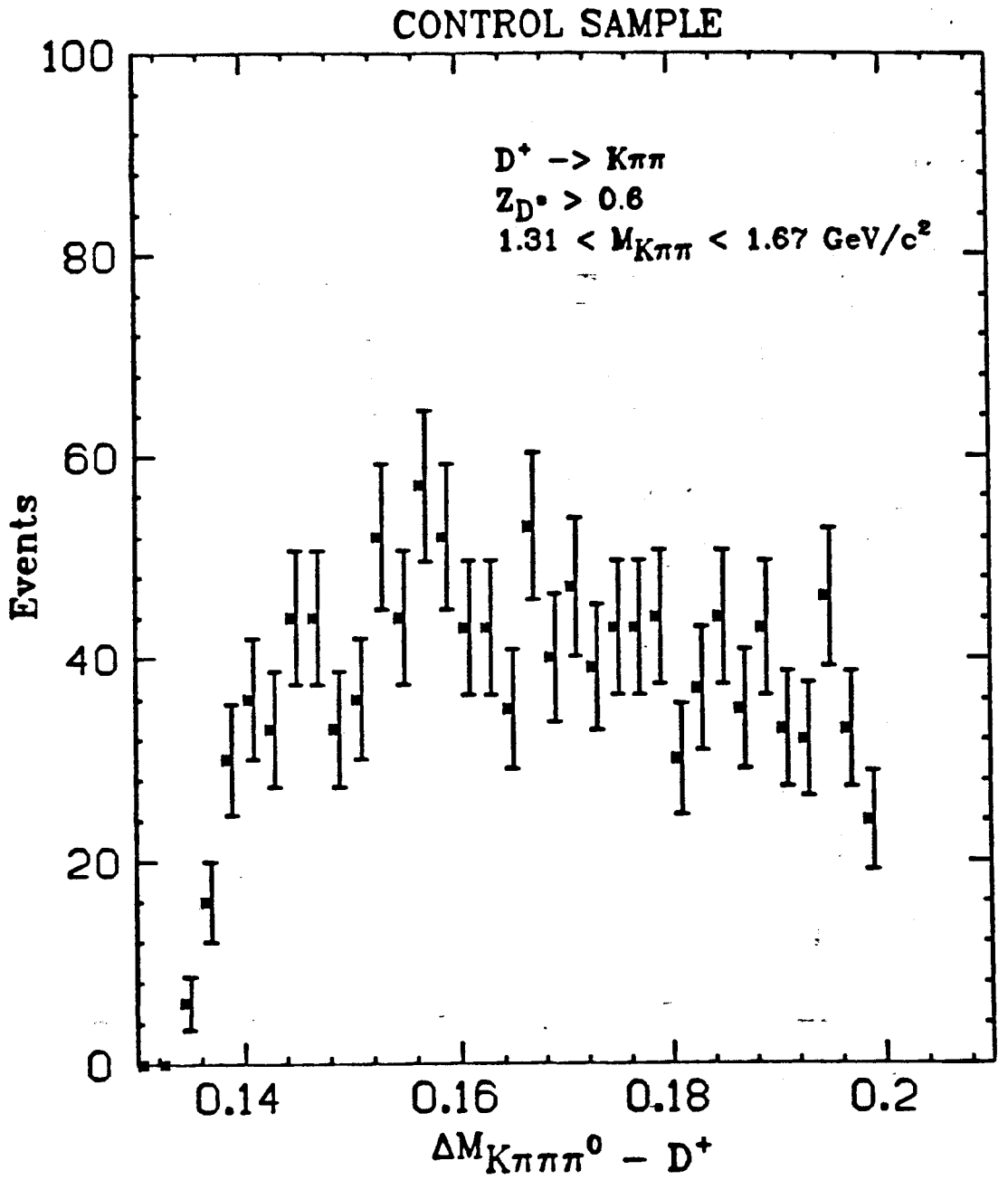

Fig. 44: Mass difference distribution for control sample events in which the invariant mass of the fake D^+ lies between 1.31 and 1.67 GeV/c^2

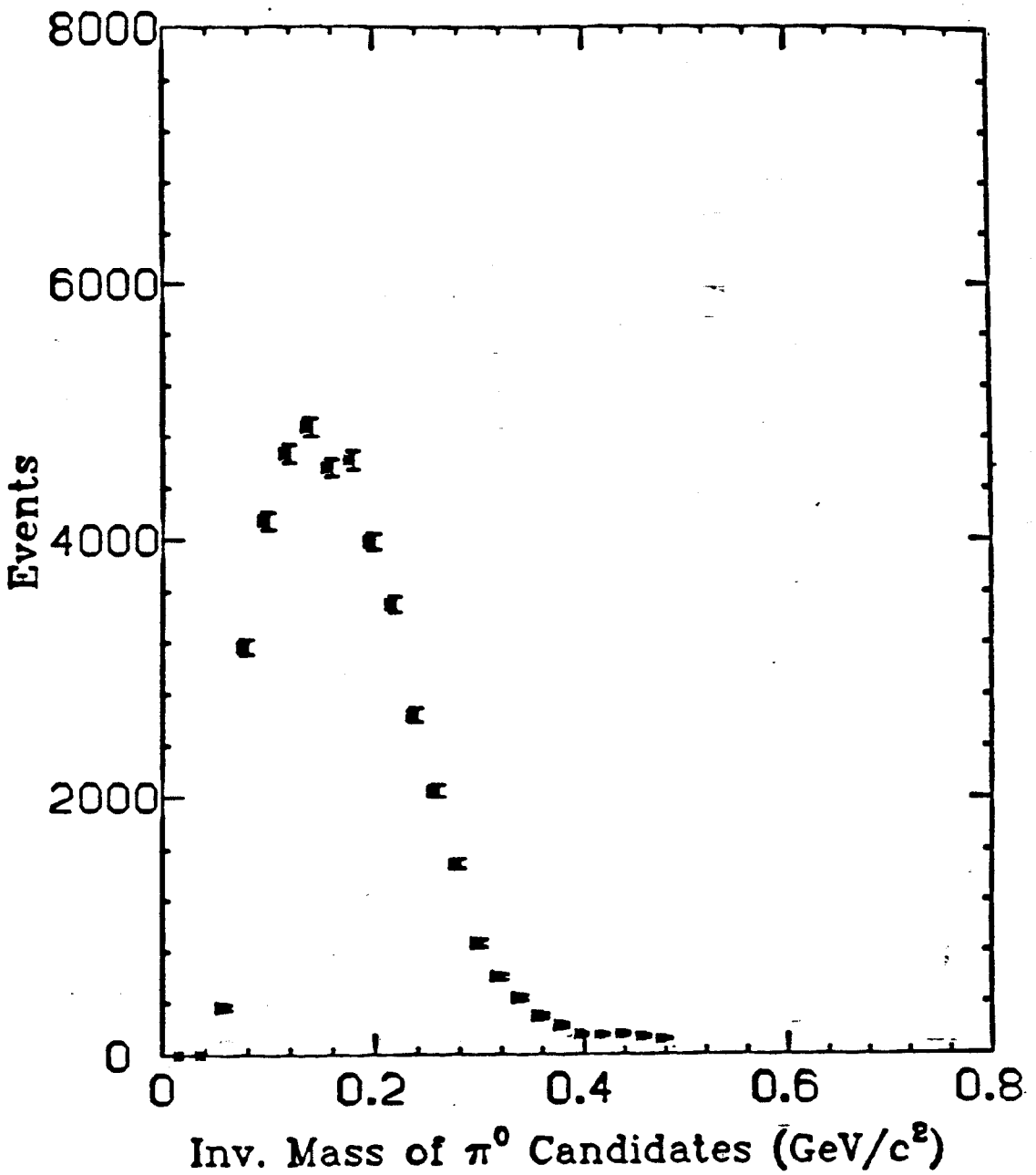

Fig. 45: Invariant masses of π^0 candidates used in D^+ sample

As in the D^0 analysis, a vertex fit of the K and π's of the D^+ were made after track errors were boosted by 10%. Vertex errors are boosted by 8% after the fit. D^+ candidates are required to have a $\chi/\text{dof} < 3$ for the vertex fit of the three tracks. We also required that the D^+ flight trajectory be consistent (within 3 σ) with the hypothesis that it originates in the vicinity of the beam interaction spot.

At this point in the D^0 lifetime analysis, a cut was made on the χ^2 of a vertex fit of the bachelor pion and the virtual D^0 track. It was argued that this cut provided not only a consistency check on the D^{*+} hypothesis, but a better determination, in principle of the relative angle between the D^0 and the bachelor pion. This, in turn, should slightly improve the mass difference resolution. For the D^+ analysis, we simply make use of the fact mentioned above, namely that the ratio of bachelor π^0 energy to total D^{*+} energy must be nearly a constant for all legitimate D^{*+} events going through the $D^+\pi^0$ decay mode. Demanding that the D^{*+} candidates have a ratio between bounds set by the Monte Carlo simulation of the decay allows a rejection of background with little loss of signal.

Two further checks are made to verify that the $K\pi\pi\pi^0$ candidates are consistent with coming from D^{*+} decays. As in the D^0 analysis, we ask that no D^{*+} candidate in the lifetime sample have a bachelor π^0 with momentum greater than 1.3 GeV/c. Secondly, we ask that the χ^2/dof of the kinematic fit of the K, π and π momenta to the D^+ mass be less than 4. The final kinematic fit was done using track information constrained by the vertex fit described above. This ensures maximum precision on the $\Delta M_{K\pi\pi\pi^0-D^+}$ determination.

Even after all cuts, some multiple-counting of events remains (i.e. some charged track combinations can be combined with several π^0 candidates in the same event). Multiple-counting is eliminated by selecting the D^{*+} candidate

with the smallest χ^2 for the π^0 fit, or in cases with several D^+ candidates, the smallest SQUAW-fit χ^2 .

Figs. 46-48 show the mass difference distribution after all cuts for the data, the high invariant mass control sample, and the low invariant mass control sample, respectively. We can again see an indication of peaking in the control sample distributions for $\Delta M_{K\pi\pi\pi^0-D^+} \sim 154$ MeV/c^2 for the control samples, although the statistics are too limited too draw any firm conclusions. The extremely low number of events in the low-invariant mass control sample results primarily from the track overlap cut. The lower invariant mass of the fake D^+ 's leads to smaller opening angles, and hence a greater probability of overlapping tracks. In order to determine the amount of combinatoric background in figure 46, we first determined the shape of the mass difference distribution for the high and low invariant mass control samples. We increased the statistics of these samples by eliminating the cuts on the number of vertex chamber hits, on the chi-square of the track fit, and the chi-square of the vertex fit. Cuts on tracks which overlap and on the ratio of bachelor π^0 energy to D^{*+} energy were retained. The mass difference distribution of these control samples made with modified cuts were then fit with a trial function which had parameters controlling the shape and normalization. These parameters were allowed to vary until an optimal least-squares fit was obtained. Fig. 49 shows the mass difference distribution for the high and low invariant mass control samples along with the best fit to the data for this function. We then fixed the parameters which controlled the shape of the function and fit the data in figures 47 and 48 to determine the normalization for the high and low-invariant mass control samples. The normalization for the combinatoric background in fig. 46 was determined by interpolating between the values of the two control samples. The solid curve in fig. 46 shows the shape

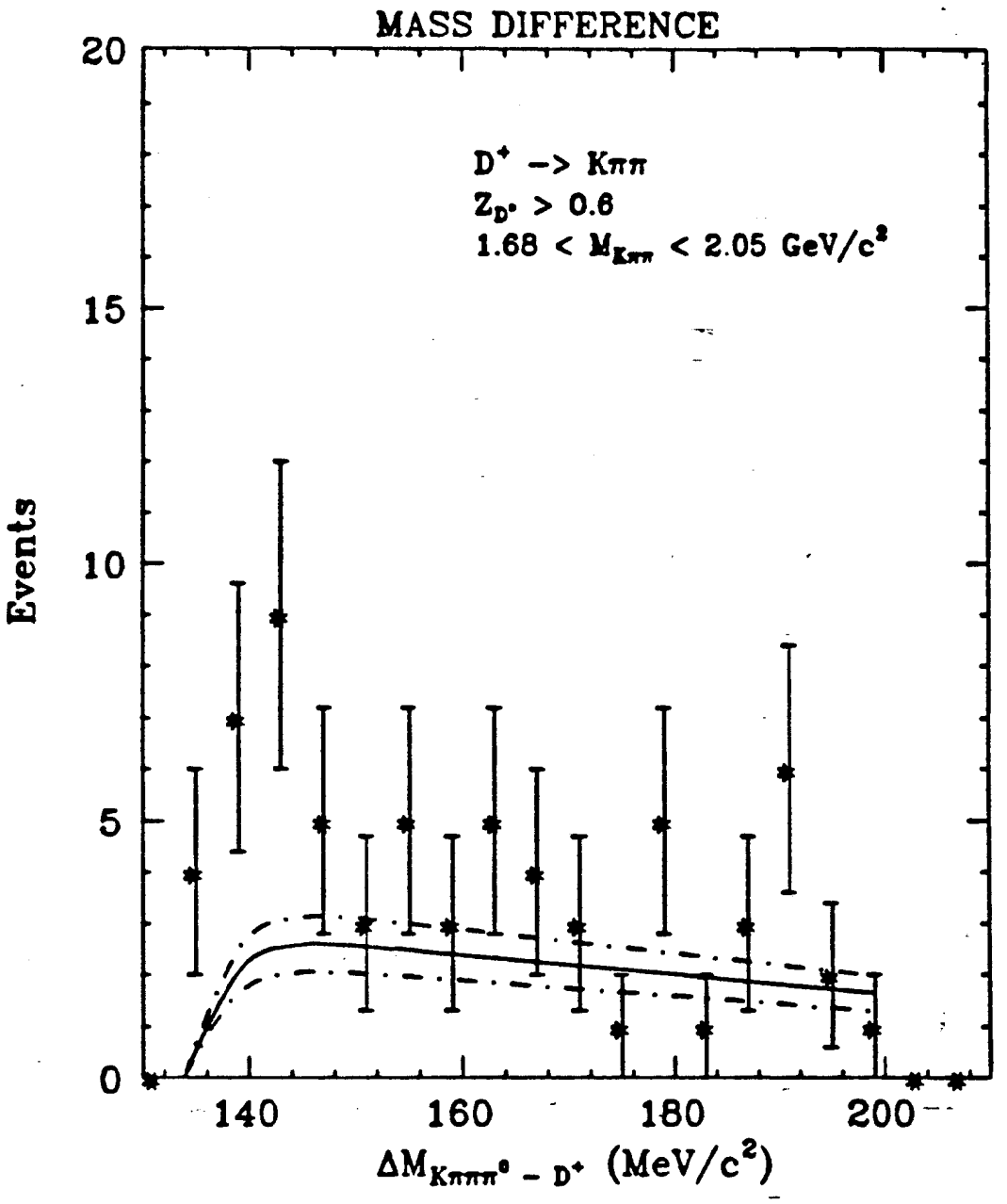

Fig. 46: Mass difference distribution for D^+ sample after all cuts

The solid curve shows the estimated background distribution, the dotted-dashed lines show the 1 sigma limits on this estimate

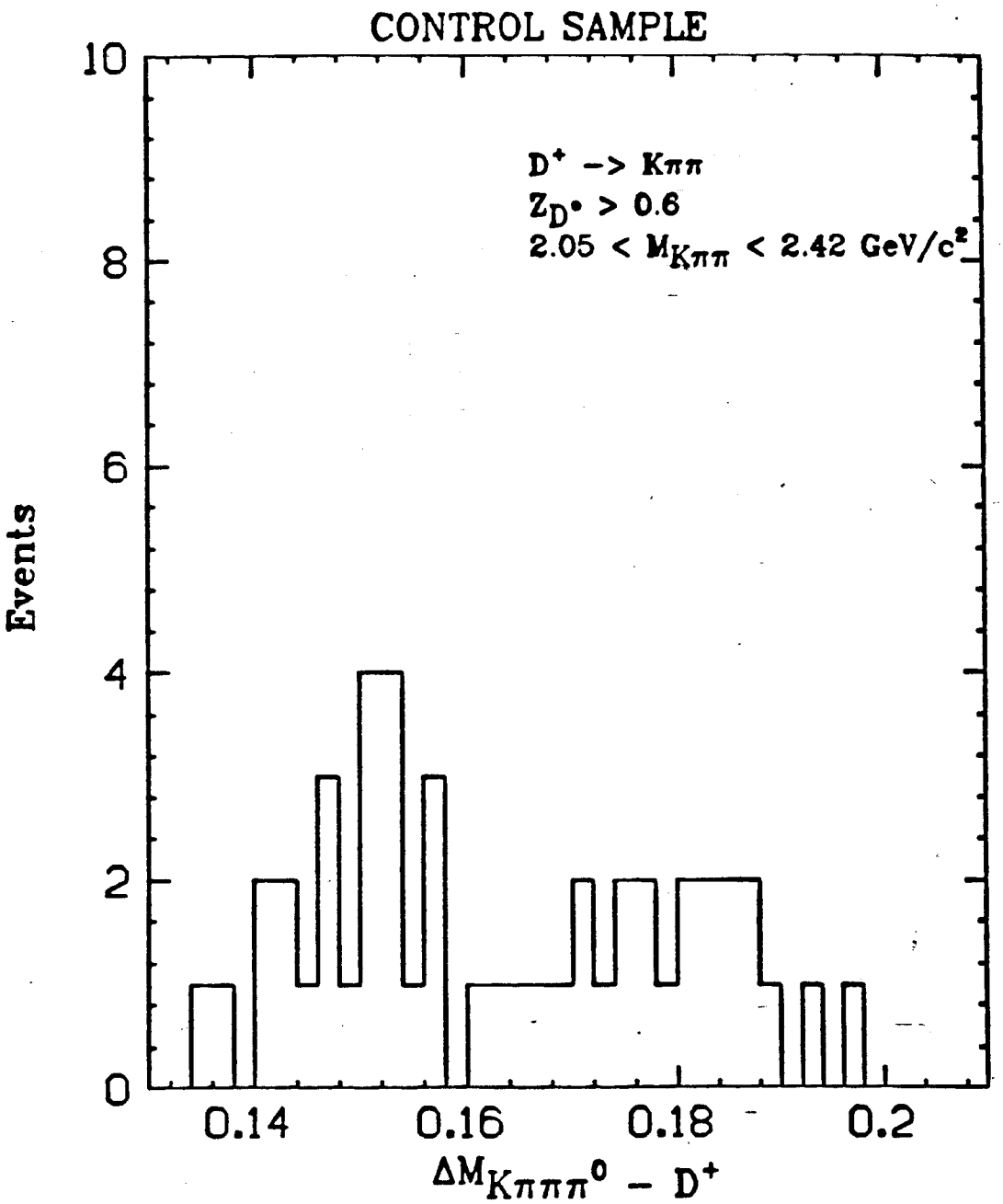

Fig. 47: Mass difference distribution for high-invariant mass control sample after all cuts

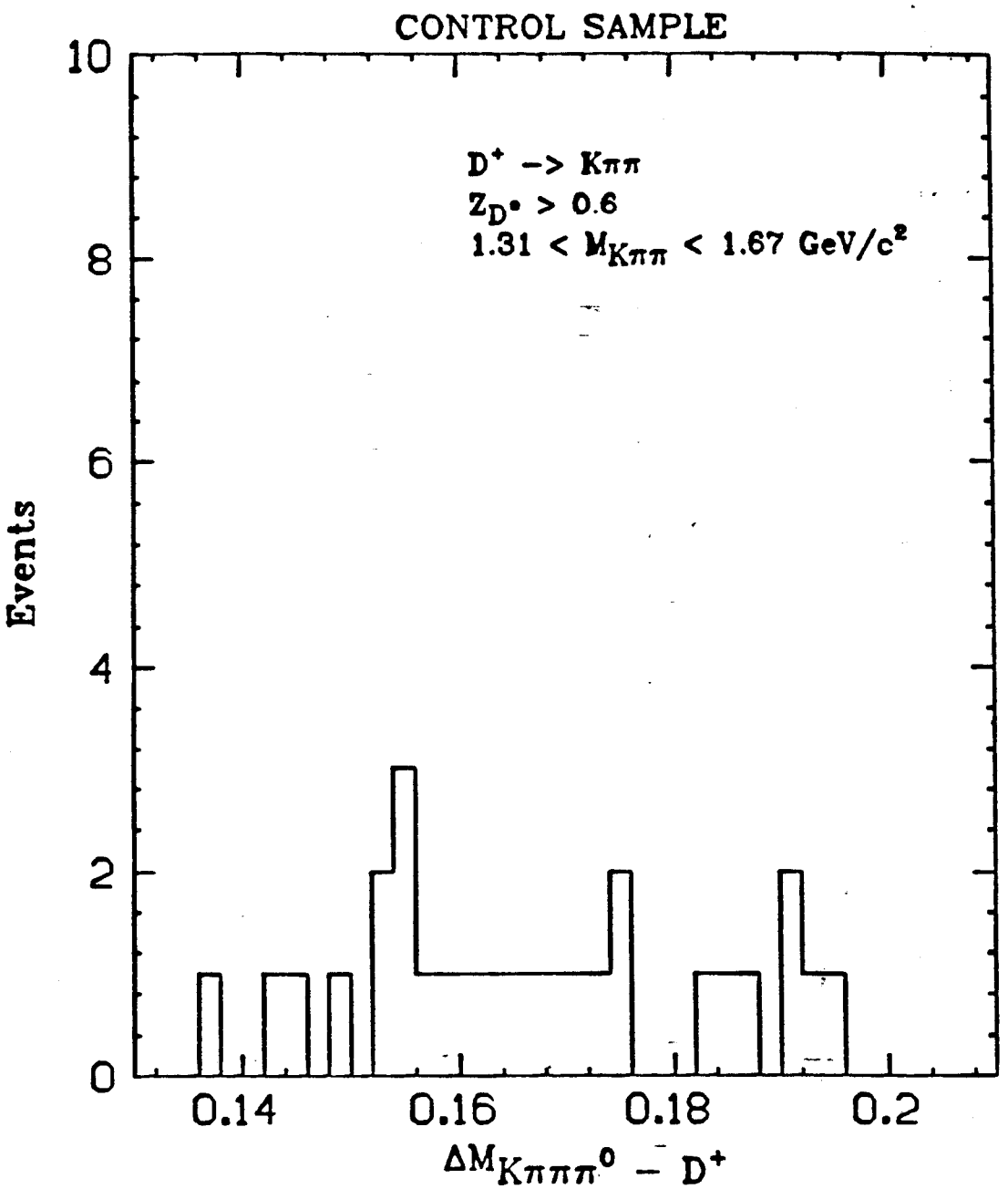

Fig. 48: Mass difference distribution for low-invariant mass control sample after all cuts

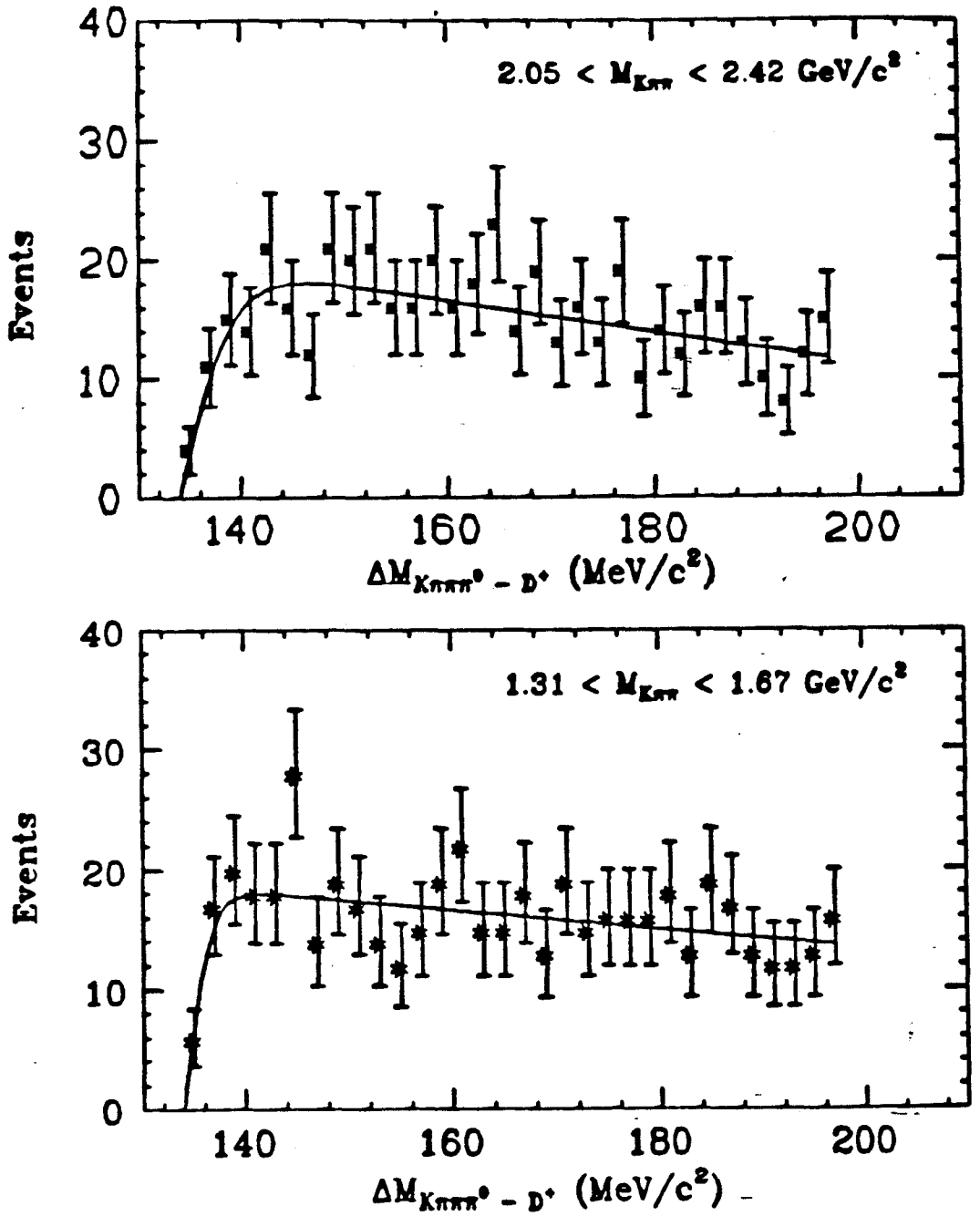

Fig. 49: Mass difference distribution after cuts on the ratio of π^0 energy to D^{*+} energy and no overlapping of tracks for $K\pi\pi\pi^0$ combinations with a $K\pi\pi$ invariant mass between

a. 2.05 and 2.42 GeV/c^2

b. 1.31 and 1.67 GeV/c^2

of the expected combinatoric background distribution. The dotted-dashed lines show the 1 sigma boundaries of this curve. On the basis of a Monte Carlo study of the $D^{*+} \rightarrow D^+\pi^0$ reaction, we have determined that the excess of events outside the D^{*+} signal region is consistent with the mass resolution smearing of the D^{*+} peak due to the poor resolution on the determination of the bachelor π^0 momentum. We have used the background curve to estimate the combinatoric background from $135 < \Delta M_{K\pi\pi\pi^0-D^+} < 146$ GeV/c^2 to be 5.7 ± 3.6 events. Using Monte Carlo techniques, we have also determined that two other backgrounds arise in the analysis. The number of D^{*+} mesons from B decays, for example, is estimated to be $3 \pm 2\%$. Events from the reaction,

$$D^{*0} \rightarrow D^0\pi^0$$
$$\hookrightarrow K^-\pi^+$$

in which the K and π from the D^0 are combined with a random track to make a D^+ candidate provide $14 \pm 6\%$ of the events in the signal region. The background from other charm channels is negligible.

Now that the amount of background has been determined, we must measure its lifetime. In order to increase the statistics on the lifetime measurement, the low and high invariant mass control samples are combined. This assumes that the difference in vertex errors between the samples has little effect on any systematic mismeasurement of the lifetimes. This assumption has been checked for the D^0 sample and for the D^+ data sample as will be discussed below. Fig. 50 shows the lifetime distribution for the combined control sample. The mean lifetime, assuming a Gaussian distribution, is $0.8 \pm 0.5 \times 10^{-13}$ s. We can now determine the mean lifetime of the D^+ sample under the following assumptions:

i. the combinatorial background under the peak in fig. 46 has a mean lifetime identical to that of the control sample

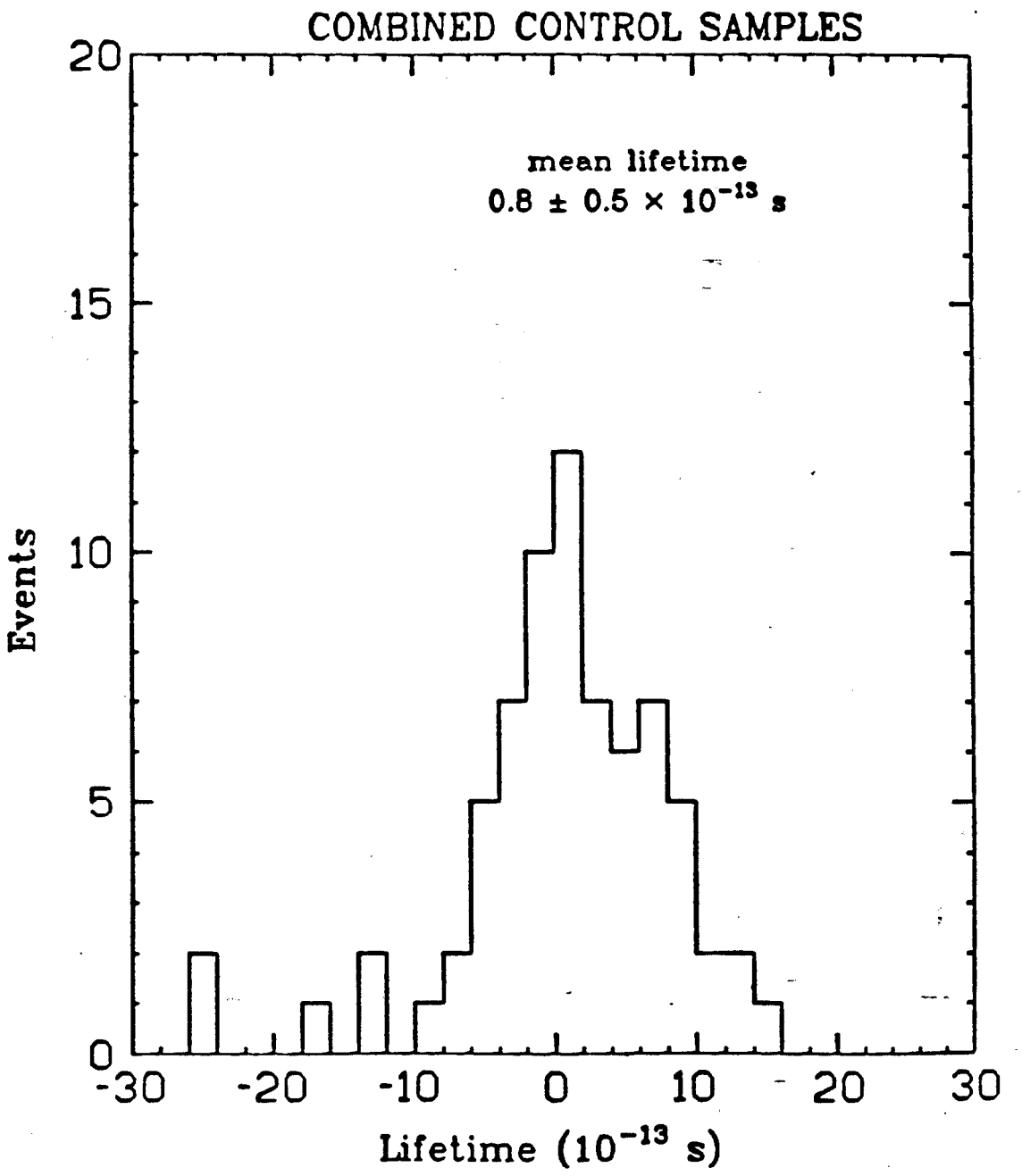

Fig. 50: Lifetimes of combined control sample events

ii. the combinatorial background fraction is $25 \pm 15\%$

iii. the background from B hadrons is 3% as in the D^0 lifetime analysis

The fitting function employed in the D^0 lifetime measurement was modified to include the effects of the D^{*0} background and the slightly larger lifetime of the combinatoric background. It was then used to derive a value of $8.9^{+3.8}_{-2.7} \times 10^{-13}$ s as the mean lifetime of the D^+ sample. A plot of the D^+ sample lifetimes along with the curve showing the fitting function is shown in fig. 51. A similar analysis done on a Monte Carlo simulation of the D^{*+} to D^+ reaction yields $8.4^{+1.9}_{-1.5} \times 10^{-13}$ s for an input lifetime of 9.5×10^{-13} s.

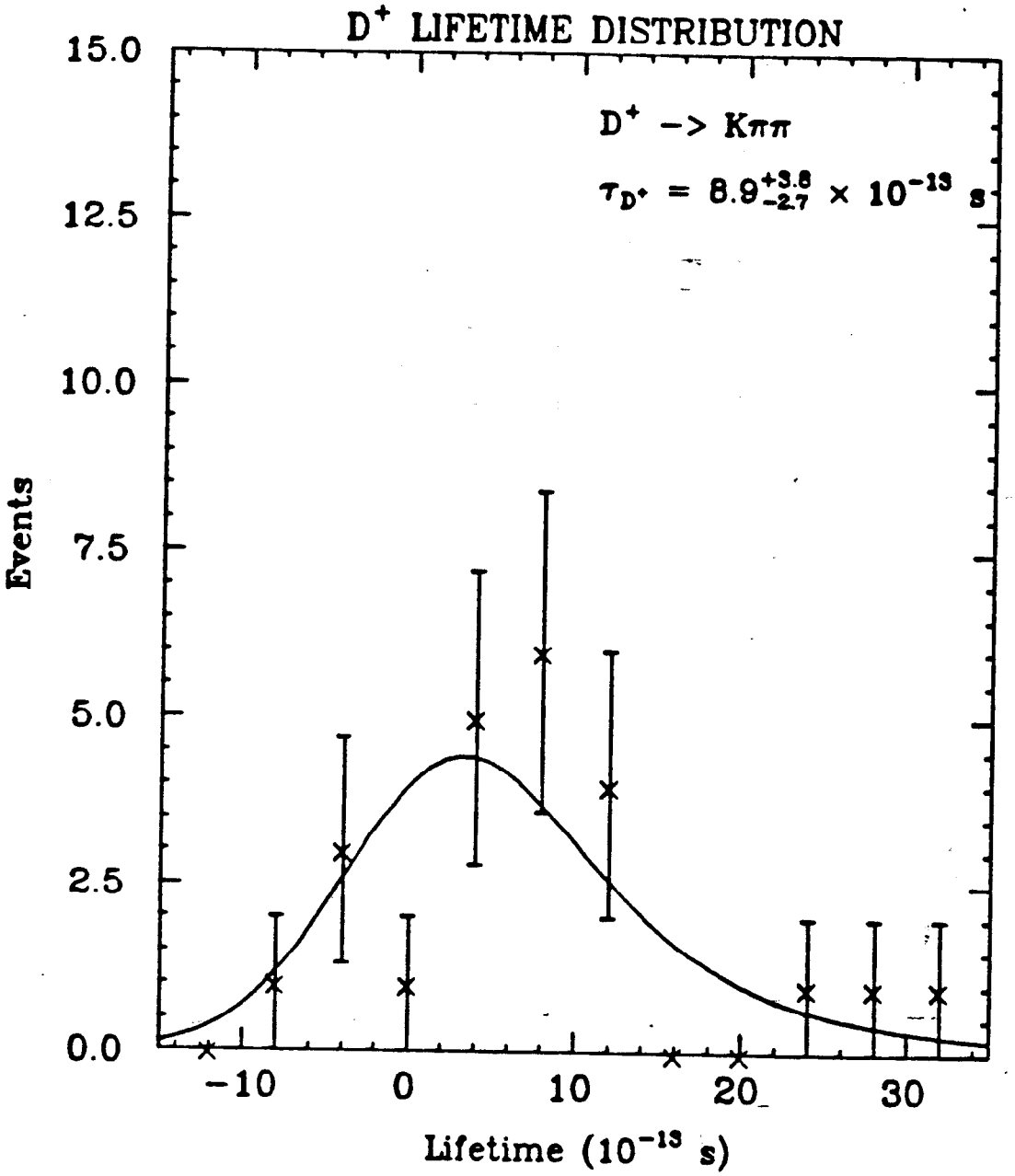

Fig. 51: Lifetimes of D^+ sample events along with the curve from the fitting function

6. Studies of Systematic Errors

In this chapter, we will determine the systematic error on the lifetime measurements for the D^0 and D^+ . Although the contributions to the systematic error for the analyses are fairly similar, the methods for determining them differ in detail. Therefore, they will be described separately. We will begin with a check on the general lifetime algorithm by making a measurement of the τ lifetime.

6.1 τ Lifetime Study

Lifetime studies at an e^+e^- storage ring offer at least one advantage over similar studies done at hadron machines. This is the existence of an event sample with a lifetime which is not only very similar to the lifetime of the charmed mesons which we wish to study but which is well-understood both theoretically and experimentally. We are speaking here, of course, about τ lepton events. The lifetime of the τ is derived by the same arguments discussed in chapter 1. Hence,

$$\tau_\tau = \mathrm{Br}(e) \cdot \left(\frac{m_\mu}{m_\tau}\right)^5 \cdot \tau_\mu = 2.8 \times 10^{-13}\ \mathrm{s}$$

where Br(e) is the branching ratio for $\tau \rightarrow e\nu_e\nu_\tau$. The current best measurement of the τ lifetime is $2.80 \pm 0.24 \pm 0.25 \times 10^{-13}$ s[36] . Since τ 's are readily identified at PEP energies and fairly plentiful, it is easy to obtain a relatively clean τ sample and make a rough estimate of its lifetime. Since the τ is well-understood both theoretically and experimentally, this sample provides an excellent test bed for the techniques described above.

At 29 GeV, a clean sample of τ events can be chosen largely on the basis of the topology of the event. For example, in this study we looked at events with a 1+3 topology, i.e. events which have 1 track recoiling against 3 tracks pointing into the opposite hemisphere. Specifically, we choose events with 4 charged tracks

with 0 net charge and total energy between 5 and 26 GeV. The lower limit on the total energy rejects τ pairs produced from 2-photon processes while the upper limit rejects radiative Bhabha and muon pairs which have converted photons. Each event is divided into two jets by a plane perpendicular to the thrust axis. Events are rejected unless one of the jets contain exactly three prongs which have an invariant mass between 0.7 and 1.5 GeV/c^2 and energy between 3 and 15 GeV. Furthermore, all tracks in one jet are required to be more than 120° from all tracks in the opposite jet. All tracks are required to be well-measured according to the stage 2 criteria applied to the D mesons. Monte Carlo calculations are used to estimate backgrounds in the final sample of 4% from low-multiplicity hadronic events and 3% from two-photon produced τ pairs[36]. This sample of τ events is then passed through the lifetime algorithm in order to determine the mean decay length of the sample. Fig. 52 shows the distribution of decay lengths found. The mean value is $647 \pm 72\mu$. This can be compared to the 680μ expected from the current world average for the τ lifetime. Since these values are in good agreement, we conclude that the lifetime measuring method used here is basically sound and shows no obvious bias.

6.2 Systematic Error for D^0 Analysis

For the D^0 analysis, contributions to the systematic error are broken down as follows:

- $\pm 0.3 \times 10^{-13}$ s for any systematic offset as measured by the agreement between the real data and Monte Carlo data control samples

- $\pm 0.2 \times 10^{-13}$ s from the uncertainty on the amount of combinatorial hadronic background

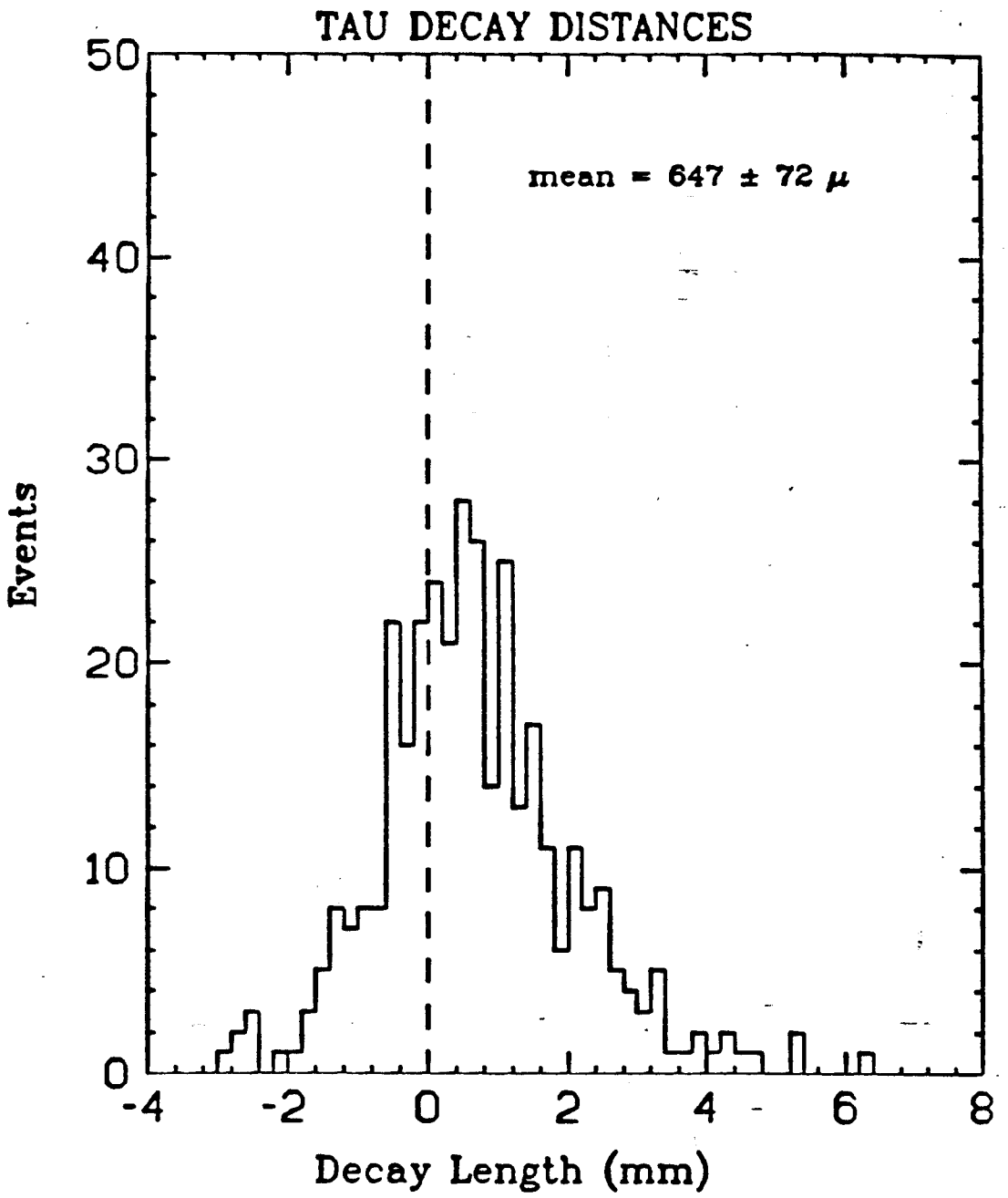

Fig. 52: Decay length distribution for τ leptons

- $\pm 0.1 \times 10^{-13}$ s from the uncertainty on the amount of $B \rightarrow D^{*+}$ background
- $\pm 0.2 \times 10^{-13}$ s for reasonable variations in the errors assigned to the proper decay times

Each of these will be discussed below.

The first error is determined by estimating the possible systematic offset in the measurement of the mean lifetime of a sample. This is calculated by estimating the offset from 0 of the D^0 control sample. As stated in section 5.5, the mean lifetime of the D^0 control sample is $0.6 \pm 0.3 \times 10^{-13}$ s. This agrees with the expectation from the Monte Carlo control sample which has a mean lifetime of $0.5 \pm 0.2 \times 10^{-13}$ s. Measurements were also made on several Monte Carlo data sets in which each event had one reaction of the type $D^{*+} \rightarrow D^0\pi, D^0 \rightarrow K\pi$ (the charm quark opposite the D^{*+} was allowed to fragment in the normal manner). The values used are in Appendix B. Table 4 contains the various measured values for the mean lifetime as the lifetime of the D^0 was changed.

Table 4.

Lifetime Measurements on Monte Carlo Data Samples

Input lifetime	Measured lifetime (10^{-13} s)
0.0	$0.3 \pm .47$
3.1	$2.8 \pm .41$
6.2	$-5.9 \pm .41$

Since there is no observed offset at any lifetime in the Monte Carlo and the control samples for the real data and the Monte Carlo agree within the statistical error of 0.3×10^{-13} s, we claim that the 1 sigma limit on any systematic offset in measuring the lifetime of the D^0 sample is $\pm 0.3 \times 10^{-13}$ s.

The second contribution is derived by adjusting the proportion of combinatorial and B meson backgrounds in the fitting function according to the maximum amount of each background that could exist in the D^0 sample. As stated in section 5.4, the mean lifetime of $4.7^{+0.9}_{-0.8} \times 10^{-13}$ for the D^0 sample was calculated with contributions from combinatorial background and B-hadrons included. The amount of combinatoric background in the lifetime sample is estimated by straight-line fits to the events outside the D^{*+} peak in figs. 27 and 33. This yields $12 \pm 6\%$ as the best estimate of the combinatoric background fraction for the $K\pi$ decay mode and $14 \pm 6\%$ as background fraction for the $K\pi\pi^0$ mode. The amount of B-hadron contamination is estimated by a Monte Carlo study as described in section 5.1. The lifetime of the combinatoric background is assumed to be the same as that of the real data control sample, 0.6×10^{-13} s. The lifetime of B-hadrons was set to 10^{-12} s[37] . Varying the combinatoric background fraction in the fitting function from 6 to 18% changes the mean lifetime by $\mp 0.2 \times 10^{-13}$ s. Adjusting the B-hadron background fraction between 1 and 5% changes the mean lifetime by $\pm 0.1 \times 10^{-13}$ s. It should be noted that the two backgrounds have opposite effects on the mean lifetime of the sample.

The third error depends on the correct determination of the vertex error boost mentioned previously. In principle, one would like to determine the correct boost to the vertex error by studying the lifetime/estimated error of an appropriate control sample. This has in fact been done for the τ lifetime analysis[36]. That study found that the distribution of lifetime/error is a Gaussian of small mean, but with a width of 1.13 ± 0.05. This indicates a vertex error which is about 13% too small given the distribution of the lifetimes from a sample with a small *mean* lifetime. The additional 13% error presumably comes from misassignment and mistiming of VC hits on tracks which are too close together. Unfortunately,

it is not possible to repeat this study accurately for this analysis due to the lack of a large control sample. It should be noted, for example, that the width of the control sample lifetime distribution in fig. 39 is notably narrower than the lifetime distribution of the D^0 sample. This occurs primarily because the control sample is formed with track pairs which have an invariant mass above the D^0 mass band. This tends to make the fake D^0 's have wider opening angles and therefore smaller vertex errors than the real D^0 decays. This point cannot, of course, be corrected, but, we can attempt to at least check on the vertex error boost by measuring the lifetime/estimated error distribution of this sample, shown in fig.53. The data is reasonably well-fit by a Gaussian of width 1.08 ± 0.06. Our determination is consistent with that of the τ lifetime analysis. Hence, 1.08 is taken to be correct value for the error boost. The systematic error on the D^0 lifetime from the boost is estimated by measuring the difference between the mean lifetime of the D^0 sample with a 1.0 and 1.16 vertex error boost. Without the boost, the lifetime is $4.9^{+0.9}_{-0.8} \times 10^{-13}$ s. With a 16% error boost, the lifetime goes to $4.5^{+0.9}_{-0.8} \times 10^{-13}$ s. The contribution to the systematic error is therefore assumed to be $\pm 0.2 \times 10^{-13}$ s.

The last error to be considered is the bias against long-lived events. The efficiency for detecting D mesons cannot be completely independent of lifetime since, if the lifetime is too long (say 10^{-11} s or more) then the decay length would place the decay tracks outside the inner layers of the VC. Although the data seen in fig. 37 shows no hint of disagreement with the hypothesis that all D^0 decays have a single lifetime of about 4×10^{-13} s, it is possible that there may be a bias against the longest-lived events from a sample with this lifetime. In order to determine the efficiency for such events, we have performed a study on a large sample of Monte Carlo events which all included the decay sequence

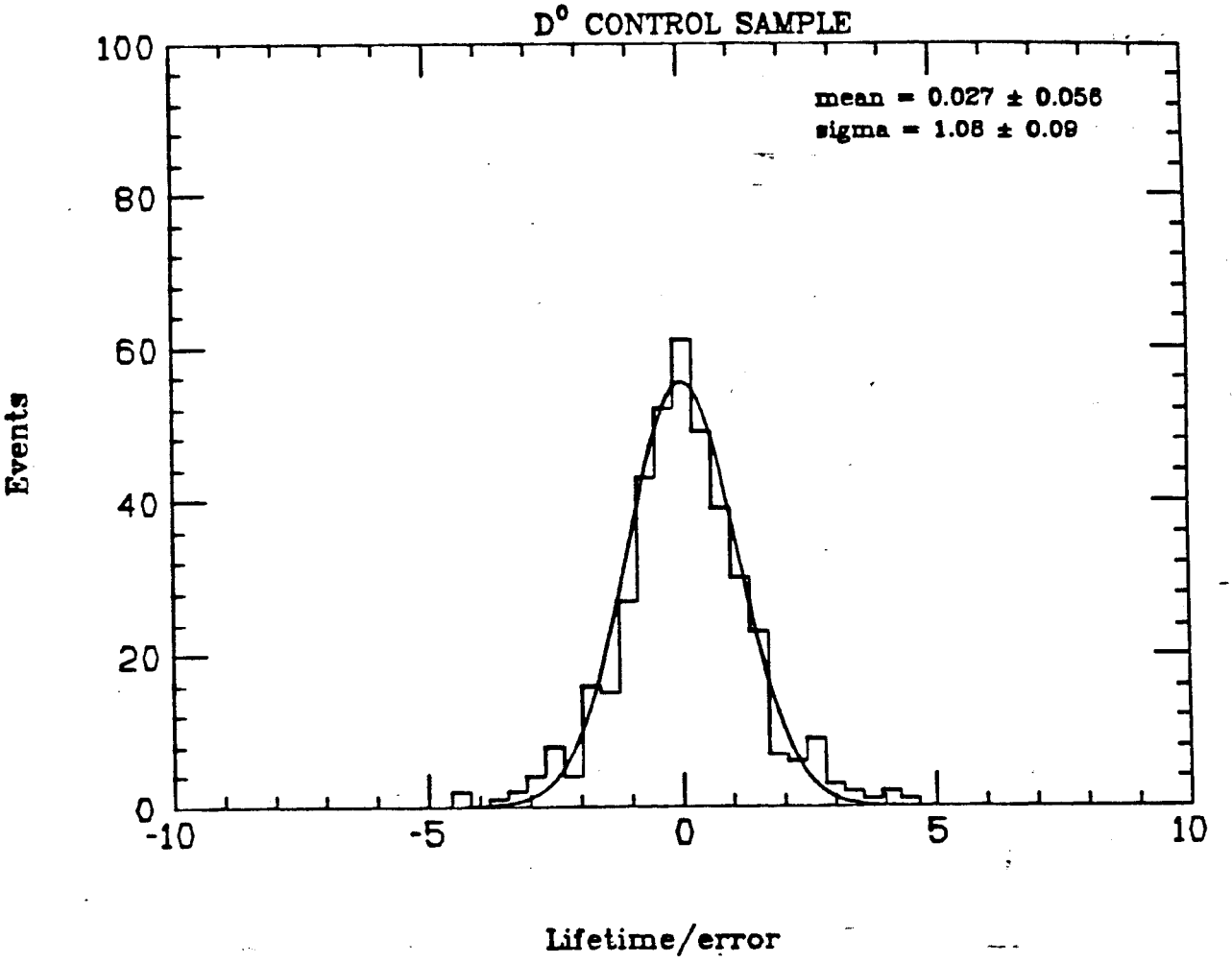

Fig. 53: Distribution of lifetime/error for the D^0 control sample along with a curve showing the best fit Gaussian for the data between -3 and 3 sigma

$D^0 \to K\pi$. The D^0 lifetime was set to 62×10^{-13} s, about 15 times the current world average. The events are run through the same analysis procedure used on real data. The resultant lifetime is $59.4^{+6.0}_{-5.3} \times 10^{-13}$ s for the 111 events which pass all cuts. Thus, there is no indication of bias in measuring lifetimes from a sample with a mean lifetime about an order of magnitude higher than the measurements presented here.

Adding all of the errors previously discussed in quadrature gives a systematic error of 0.5×10^{-13} s. Thus, the final answer for the D^0 lifetime is

$$4.7^{+0.9}_{-0.8} \pm 0.5 \times 10^{-13} \text{ s.}$$

6.3 Systematic error for D^+ Analysis

The contributions to the systematic error on the D^+ lifetime measurement are as follows:

- 1.1×10^{-13} s from the uncertainty in the amount of combinatorial background
- 0.3×10^{-13} s from the uncertainty in the amount of B hadron background
- 0.2×10^{-13} s from the uncertainty about the correct value for the vertex error boost
- 0.5×10^{-13} s from the possibility of a systematic offset in the lifetime measurement

The first error reflects the changes in the lifetime which occur when the amount of background specified in the fitting function is changed. For 40% combinatorial background in the 23 signal events, the lifetime becomes $10.2^{+4.1}_{-2.8} \times 10^{-13}$ s.

For a background fraction of 9%, the lifetime goes to $7.8^{+3.0}_{-2.2} \times 10^{-13}$ s. When the amount of B background is changed to 1% or 5%, the lifetime becomes $9.2^{+3.8}_{-2.6} \times 10^{-13}$ s or $8.6^{+3.8}_{-2.7} \times 10^{-13}$ s, respectively. The third error reflects changes in the measured lifetime for various changes in the vertex error boost discussed in the previous section. If this 8% boost is increased by a factor of two, then the lifetime becomes $8.8^{+3.8}_{-2.7} \times 10^{-13}$ s. If no boost is used, the lifetime is $9.3^{+3.8}_{-2.6} \times 10^{-13}$ s. The fourth error is an estimate of the magnitude of a possible systematic mismeasurement of the D^+ lifetime due to a systematic mismeasurement of the vertex position. This is done by estimating the offset from zero of the D^+ control sample. The problem here, of course, is that there is always some residual B and charm background in the control samples, thus their lifetimes are always slightly positive. Since the D^+ analysis avoided using the Monte Carlo as much as possible, we have compared the D^+ control sample lifetime to that of the D^0 control sample described earlier. The D^0 control samples for Monte Carlo data and real data agree quite well and indicate that an offset of about 0.5×10^{-13} s can be expected due to the residual charm and B tracks in the sample. The D^+ control sample lifetime agrees with this within its statistical error of $\pm 0.5 \times 10^{-13}$ s. Therefore, we take 0.5×10^{-13} s as the limit of any measurement offset. These errors are added in quadrature to get a final systematic error of $\pm 1.3 \times 10^{-13}$ s. The quoted error includes the small dependence of the D^+ lifetime on the D^0 lifetime measurement. Thus, the final value for the D^+ lifetime is $8.9^{+3.8}_{-2.7} \pm 1.3 \times 10^{-13}$ s.

7. Conclusions

Now that we have our best estimates of the D^0 and D^+ lifetimes along with the systematic errors associated with the measurements, we can compare our values to those of other experiments. We have found

$$\tau_{D^0} = 4.7^{+0.9}_{-0.8} \pm 0.5 \times 10^{-13} \text{ s}$$

$$\tau_{D^+} = 8.9^{+3.8}_{-2.7} \pm 1.3 \times 10^{-13} \text{ s}$$

The ratio of lifetimes, assuming independent errors for the D^+ and D^0 is $\frac{\tau_{D^\pm}}{\tau_{D^0}} = 1.9^{+0.9}_{-0.7} \pm 0.3$. Fig. 54 shows the current published measurements of τ_{D^0} from emulsion, bubble chamber, and silicon strip detectors along with the present measurement[38–45] . The current world average, excluding the value presented here is $3.83 \pm .32 \times 10^{-13}$ s. Fig. 55 contains the current published values of τ_{D^+}. The current world average, excluding the measurement presented here is $8.92 \pm .87 \times 10^{-13}$ s. The world average values can be divided to yield a ratio of $2.33 \pm .30$. Thus, the results of this measurement are in good agreement with the results from other experiments.

When taken all together, the measurements indicate that the lifetimes of the D^0 and D^+ are very close to the theoretically predicted value for the charm quark lifetime. This is a good indication that the overall properties of the hadronic decays of these mesons can be explained by the Standard Model for weak interactions. The discrepancy between the D^0 and D^+ lifetimes definitely indicates, however, that the naive spectator model is not completely correct. One possible source of the difference might be in the Cabibbo-suppressed decays of these mesons. Since the D^+ and D^0 partial decay widths to Cabibbo-favored semileptonic final states are equal (assuming isospin symmetry), a comparison of the ratio of the D^+ and D^0 semileptonic branching ratios to the ratio of D^+ and

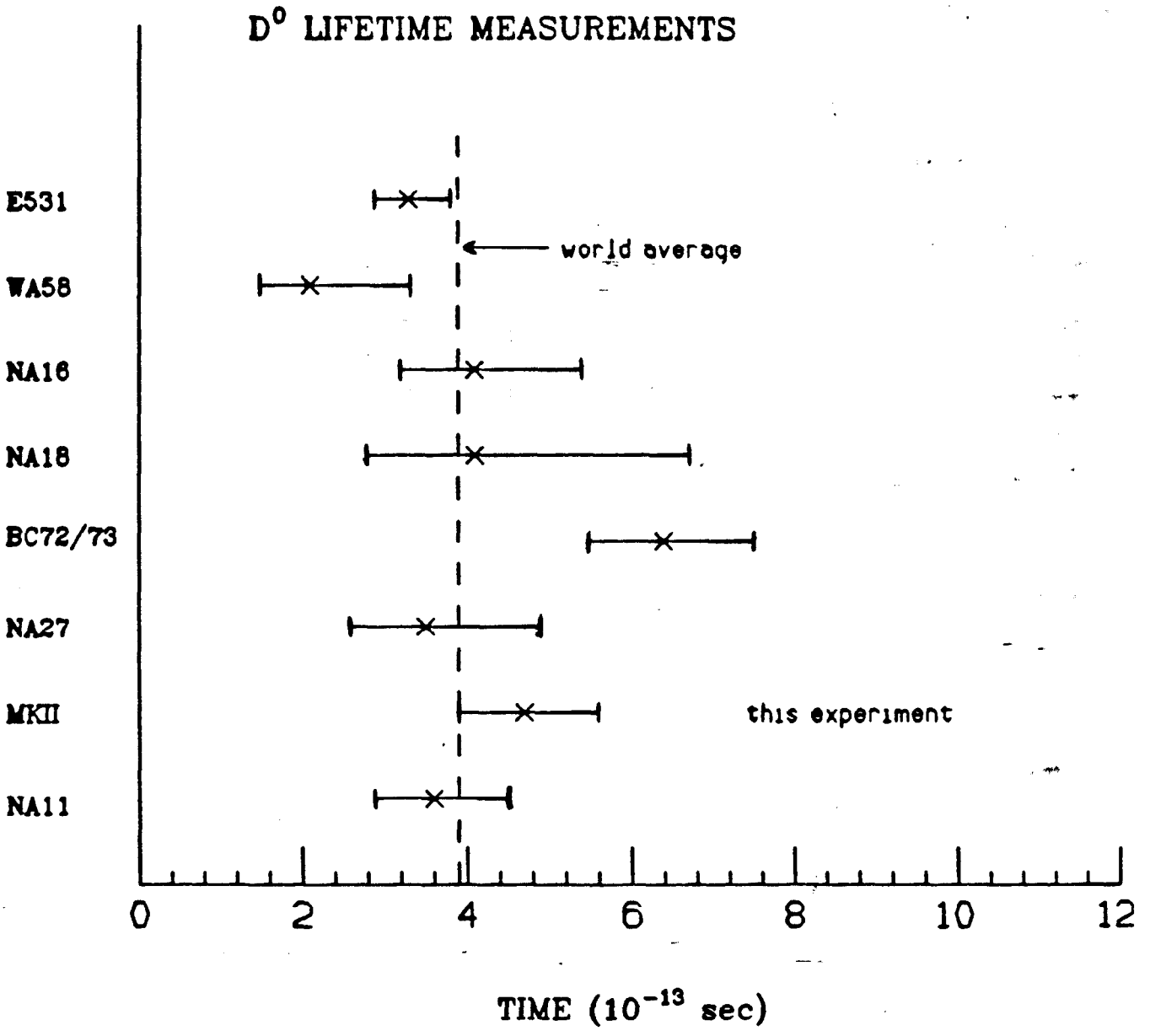

Fig. 54: Current experimental measurements of the D^0 lifetime

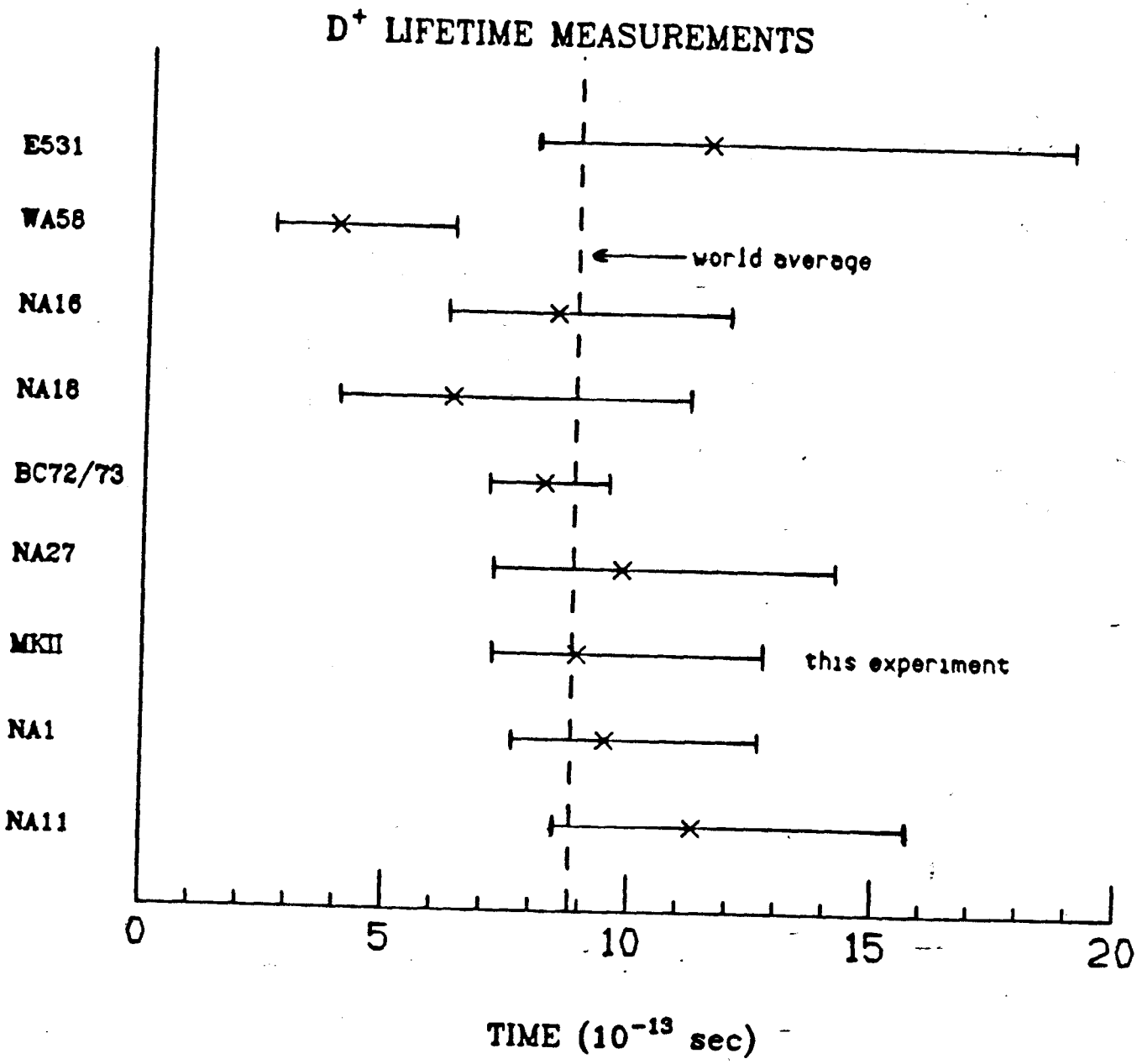

Fig. 55: Current experimental measurements of the D^+ lifetime

D^0 lifetimes places limits on the size of the Cabibbo-suppressed semileptonic widths. The best measurement to date of the semileptonic branching ratios comes from the MarkIII experiment[46] . They find

$$\frac{Br(D^+ \to e^+ + X)}{Br(D^0 \to e^+ + X)} = 2.3^{+0.5}_{-0.4} \pm 0.1.$$

When compared to our measurement, this implies

$$\frac{\Gamma_{D^+ \to e^+ + X}}{\Gamma_{D^0 \to e^+ + X}} = 1.2^{+0.6}_{-0.5} \qquad \text{statistical errors only.}$$

The diagrams for Cabibbo-suppressed semileptonic decay of the D^+ is shown in fig. 57. Assuming isospin conservation, there is no comparable diagram for the D^0 . Thus, the ratio of semileptonic widths can be expressed as

$$\frac{\Gamma^{CA}_{D^+ \to e^+ + X} + \Gamma^{CS}_{D^+ \to e^+ + X}}{\Gamma^{CA}_{D^0 \to e^+ + X}} = 1 + \frac{\Gamma^{CS}_{D^+ \to e^+ + X}}{\Gamma^{CA}_{D^0 \to e^+ + X}} = 1.2^{+0.6}_{-0.5}$$

where CA stands for Cabibbo-allowed and CS for Cabibbo-suppressed. Thus,

$$\frac{\Gamma^{CS}_{D^+ \to e^+ + X}}{\Gamma^{CA}_{D^0 \to e^+ + X}} < 1.4$$

at the 95% CL.

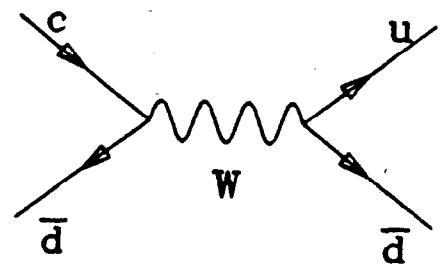

Fig. 56: Diagram for Cabibbo-suppressed decay of the D^+ meson

Appendix

We will now describe the solution to the χ^2-minimization expression derived in chapter 3. The derivation is due to George Trilling. We start with the equation

$$\frac{\partial \chi^2}{\partial \beta^{(\nu=1,N)}_{l=1,3}} = \sum_{k=1}^{N} \sum_{i,j=1}^{5} \left\{ \frac{\partial \mathcal{A}_i^{(k)}}{\partial \beta_l^{(\nu)}} H_{ij}^{(k)} \left[\mathcal{A}_j^{(k)} - \alpha_j^{(k)} \right] + \left(\mathcal{A}_i^{(k)} - \alpha_i^{(k)} \right) H_{ij}^{(k)} \frac{\partial \mathcal{A}_j^{(k)}}{\partial \beta_l^{(\nu)}} \right\} = 0$$

Note that the symmetry of the inverse error matrices ($H_{ij}^{(k)} = H_{ji}^{(k)}$) allows us to simplify the above equations to

$$\frac{\partial \chi^2}{\partial \beta^{(\nu=1,N)}_{l=1,3}} = 2 \sum_{k=1}^{N} \sum_{i,j=1}^{5} (\mathcal{A}_i^{(k)} - \alpha_i^{(k)}) H_{ij}^{(k)} \frac{\partial \mathcal{A}_j^{(k)}}{\partial \beta_l^{(\nu)}} = 0.$$

and

$$\frac{\partial \chi^2}{\partial x_{l=1,3}} = 2 \sum_{k=1}^{N} \sum_{i,j=1}^{5} \left(\mathcal{A}_i^{(k)} - \alpha_i^{(k)} \right) H_{ij}^{(k)} \frac{\partial \mathcal{A}_j^{(k)}}{\partial x_l} = 0.$$

In order to solve these equations, we first linearize them by approximating the track parameters $\mathcal{A}^{(k)}$ with the form

$$\mathcal{A}_i^{(k)} = \mathcal{A}_{i0}^{(k)} + \sum_{q=1}^{N} \sum_{m=1}^{3} \delta \beta_m^{(q)} \frac{\partial \mathcal{A}_i^{(k)}}{\partial \beta_m^{(q)}} + \sum_{m=1}^{3} \delta x_m \frac{\partial \mathcal{A}_i^{(k)}}{\partial x_m}.$$

Thus, we get

$$\frac{\partial \chi^2}{\partial \beta_l^{(\nu)}} = 2 \sum_{k=1}^{N} \sum_{i,j=1}^{5} \left\{ \mathcal{A}_{i0}^{(k)} + \sum_{q=1}^{N} \sum_{m=1}^{3} \delta \beta_m^{(q)} \frac{\partial \mathcal{A}_i^{(k)}}{\partial \beta_m^{(q)}} + \sum_{m=1}^{3} \delta x_m \frac{\partial \mathcal{A}_i^{(k)}}{\partial x_m} - \alpha_i^{(k)} \right\} H_{ij}^{(k)} \frac{\partial \mathcal{A}_j^{(k)}}{\partial \beta_l^{(\nu)}} = 0$$

and

$$\frac{\partial \chi^2}{\partial x_l} = 2 \sum_{k=1}^{N} \sum_{i,j=1}^{5} \left\{ \mathcal{A}_{i0}^{(k)} + \sum_{q=1}^{N} \sum_{m=1}^{3} \delta \beta_m^{(q)} \frac{\partial \mathcal{A}_i^{(k)}}{\partial \beta_m^{(q)}} + \sum_{m=1}^{3} \delta x_m \frac{\partial \mathcal{A}_i^{(k)}}{\partial x_m} - \alpha_i^{(k)} \right\} H_{ij}^{(k)} \frac{\partial \mathcal{A}_j^{(k)}}{\partial x_l} = 0.$$

This yields 3N+3 equations which must be solved for 3N+3 unknowns. We can express 3N of the equations as

$$\sum_{k=1}^{N}\sum_{i,j=1}^{5}\sum_{m=1}^{3}\Big[\sum_{q=1}^{N}\delta\beta_m^{(q)}\frac{\partial \mathcal{A}_i^{(k)}}{\partial\beta_m^{(q)}}H_{ij}^{(k)}\frac{\partial \mathcal{A}_j^{(k)}}{\partial\beta_l^{(\nu)}}+\delta x_m\frac{\partial \mathcal{A}_i^{(k)}}{\partial x_m}H_{ij}^{(k)}\frac{\partial \mathcal{A}_j^{(k)}}{\partial\beta_l^{(\nu)}}\Big]$$
$$=\sum_{k=1}^{N}\sum_{i,j=1}^{5}\Big[\alpha_i^{(k)}-\mathcal{A}_{i0}^{(k)}\Big]H_{ij}^{(k)}\frac{\partial \mathcal{A}_j^{(k)}}{\partial\beta_l^{(\nu)}}\qquad \nu=1,2,...,N,\ l=1,2,3.$$

The remaining 3 equations are

$$\sum_{k=1}^{N}\sum_{i,j=1}^{5}\sum_{m=1}^{3}\Big[\sum_{q=1}^{N}\delta\beta_m^{(q)}\frac{\partial \mathcal{A}_i^{(k)}}{\partial\beta_m^{(q)}}H_{ij}^{(k)}\frac{\partial \mathcal{A}_j^{(k)}}{\partial x_l}+\delta x_m\frac{\partial \mathcal{A}_i^{(k)}}{\partial x_m}H_{ij}^{(k)}\frac{\partial \mathcal{A}_j^{(k)}}{\partial x_l}\Big]$$
$$=\sum_{k=1}^{N}\sum_{i,j=1}^{5}\Big[\alpha_i^{(k)}-\mathcal{A}_{i0}^{(k)}\Big]H_{ij}^{(k)}\frac{\partial \mathcal{A}_j^{(k)}}{\partial x_l}\qquad l=1,2,3.$$

These expressions can be simplified by noting that the only correlated parameters in the set of tracks being vertexed are the x_l coordinates, i.e. the x, y, and z vertex position common to all the tracks. Therefore, we demand

$$\frac{\partial \mathcal{A}_i^{(k)}}{\partial\beta_m^{(q)}}=0 \text{ unless } k=q.$$

This simplifies the 3N equations formula to

$$\sum_{ij=1}^{5}\sum_{m=1}^{3}\Big[\Big(\delta\beta_m^{(\nu)}\frac{\partial \mathcal{A}_i^{(\nu)}}{\partial\beta_m^{(\nu)}}H_{ij}^{(\nu)}\frac{\partial \mathcal{A}_j^{(\nu)}}{\partial\beta_l^{(\nu)}}\Big)+\delta x_m\frac{\partial \mathcal{A}_i^{(\nu)}}{\partial x_m}H_{ij}^{(\nu)}\frac{\partial \mathcal{A}_j^{(\nu)}}{\partial\beta_l^{(\nu)}}\Big]=\sum_{i,j=1}^{5}\Big[\alpha_i^{(\nu)}-\mathcal{A}_{i0}^{(\nu)}\Big]H_{ij}^{(\nu)}\frac{\partial \mathcal{A}_j^{(\nu)}}{\partial\beta_l^{(\nu)}}.$$

for l = 1,2,3 while the second set of equations becomes

$$\sum_{i,j=1}^{5}\sum_{m=1}^{3}\Big[\sum_{k=1}^{N}\delta\beta_m^{(k)}\frac{\partial \mathcal{A}_i^{(k)}}{\partial\beta_m^{(k)}}H_{ij}^{(k)}\frac{\partial \mathcal{A}_j^{(k)}}{\partial x_l}+\sum_{k=1}^{N}\delta x_m\frac{\partial \mathcal{A}_i^{(k)}}{\partial x_m}H_{ij}^{(k)}\frac{\partial \mathcal{A}_j^{(k)}}{\partial x_l}\Big]$$
$$=\sum_{k=1}^{N}\sum_{i,j=1}^{5}\Big[\alpha_i^{(k)}-\mathcal{A}_{i0}^{(k)}\Big]H_{ij}^{(k)}\frac{\partial \mathcal{A}_j^{(k)}}{\partial x_l}\qquad l=1,2,3.$$

Now let's rewrite the above expressions in terms of some new notation. We will express the first equation as

$$\sum_{m=1}^{3}\left[R_{lm}^{(\nu)}\delta\beta_m^{(\nu)}+Q_{lm}^{(\nu)}\delta x_m\right]=\aleph_l^{(\nu)} \qquad \text{for } \nu=1,...,N\ ,l=1,2,3.$$

where

$$R_{lm}^{(\nu)}=\sum_{i,j=1}^{5}\frac{\partial\mathcal{A}_i^{(\nu)}}{\partial\beta_m^{(\nu)}}H_{ij}^{(\nu)}\frac{\partial\mathcal{A}_j^{(\nu)}}{\partial\beta_l^{(\nu)}} \qquad 3\times 3 \text{ matrix for each track}$$

$$Q_{lm}^{(\nu)}=\sum_{i,j=1}^{5}\frac{\partial\mathcal{A}_i^{(\nu)}}{\partial x_m}H_{ij}^{(\nu)}\frac{\partial\mathcal{A}_j^{(\nu)}}{\partial\beta_l^{(\nu)}} \qquad 3\times 3 \text{ matrix for each track}$$

$$\aleph_l^{(\nu)}=\sum_{i,j=1}^{5}\left[\alpha_i^{(\nu)}-\mathcal{A}_{i0}^{(\nu)}\right]H_{ij}^{(\nu)}\frac{\partial\mathcal{A}_j^{(\nu)}}{\partial\beta_l^{(\nu)}} \qquad 3 \text{ element vector for each track.}$$

The second set of equations will be written as

$$\sum_{m=1}^{3}\left[\sum_{k=1}^{N}S_{lm}^{(k)}\delta\beta_m^{(k)}+T_{lm}\delta x_m\right]=Z_l \qquad l=1,2,3.$$

with

$$S_{lm}^{(k)}=\sum_{i,j=1}^{5}\frac{\partial\mathcal{A}_i^{(k)}}{\partial\beta_m^{(k)}}H_{ij}^{(k)}\frac{\partial\mathcal{A}_j^{(k)}}{\partial x_l}=Q_{ml}^{(k)} \qquad 3\times 3 \text{ matrix for each track}$$

$$T_{lm}=\sum_{i,j=1}^{5}\sum_{k=1}^{N}\frac{\partial\mathcal{A}_i^{(k)}}{\partial x_m}H_{ij}^{(k)}\frac{\partial\mathcal{A}_j^{(k)}}{\partial x_l} \qquad 3\times 3 \text{ matrix}$$

$$Z_l=\sum_{k=1}^{N}\sum_{i,j=1}^{5}\left[\alpha_i^{(k)}-\mathcal{A}_{i0}^{(k)}\right]H_{ij}^{(k)}\frac{\partial\mathcal{A}_j^{(k)}}{\partial x_l} \qquad 3 \text{ element vector.}$$

We now make use of the fact that the track parameters and error matrices are calculated in the vicinity of the beam interaction point (and therefore in the vicinity of the vertex position we seek). Hence we can use the fact that

$$\frac{\partial\mathcal{A}_i}{\partial\beta_j}=\delta_{ij}\ , \qquad \frac{\partial\mathcal{A}_{4,5}}{\partial\beta_j}=0 \qquad \text{and} \qquad \frac{\partial\mathcal{A}_i}{\partial x_m}=0 \qquad \begin{cases} i,j=1,2,3 \\ m=1,2,3 \end{cases}$$

keeping in mind that we have already calculated

$$\mathcal{A}_1, \mathcal{A}_2, \mathcal{A}_3, \mathcal{A}_4, \mathcal{A}_5 = \phi, \frac{1}{p\cos\lambda}, \tan\lambda, \xi_V, \text{ and } \eta_V.$$

If we now calculate

$$\frac{\partial \mathcal{A}_4}{\partial x_m} = \frac{\partial \xi}{\partial x_m} \equiv \varrho_m \quad \text{and} \quad \frac{\partial \mathcal{A}_5}{\partial x_m} = \frac{\partial \eta}{\partial x_m} \equiv \varsigma_m \qquad (m = 1,2,3),$$

where ϱ_m and ς_m are components of $\hat{\xi}$ and $\vec{\epsilon}$, then we can simplify the equations even further since now

$$\begin{aligned}
R_{lm}^{(\nu)} &= H_{lm}^{(\nu)} \\
Q_{lm}^{(\nu)} &= \varrho_m^{(\nu)} H_{4l}^{(\nu)} + \varsigma_m^{(\nu)} H_{5l}^{(\nu)} \\
\aleph_l^{(\nu)} &= \sum_{i=1}^{5} \left[\alpha_i^{(\nu)} - \mathcal{A}_{i0}^{(\nu)}\right] H_{il}^{(\nu)} \\
S_{lm}^{(k)} &= H_{m4}^{(k)}(\varrho_l^{(k)}) + H_{m5}^{(k)}(\varsigma_l^{(k)}) = Q_{ml}^{(k)} \\
T_{lm} &= \sum_{k=1}^{N} \left[H_{45}^{(k)} \varrho_m^{(k)} \varsigma_l^{(k)} + H_{54}^{(k)} \varsigma_m^{(k)} \varrho_l^{(k)} + H_{44}^{(k)} \varrho_m^{(k)} \varrho_l^{(k)} + H_{55}^{(k)} \varsigma_m^{(k)} \varsigma_l^{(k)}\right] \\
Z_l &= \sum_{k=1}^{N} \left[\sum_{i=1}^{5} \left[\alpha_i^{(k)} - \mathcal{A}_{i0}^{(k)}\right] \left(H_{i4}^{(k)} \varrho_l^{(k)} + H_{i5}^{(k)} \varsigma_l^{(k)}\right)\right].
\end{aligned}$$

Hence, we have 3N+3 equations

$$\begin{aligned}
\sum_{m=1}^{3} \left[H_{lm}^{(\nu)} \delta\beta_m^{(\nu)} + Q_{lm}^{(\nu)} \delta x_m\right] &= \aleph_l^{(\nu)} \qquad l = 1,2,3, \quad \nu = 1,\ldots,N \\
\sum_{m=1}^{3} \left[\sum_{k=1}^{N} \left[Q_{lm}^{T(k)} \delta\beta_m^{(k)} + T_{lm} \delta x_m\right]\right] &= Z_l \qquad l = 1,2,3
\end{aligned}$$

where $\mathbf{Q}^T$ is the transpose of $\mathbf{Q}$. Now let's assemble all the equations into one

by defining

$$\begin{pmatrix} \delta\beta_1^{(1)} \\ \delta\beta_2^{(1)} \\ \delta\beta_3^{(1)} \\ \delta\beta_1^{(2)} \\ \delta\beta_2^{(2)} \\ \delta\beta_3^{(2)} \\ \vdots \\ \delta x_1 \\ \delta x_2 \\ \delta x_3 \end{pmatrix} \quad \begin{matrix} \} \text{track 1} \\ \\ \\ \} \text{track 2} \\ \\ \\ \vdots \\ \} \text{vertex} \\ \\ \end{matrix}$$

which we will call **D**, and

$$\begin{pmatrix} \aleph_1^{(1)} \\ \aleph_2^{(1)} \\ \aleph_3^{(1)} \\ \aleph_1^{(2)} \\ \aleph_2^{(2)} \\ \aleph_3^{(2)} \\ \vdots \\ Z_1 \\ Z_2 \\ Z_3 \end{pmatrix} \quad \begin{matrix} \} \text{track 1} \\ \\ \\ \} \text{track 2} \\ \\ \\ \vdots \\ \} \text{3 component vector} \\ \\ \end{matrix}$$

which we will call **W**. Thus, we reduce all 3N+3 equations to the form **UD** = **W**, where **U** is the (3N+3)× (3N+3) matrix shown on the next page.

$$\mathbf{U} = \begin{bmatrix} \mathbf{H}^{(1)} & 0 & \dots & \dots & 0 & \mathbf{Q}^{(1)} \\ 0 & \mathbf{H}^{(2)} & 0 & \dots & 0 & \mathbf{Q}^{(2)} \\ 0 & 0 & \mathbf{H}^{(3)} & 0 & \vdots & \mathbf{Q}^{(3)} \\ \vdots & \vdots & \dots & \ddots & 0 & \vdots \\ 0 & 0 & 0 & \dots & \mathbf{H}^{(N)} & \mathbf{Q}^{(N)} \\ \mathbf{Q}^{T(1)} & \mathbf{Q}^{T(2)} & \mathbf{Q}^{T(3)} & \dots & \mathbf{Q}^{T(N)} & \mathbf{T} \end{bmatrix}$$

Our original goal was to solve for the values of the column vector $\mathbf{D}$, so the solution is given by

$$\mathbf{D} = \mathbf{U}^{-1}\mathbf{W}.$$

The squared error matrix is given by $\mathbf{U}^{-1}$, thus

$$\langle \sigma_a \cdot \sigma_b \rangle = [\mathbf{U}^{-1}]_{lm}$$

where

$$a = \delta\beta_i^{(k)} \qquad l = 3(k-1) + i$$

$$a = \delta x_i \qquad l = 3N + i$$

and similarly for b and m.

Appendix B

Here we define some of the Monte Carlo parameters which were most relevant to this analysis. For example, the decay distance for a D decay with a given lifetime depends on the momentum of the D, thus if we wish to compare results from the Monte Carlo to the real data we need a parametrization of the momentum spectrum of D's in charm events. Such a parametrization is given by a fragmentation function. The form of this function determines the probability that a quark of a given type with a given energy will produce a hadron of a given energy. Following the Peterson convention,[47] the Monte Carlo used in this analysis assumes that the form of this function for heavy quarks such as charm and bottom is

$$F_Q(z) = \frac{A}{z[1 - \frac{1}{z} - \frac{\epsilon_Q}{(1-z)}]^2}$$

for a quark of flavor Q (charm or bottom) fragmenting to a hadron of energy zE_Q where E_Q is the energy of the quark and z is the fraction of quark energy taken by the hadron. The parameter A is an arbitrary normalization constant. The shape of the function as a function of z is determined by the parameter ϵ_Q. We assumed $\epsilon_c = 0.3$ (for charm) and $\epsilon_b = 0.03$ (for bottom).

In determining the background due to B decays to charm mesons, we have used information from ref. 34 in setting the branching fraction of B mesons to D^{*+} and the momentum spectrum of D^{*+} mesons from B mesons. For example, the spectrum of D^0's from B mesons is shown in fig. 58. The shape of the data is consistent with a large proportion of the D^0 mesons being produced by semileptonic B decay. In our Monte Carlo studies, the momentum spectrum of D's from B mesons has been chosen to be consistent with the data in this figure. The branching fraction of B mesons into D^{*+} mesons was set to 50%. This

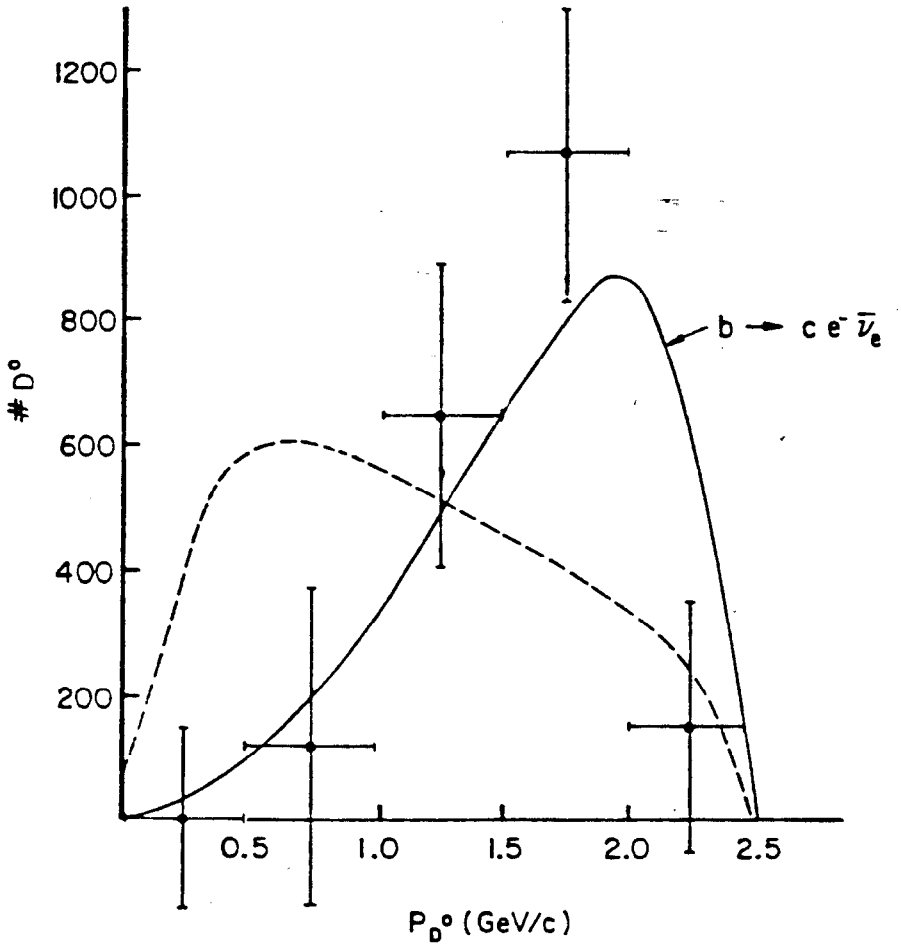

Fig. 57: Plot of number of D^0 mesons vs. D momentum from CLEO data (ref. 34). The dashed curve shows the phase space expectation while the solid curve shows the expected shape for semileptonic decays of b quarks to charm.

parameter and the shape of the momentum spectrum were varied in determining the error on the 3% background estimate of D^{*+} mesons from B decays.

REFERENCES

1. J.-E. Augustin, et. al., Phys. Rev. Lett., 33, 1406 (1974).
2. J.J. Aubert, et. al., Phys. Rev. Lett., 33, 1404 (1974).
3. M.K. Gaillard, B.W. Lee and J. Rosner,Rev. Mod. Phys., 47, 277 (1975).
4. S.L. Glashow, J. Iliopoulis, and L. Maiani, Phys. Rev. D2, 1285 (1970).
5. W. Bacino, et. al., Phys. Rev. Lett., 45, 329 (1980).
6. R.H. Schindler, et. al., Phys. Rev. D24, 78 (1981).
7. R.L. Kingsley, et. al., Phys. Rev. D11, 1919 (1975).
8. J.F. Donoghue and L.W. Wolfenstein, Phys. Rev. D15, 3341 (1977).
9. M.B.Einhorn and C. Quigg, Phys. Rev. D12, 2015 (1975)..
10. I. Perruzzi, et. al., Phys. Rev. Lett., 39, 1301 (1977).
11. W. Bernreuther, D. Nachtmann, and B. Stech, Zeit. Physik C, Parts. and Fields 4, 257 (1980).
12. Myron Bander, D. Silvermann, and A. Soni, Phys. Rev. Lett., 44, 7 (1980).
13. B. Guberina, S. Nussinov, R.D. Peccei, and R. Rückl, Phys. Lett. 98B, 111 (1979).
14. T. Kobayashi and N. Yamazaki, Prog. Theor. Phys. 65, 775 (1981).
15. V.A.Khoze and M.A. Shifman, Uspeki Fiz. Nauk 140, 3 (1983) and preprint DESY 83-105, Oct. 1983.
16. G. Alterelli and L. Maiani, Phys. Lett. 118B, 414 (1982).
17. H.Sawayanagi, K. Fujii, T. Okazaki and S. Okuba, Phys. Rev. D27,2107 (1983).

18. J.A. Jaros, in Proc. of the Int. Conf. on Instrumentation for Colliding Beam Physics, SLAC-Report 250, Edited by W. Ash, Stanford, CA (1982), p. 29.

19. W. Davies-White, et. al., Nucl. Instr. and Methods 160, 227 (1979).

20. G.S. Abrams, et. al., IEEE Trans. NS-25, 309 (1978).

21. G.S. Abrams et. al., IEEE Trans. NS-27, 59 (1980).

22. K.G. Hayes, SLAC-237 (1981), Ph.D. Thesis (unpublished).

23. J.D. Fox and M.E.B. Franklin, IEEE Trans. NS-25, no. 3 (1981).

24. T. Himel, SLAC-223 (1979), Ph.D. Thesis (unpublished).

25. H. Brafman, et. al., IEEE Trans. NS-25, 692 (1978).

26. R.L. Ford and W.R. Nelson, SLAC-0210, June 1978, 277 pp.

27. P. Bevington, Data Reduction and Error Analysis for the Physical Sciences MacGraw - Hill, New York, N.Y., (1969).

28. M.E. Nelson et. al., Phys. Rev. Lett. 50, 1542 (1983).

29. J.M. Yelton et. al., Phys. Rev. Lett. 49, 430 (1982).

30. G. Goldhaber, Proceedings of the 18th Rencontre de Moriond, 1983. Also printed as LBL-16146 (1983).

31. M. E. Nelson et. al., , Phys. Rev. Lett. 50, 1542 (1983).

32. E. Fernandez et. al., , Phys. Rev. Lett. 50, 2054 (1983).

33. B. Adeva et. al., , Phys. Rev. Lett. 51, 443 (1983).

34. J. Green et. al., , Phys. Rev. Lett. 51 347 (1983).

35. A description of the photon finding algorithm can be found in C. A. Blocker, PhD. Thesis, LBL-10801.

36. D. Amidei, et. al., Ph.D. Thesis, LBL-17795 (1984).

37. N. Lockyer et. al., , Phys. Rev. Lett. 51, 1316 (1983).
E. Fernandez et. al., , Phys. Rev. Lett. 51, 1022 (1983).

38. N. Ushida et. al., , Phys. Lett. 121B, 287 and 292 (1983).
Emulsion experiment - E531.

39. M. Adamovich et. al., , Phys. Lett. 140B, 119 (1984).
Emulsion experiment - WA58.

40. M. Aguilar-Benitez et. al., , Phys. Lett. 122B, 312 (1983) and Phys. Lett. 146B, 266 (1984).
Bubble chamber experiment - NA16 (LEBC).

41. A. Badertscher et. al., , Phys. Lett. 123B, 471 (1983).
Bubble chamber experiment - NA18 (BIBC).

42. K. Abe et. al., , Phys. Rev. D30, 1 (1984).
Bubble chamber experiment - BC72/73.

43. E.H.S. Collaboration, Proceedings of the 18th Rencontre de Moriond, 1984.
Bubble chamber experiment - NA27.

44. R. Bailey, et. al., , CERN-EP/84-18.
Silicon strip experiment - NA11.

45. S. R. Amendolia et. al., , CERN-EP/82-200.
Silicon strip experiment - NA1.

46. R. M. Baltrusaitis et. al., , SLAC-PUB-3532.

47. C. Peterson et. al., , Phys. Rev. D27, 105 (1983).